



University of Kentucky  
UKnowledge

---

University of Kentucky Doctoral Dissertations

Graduate School

---

2004

## ELECTRO-OPTICAL STUDIES OF CHARGE-DENSITY-WAVE MATERIALS

Ram C. Rai

*University of Kentucky*, [rcrai312@yahoo.com](mailto:rcrai312@yahoo.com)

[Right click to open a feedback form in a new tab to let us know how this document benefits you.](#)

---

### Recommended Citation

Rai, Ram C., "ELECTRO-OPTICAL STUDIES OF CHARGE-DENSITY-WAVE MATERIALS" (2004). *University of Kentucky Doctoral Dissertations*. 427.

[https://uknowledge.uky.edu/gradschool\\_diss/427](https://uknowledge.uky.edu/gradschool_diss/427)

This Dissertation is brought to you for free and open access by the Graduate School at UKnowledge. It has been accepted for inclusion in University of Kentucky Doctoral Dissertations by an authorized administrator of UKnowledge. For more information, please contact [UKnowledge@lsv.uky.edu](mailto:UKnowledge@lsv.uky.edu).

ABSTRACT OF DISSERTATION

Ram C. Rai

The Graduate School  
University of Kentucky  
2004

ELECTRO-OPTICAL STUDIES OF CHARGE-DENSITY-WAVE MATERIALS

---

ABSTRACT OF DISSERTATION

---

A dissertation submitted in partial fulfillment of the requirements for  
the degree of Doctor of Philosophy in the College of Arts and Sciences  
at the University of Kentucky

By

Ram C. Rai

Lexington, Kentucky

Director: Dr. Joseph W. Brill, Professor of Physics and Astronomy

Lexington, Kentucky

2004

Copyright © Ram C Rai 2004

## ABSTRACT OF DISSERTATION

### ELECTRO-OPTICAL STUDIES OF CHARGE-DENSITY-WAVE MATERIALS

A search for narrow-band-noise (NBN) modulations of the infrared transmission in blue bronze has been performed. No modulations were observed, giving an upper limit for NBN changes in the absorption coefficient of  $\Delta\alpha_{NBN} < 0.3 / \text{cm}$  ( $\approx \alpha / 2000$ ). The implication of these results on proposed CDW properties and NBN mechanisms are discussed.

An infrared microscope with a capability of doing both reflectance and transmission measurements has been integrated into the previous electro-transmission system with tunable diode lasers. Electro-optic experiments were done using the microscope for the studies of the CDW states of  $\text{K}_{0.3}\text{MoO}_3$  (blue bronze) and orthorhombic  $\text{TaS}_3$ .

The electro-reflectance signal for blue bronze has been evidenced for the first time. The infrared reflectance of  $\text{K}_{0.3}\text{MoO}_3$  varied with position when a voltage greater than the CDW depinning threshold is applied. The spatial dependence of  $\Delta R/R$  was slightly different than for  $\Delta\tau/\tau$ , in that the magnitude of  $\Delta R/R$  decreased and, for low voltages and frequencies, the signal became inverted near the contacts. Perhaps the differences might be associated with changes in the CDW properties on the surface. For blue bronze, the electro-reflectance signal was measured to be smaller than electro-transmittance signal by one order of magnitude for light polarized transverse to the chain direction, while the electro-reflectance signal for parallel polarized light was found to be a few times smaller than for transverse polarized light.

The fits of the electro-reflectance spectrum showed that the changes in background dielectric constant were  $\sim 0.05\%$  and/or oscillator strength and/or frequency shifts of the phonons were  $\sim 0.05\%$  and  $\sim 0.005\text{ cm}^{-1}$  in the applied electric field. We also found that parallel polarized phonons are affected by CDW strain, and these changes dominate the electro-reflectance spectrum. We have examined the electro-reflectance spectra associated with CDW current investigation for light polarized parallel to the conducting chains for signs of expected current-induced intragap states, and conclude that the density of any such states is at most a few times less than expected.

We have observed a large ( $\sim 1\%$ ) change in infrared reflectance of orthorhombic TaS<sub>3</sub>, when its CDW is depinned. The change is concentrated near one current contact. Assuming that the change in reflectance is proportional to the degree of CDW polarization, we have studied the dynamics of CDW repolarization through position dependent measurements of the variation of the electro-reflectance with the frequency of square wave voltages applied to the sample, and have found that the response could be characterized as a damped harmonic oscillator with a distribution of relaxation (i.e. damping) times. The average relaxation time, which increases away from the contacts, varies with applied voltage as  $\tau_0 \propto V^{-p}$  with  $p \sim 3/2$ , but the distribution of times broadens as the voltage approaches the depinning threshold. Very low resonant frequencies ( $\sim 1\text{ kHz}$ ) indicate a surprisingly large amount of inertia, which is observable in the time dependence of the change in reflectance as a polarity dependent delay of  $\sim 100\ \mu\text{s}$ .

KEYWORDS: Quasi-One-Dimensional, Charge-Density-Waves, Electro-Optic Effect, IR Spectrum, Polarization Dynamics.

\_\_\_\_\_  
Ram C Rai

\_\_\_\_\_  
July 2, 2004

ELECTRO-OPTICAL STUDIES OF CHARGE-DENSITY-WAVE MATERIALS

By

Ram C. Rai

Dr. Joseph W. Brill  
(Director of Dissertation)

Dr. Thomas Troland  
(Director of Graduate Studies)

July 2, 2004

## RULES FOR THE USE OF DISSERTATIONS

Unpublished dissertations submitted for the Doctor's degree and deposited in the University of Kentucky Library are as a rule open for inspection, but are to be used only with due regard to the rights of the authors. Bibliographical references may be noted, but quotations or summaries of parts may be published only with the permission of the author, and with the usual scholarly acknowledgments.

Extensive copying or publication of the dissertation in whole or in part also requires the consent of the Dean of the Graduate School of the University of Kentucky.

DISSERTATION

Ram C. Rai

The Graduate School  
University of Kentucky  
2004



ELECTRO-OPTICAL STUDIES OF CHARGE-DENSITY-WAVE MATERIALS

---

DISSERTATION

---

A dissertation submitted in partial fulfillment of the requirements for the  
degree of Doctor of Philosophy in the College of Arts and Sciences  
at the University of Kentucky

By

Ram C. Rai

Lexington, Kentucky

Director: Dr. Joseph W. Brill, Professor of Physics and Astronomy

Lexington, Kentucky

2004

Copyright © Ram C Rai 2004

DEDICATED TO MY PARENTS

R. B. RAI AND M. K. RAI

# ACKNOWLEDGEMENTS

First, I would like to express my sincere respect and appreciation to my dissertation advisor, Dr. J. W. Brill for his guidance and support throughout the course of the research project. In addition, Dr. Brill provided timely and instructive comments and evaluation at every stage of the dissertation process, allowing me to complete this dissertation on schedule. I also would like to thank the other members of my advisory committee, Dr. J. Anthony, Dr. G. Cao, Dr. K. MacAdam, Dr. G. Murthy, and Dr. K. W. Ng, for their guidance and expertise.

I also would like to thank Dr. V. Bondarenko, Dr. B. M. Emerling, Dr. M. Itkis, and Dr. D. K. Powell, for their help and support. I appreciate the technical assistance provided by staffs in the electronic shop, the machine shop, and vacuum shop.

I would like to thank Prof. R. E. Thorne of the Cornell University, for providing crystals. This research project was funded by the National Science Foundation Grant # DMR-0100572.

I am grateful to my parents in Nepal who always encouraged and supported me with great love while pursuing my studies abroad. I am also grateful to my sisters for their encouragement. I also want to thank my niece, Tara Limbu, and my friend, Meena Rai, for their help.

# TABLE OF CONTENTS

Acknowledgements . . . . .	iii
List of Tables . . . . .	vi
List of Figures . . . . .	vii
List of Files . . . . .	xii
1 Introduction. . . . .	1
1.1 Background . . . . .	1
1.2 Theory of Charge-Density-Wave Ground State . . . . .	3
1.3 Pinning in the CDW State . . . . .	6
1.4 Phase Slip Processes . . . . .	8
1.5 Review of Physical Properties of $K_{0.3}MoO_3$ . . . . .	13
1.6 Review of Physical Properties of $TaS_3$ . . . . .	16
1.7 Review of Electro-optic Effect in Blue Bronze . . . . .	19
1.7.1 Spatial and Voltage Dependences of the Electro-optic effect . . . . .	21
1.7.2 Theory of the Electro-optic Effect for Blue Bronze . . . . .	23
1.7.3 Comparison of $\Delta\tau/\tau$ for Unipolar and Bipolar Voltages . . . . .	26
1.7.4 Electro-optic Effect Due to Changes in Phonons . . . . .	29
2 Experimental Procedures . . . . .	31
2.1 Introduction . . . . .	31
2.2 Electro-optic System . . . . .	32
2.2.1 Tunable Diode Lasers . . . . .	34
2.2.2 Optics Module . . . . .	36
2.2.3 Cryostat . . . . .	39
2.2.4 Infrared Microscope . . . . .	41
2.3 Laser Calibration . . . . .	43
2.4 Sample Preparation . . . . .	44

2.5	Experimental Set-up for Electro-Optic Measurements . . . . .	48
2.5.1	Electro-Transmission Measurements . . . . .	49
2.5.2	Electro-Reflectance Measurements . . . . .	51
3	Results and Discussions . . . . .	54
3.1	Search for Narrow-Band-Noise Modulations of the Infrared Transmission of Blue Bronze . . . . .	54
3.2	Electro-Reflectance Spectra of Blue Bronze . . . . .	63
3.2.1	Voltage and Spatial Dependences of the Electro-Reflectance . . . . .	66
3.2.2	Effects of CDW Polarization on Phonons . . . . .	70
3.2.3	Parallel Electro-Reflectance Spectra . . . . .	78
3.2.4	Conclusion . . . . .	85
3.3	Dynamics of the Electro-Reflective Response of TaS <sub>3</sub> . . . . .	86
3.3.1	Voltage and Spatial Dependences of the Electro-Reflectance . . . . .	89
3.3.2	Frequency Dependence of the Electro-Reflective Response . . . . .	91
3.3.3	Real Time Measurement of the Electro-Reflective Response . . . . .	101
3.3.4	Conclusion . . . . .	104
3	Conclusions . . . . .	108
4	Appendix . . . . .	112
	References . . . . .	117
	Vita . . . . .	122

# LIST OF TABLES

1	The values of the fitting parameters . . . . .	74
---	--	----

# LIST OF FIGURES

Figure 1.1	The band structure of a one-dimensional electron gas: (a) An undistorted system at $T > T_p$ . (b) Peierls insulator at $T < T_p$ . This figure is appropriate for a one-third filled band. . . . . 4
Figure 1.2	(a) A charge-density wave with a local distortion in the phase (full line), and dashed line is undistorted CDW. (b) Spatial dependence of the phase $\phi$ . . . . . 11
Figure 1.3	(a) Energy bands for current conversion sequence. (b) Dislocation nucleation sequence in current conversion process. . . . . 12
Figure 1.4	Linear chains of $\text{MoO}_6$ octahedra along the monoclinic b axis in blue bronze. Unit cell parameters <sup>36</sup> at room temperature: $a = 18.249 \text{ \AA}$ , $b = 7.560 \text{ \AA}$ , $c = 9.855 \text{ \AA}$ , and $\beta = 117.53^\circ$ . . . . . 14
Figure 1.5	(a) Resistivity of $\text{K}_{0.3}\text{MoO}_3$ as a function of $1000/T$ along the b-direction, along $[102]$ direction, and perpendicular to $[\bar{2}01]$ direction. <sup>36</sup> (b) Normalized resistivity of ortho- $\text{TaS}_3$ and $\text{K}_{0.3}\text{MoO}_3$ as a function of $1000/T$ along the b-direction (measured in our lab). . . . . 15
Figure 1.6	(a) Structure of $\text{NbSe}_3$ . Three linear chains with slightly different values of X-X bond lengths are shown here. (b) A model for the unit cell of the orthorhombic $\text{TaS}_3$ . Each unit cell has 24 chains roughly similar to the chains in $\text{NbSe}_3$ structure, but the detailed structure of the chains has not been determined. . . . . 17
Figure 1.7	(a) Open and closed triangles show electromodulated transmission at $x = 1.02$ (the end of the sample) and $0.80 \text{ mm}$ , respectively, for a sample at $99 \text{ K}$ ; Solid curve shows current vs voltage. (b) Spatial dependence of the electromodulated transmission at different voltages. Data for successive voltages are vertically offset by $0.5\%$ for clarity. Dashed curves show the approximate bulk strains and shading shows the contact strains. . . . . 22
Figure 1.8	Closed and open circles represent electrons and holes. The $\epsilon_F$ is the Fermi energy. (a) An undistorted CDW state and its energy band without any external field. (b) Polarization of the CDW state in the presence of an external field and resulting band bending near the gap, causing changes in quasiparticle density. . . . . 25
Figure 1.9	(a) Voltage dependence of $\Delta\tau/\tau$ for bipolar, unipolar, and inverted unipolar square wave pulses, and the CDW current <sup>54</sup> (Note that the

	polarity of $\Delta\tau/\tau$ is inverted for the unipolar voltages in this reference). (b) Spatial dependence of $\Delta\tau/\tau$ for bipolar square waves at $\pm 3.7 V_T$ and $\pm V_T$ , and a unipolar square wave at $+3V_T$ . The vertical arrows indicate representative contact contributions. <sup>55</sup> . . . . . 28
Figure 1.10	(a) The optical density and (b) the electromodulated transmission spectra of blue bronze at 82 K. These spectra were taken with bipolar square wave voltages, $V = \pm 1.7 V_p$ , (where $V_p = 15$ mV for the sample). . . . . 30
Figure 2.1	Block diagram of the electro-optical system. This schematic is drawn for electro-reflectance measurements. However, the electro-optical system can be used for both transmission and reflection measurements. . . . . 33
Figure 2.2	Optics module designed for tunable diode lasers (TDLs). . . . . 37
Figure 2.3	Schematic diagram of the MicrostatN cryostat for sample cooling (Reproduced from Operator's Handbook, Oxford Instruments, Inc.). . . 40
Figures 2.4	Part of the infrared microscope. The collimated beams are shown for reflectance and transmission sampling modes. . . . . 42
Figure 2.5	Typical calibration curves for four tunable diode lasers (TDLs) operating at different currents; laser 1 at 400 mA, laser 2 at 500 mA, laser 3 at 700 mA, and laser 4 at 800 mA. The solid lines are polynomial fits to the data. The cubic fitting parameters for laser 1 are shown in the box. .45
Figure 2.6	(a) Blue bronze sample mounted on a sapphire substrate for reflectance and a KRS-5 substrate for transmission. (b) Ortho-TaS <sub>3</sub> sample mounted on a sapphire substrate. . . . . 47
Figure 2.7	Block diagram for the electro-transmission measurements with a digital oscilloscope. M1, M2, and M3 are 90 <sup>0</sup> off-axis-ellipsoidal mirrors, Ge (Zn) is a zinc doped germanium photoconductor detector, and OAP is a 90 <sup>0</sup> off-axis-parabolic mirror. . . . . 50
Figure 3.1	Voltage oscillations for an ortho-TaS <sub>3</sub> sample (dimensions: 1.5 mm x 20 $\mu\text{m}$ x 5 $\mu\text{m}$ , $R = 13.5$ k $\Omega$ , and $I_T = 2.3$ $\mu\text{A}$ ) at 78K. (a) Voltage oscillations for $I = 3.5$ $\mu\text{A}$ directly observed on an oscilloscope, (b) Fourier transformed of Fig (a), and (c) Fourier transformed of voltage oscillations for $I = 3.2$ $\mu\text{A}$ . . . . . 55
Figure 3.2	Sample-voltage NBN spectra at different dc currents for (a) Sample #2 ( $I_T = 110$ $\mu\text{A}$ ) at 78 K. For clarity, spectra for 180 $\mu\text{A}$ and 200 $\mu\text{A}$ are shifted up by 5 dB and 10 dB respectively, (b) Sample #3. Each spectrum is shifted by 10 dB (except for $I = 120$ $\mu\text{A}$ ) for clarity. The inset graphs show the linear relationship between the fundamental (NBN) frequencies



	and the CDW currents. Sample #2 has two large fundamental frequencies whereas Sample #3 has just one fundamental frequency for each dc current. . . . .	58
Figure 3.3	(a) NBN spectra of voltage across Sample #2 at $V = 1.5V_T$ . (b) Fourier transforms of IR transmission signal through Sample #2 at $V = 1.5V_T$ , position near ( $\sim 100 \mu\text{m}$ ) positive current contact. . . . .	59
Figure 3.4	(a) NBN spectra of voltage across Sample #3 at $V = 1.5V_T$ . (b) Fourier transforms of IR transmission signal through Sample #3 at $V = 1.5V_T$ , position near ( $\sim 100 \mu\text{m}$ ) positive current contact. . . . .	60
Figure 3.5	For Sample #1; (a) Voltage dependence of $\Delta R/R$ for bipolar, unipolar voltages (adjacent to contact), and the CDW current, (b) Voltage dependence of $\Delta R/R$ for $\nu = 535 \text{ cm}^{-1}$ and $1050 \text{ cm}^{-1}$ (adjacent to contact), and (c) Spatial dependence of $\Delta R/R$ for bipolar and positive unipolar square-wave voltages at 40 mV. . . . .	67
Figure 3.6	Spatial profiles of $\Delta R/R$ for transverse polarized light at $1050 \text{ cm}^{-1}$ (a) Several bipolar square-wave voltages at 253 Hz. (b) Bipolar voltages 40 mV and 16 mV at each 253 Hz and 1.34 kHz. . . . .	69
Figure 3.7	(a) Reflectivity spectrum for transverse polarization. Phonon resonances are labeled A – J. (b) Electro-reflectance spectrum for transverse polarization, measured with 253 Hz, 80 mV bipolar square-wave near the contact. . . . .	71
Figure 3.8	A portion of reflectivity spectrum (in Figure 3.7) for transverse polarized light. The solid line represents the fitted curve. . . . .	74
Figure 3.9	Fits of the electro-reflectance spectrum by varying different parameters as indicated in each graph: (a) only $\epsilon_b$ is changed, (b) $A$ 's are changed for all three phonons, (c) $\Gamma$ 's are changed for all three phonons, (d) $\nu$ 's are changed for all three phonons, (e) $\epsilon_b$ , and $A$ 's are changed for all three phonons, and, and (f) $\epsilon_b$ , $A$ 's, and $\nu$ 's are changed for all three phonons. . . . .	75-77
Figure 3.10	Spatial dependence of the relative change in reflectivity when applying 253 Hz square-wave voltages. ( $715 \text{ cm}^{-1}$ , parallel polarized light) Closed circle: 50 mV, bipolar square-wave. Closed triangles: 50 mV, positive unipolar square-wave. The vertical arrows show the locations of the spectra shown in Figures 3.11. . . . .	79
Figure 3.11	(a) Reflectivity spectrum for parallel polarization. Phonon resonances are labeled K – P. (b) Electro-reflectance spectrum for parallel polarization, measured with 253 Hz, 50 mV square-waves at the locations shown in	

	Figure 3.10. Open symbols: bipolar square-wave. Closed symbols: unipolar square-wave (multiplied by $N \sim 1.9$ ). The curve is the calculated difference in the spectra (vertically offset for clarity) due to the presence of field-induced soliton excitations, with $n = 10^{16} / \text{cm}^3 \sim 1/\text{chain}$ , $\sigma = 400 \text{ \AA}^2$ , $\Gamma = 125 \text{ cm}^{-1}$ , and $\nu = 1100 \text{ cm}^{-1}$ . . . . .	81
Figure 3.12	(a) Reflectivity spectrum for parallel polarization. Phonon resonances are labeled K – Q. (b) Electro-reflectance spectrum for parallel polarization, measured with 253 Hz, 50 mV square-waves for Sample #2. Open symbols: bipolar square-wave. Closed symbols: unipolar square-wave (multiplied by $N \sim 2.1$ ). The curve is the calculated difference in the spectra (vertically offset for clarity) due to the presence of field-induced soliton excitations, with $n = 10^{16} / \text{cm}^3 \sim 1/\text{chain}$ , $\sigma = 400 \text{ \AA}^2$ , $\Gamma = 125 \text{ cm}^{-1}$ , and $\nu = 1100 \text{ cm}^{-1}$ . . . . .	82
Figure 3.13	(a) Voltage dependence of the electro-reflectance at the left contact and the dc R-V curve. (b) Spatial dependence of the in-phase and quadrature response of the electro-reflectance ( $\Delta R/R$ ) to 253 Hz square waves of magnitudes 60, 95, and 150 mV for Sample #1 with light of energy $\nu = 860 \text{ cm}^{-1}$ . The right ( $x \sim 800 \mu\text{m}$ ) contact is grounded and the voltage applied to the left ( $x \sim 0$ ) contact, so that (noting the minus sign on the ordinate) the electro-reflectance decreases for large voltages on the side of the sample which is positive. . . . .	90
Figure 3.14	Spatial dependence of the in-phase response of $\Delta R/R$ for Sample #3 in two different cooling: (a) Square waves of magnitude 30 mV and 40 mV at 253 Hz in the first cooling. (b) Square wave of magnitude 60 mV at 253 Hz in the next cooling. . . . .	92
Figure 3.15	Frequency dependence of the in-phase (upper panel) and quadrature (lower panel) electro-reflectance for 65 mV, 95 mV, 150 mV, and 235 mV square waves for Sample #1, with light ( $\nu = 860 \text{ cm}^{-1}$ , parallel polarization) incident adjacent to the left contact (see Figure 3.13). The curves show fits to Equation. 3.14. . . . .	93
Figure 3.16	Frequency dependence of the in-phase (upper panel) and quadrature (lower panel) electro-reflectance for 78 mV, 95 mV, 150 mV, and 235 mV square waves for Sample #1, with light ( $\nu = 860 \text{ cm}^{-1}$ , parallel polarization) incident at $100 \mu\text{m}$ from the left contact (see Figure 3.13). The curves show fits to Equation. 3.14. . . . .	94
Figure 3.17	Frequency dependence of the in-phase (upper panel) and quadrature (lower panel) electro-reflectance for 78 mV, 95 mV, 150 mV, and 235 mV square waves for Sample #1, with light ( $\nu = 760 \text{ cm}^{-1}$ , perpendicular polarization) incident adjacent to the left contact (see Figure 3.13). The curves show fits to Equation 3.14. . . . .	96

Figure 3.18	Frequency dependence of the in-phase (upper panel) and quadrature (lower panel) electro-reflectance for 110 mV, 150 mV, 200 mV, and 300 mV square waves for Sample #2, with light ( $\nu = 695 \text{ cm}^{-1}$ , parallel polarization) incident adjacent to the contact. The curves show fits to Equation 3.14. . . . . 97
Figure 3.19	Frequency dependence of the in-phase (upper panel) and quadrature (lower panel) electro-reflectance for 110 mV, 150 mV, 200 mV, and 300 mV square waves for Sample #2, with light ( $\nu = 925 \text{ cm}^{-1}$ , perpendicular polarization) incident adjacent to the contact. The curves show fits to Equation 3.14. . . . . 98
Figure 3.20	Voltage dependence of the parameters of Equations 3.15-16. Closed symbols: Sample #1 (measured at $860 \text{ cm}^{-1}$ ); open symbols: Sample #2 (measured at $695 \text{ cm}^{-1}$ ). Circles: light focused adjacent to current contact; triangles: light focused $100 \mu\text{m}$ from this contact. The dotted lines show the onset voltages ( $V_{\text{onset}} \approx 40 \text{ mV}$ for both samples) and thresholds for non-linear current ( $V_T \approx 70 \text{ mV}$ for Sample #1 and $100 \text{ mV}$ for Sample #2). The dashed line in the upper panel indicates $\tau_0 \propto V^{-3/2}$ behavior for reference. (The symbol with the arrow indicates a fit for which the resonant frequency was effectively infinite, i.e. $\gg 4 \text{ kHz}$ .) . . . . . 100
Figure 3.21	Time dependence of the CDW current (top panels), reflectance adjacent to current contacts (center panels), and reflectance $100 \mu\text{m}$ from the contacts (bottom panels) for Sample #1 at $\nu = 860 \text{ cm}^{-1}$ . The horizontal arrows in the top panels indicate current overshoot. (a) Responses to $\Omega/2\pi = 253 \text{ Hz}$ square waves with magnitudes 110 mV, 150 mV, 300 mV. (b) Responses to 200 mV square waves of frequencies $\Omega/2\pi = 253 \text{ Hz}$ , 714 Hz, and 2011 Hz. . . . . 102
Figure 3.22	Frequency dependence of the in-phase and quadrature electro-reflectance for 78 mV (upper panel) and 110mV (lower panel) square waves for Sample #1, with light ( $\nu = 760 \text{ cm}^{-1}$ , perpendicular polarization) incident at $100 \mu\text{m}$ from the left contact. Asymmetric quadrature components make data unfittable with Equation 3.14. . . . . 105
Figure 3.23	Frequency dependence of the in-phase (upper panel) and quadrature (lower panel) electro-reflectance for 37 mV and 45 mV square waves for Sample #3, with light ( $\nu = 720 \text{ cm}^{-1}$ , parallel polarization) incident adjacent to the contact. Double peaks in quadrature become more visible at the lower voltages due to the size of $\Delta R/R$ signal. . . . . 106

# LIST OF FILES

1    rcraidis.pdf ..... 5.6 MB

# Chapter 1

## Introduction

### 1.1 Background

In this thesis, I will present and discuss the results of electro-optic measurements on the quasi-one-dimensional materials,  $K_{0.3}MoO_3$  (often called blue bronze because of its deep blue color) and orthorhombic-TaS<sub>3</sub>. The results are divided into three sections. The first section covers a search for narrow-band noise modulations of the infrared transmission of blue bronze. The second section covers the measurements of electro-reflectance spectra for light polarized both parallel and perpendicular to the conducting chains, including our search for signs of expected current-induced intragap states. The third section covers dynamical studies of electro-reflectance of ortho-TaS<sub>3</sub>.

A quasi-one-dimensional electron gas coupled to a phonon system is unstable at low temperatures, and undergoes a phase transition to a nonconducting state with a narrow gap in the electron energy band.<sup>1</sup> This type of a metal-insulator transition, first pointed out by Peierls in the early 1950s, is called a Peierls' transition. Below the Peierls transition temperature  $T_P$ , a charge density wave (CDW) is the ground state of many quasi-one-dimensional materials such as  $K_{0.3}MoO_3$  (potassium molybdenum oxide)<sup>2</sup>, NbSe<sub>3</sub> (niobium triselenide)<sup>3</sup>, TaS<sub>3</sub> (tantalum trisulfide)<sup>4</sup>. The ground state is a periodic lattice distortion and a periodic modulation of the charge density. In the CDW state, these anisotropic materials exhibit nonlinear conductivity, gigantic dielectric constants, unusual elastic properties and rich dynamical behavior.<sup>5</sup> The equilibrium CDW is pinned by a potential established by random defects and impurities. Small applied electric fields polarize the CDW, i.e. cause it to strain from its pinned configuration; above a depinning voltage,  $V_T$ , the CDW slides through the sample, carrying collective current.<sup>6</sup> Most of the unusual electronic properties are related to motion of the CDW in an applied field

greater than the threshold field needed to depin it. Due to the variety of unusual electronic properties associated with CDW depinning and motion, CDW materials have been the subjects of extensive theoretical and experimental studies.

The electro-optic effect of  $K_{0.3}MoO_3$ , which undergoes a phase transition into a semiconducting charge-density-wave (CDW) state at  $T_p = 180K$ <sup>7</sup>, was discovered in 1994 by Drs. Brill and Itkis. They reported that the infrared transmission( $\tau$ ) changed in an applied electric field.<sup>8</sup> The changes in transmission ( $\Delta\tau$ ) are thermally activated and vary with position in the sample: the transmission increases on the positive side of the sample and decreases on the negative. This electro-optic effect occurs for voltages  $V > V_p$ , the voltage at which one first observes CDW polarization, and they suggested that the electro-optic effect is caused by the polarization of the CDW state in the applied electric field. The changes in transmission signal are mostly associated with changes in the intraband absorption of thermally activated quasiparticles, whose density ( $n_{qp}$ ) changes to screen deformations of the CDW in the applied field:  $\Delta\tau/\tau \propto \Delta n_{qp} \propto \partial\phi/\partial x$ . where  $\phi$  is the CDW phase. The CDW materials exhibit a unique electro-optic effect which varies spatially throughout sample, occurs at extremely small electric field ( $\sim 100$  mV/cm), and occurs over a very wide (infrared) spectral range.

In this thesis, I will present results of experiments in which we use electro-optic techniques for the studies of the CDW states of  $K_{0.3}MoO_3$  and orthorhombic  $TaS_3$ . The electro-reflectance signal for blue bronze has been evidenced for the first time. For blue bronze, the electro-reflectance signal has been measured to be smaller than electro-transmittance signal by one order of magnitude for light polarized perpendicular to the chain direction. The electro-reflectance spectrum of blue bronze for light polarized parallel to the conducting chains has been examined for signs of expected current-induced intragap states and results have been presented in this thesis. Also results of search for narrow-band noise modulations of the infrared transmission of blue bronze have been discussed. In Chapter 3.3 of this thesis, the electro-optic response of ortho- $TaS_3$  has been used to study the dynamics of CDW polarization in an applied electric field and results have been analyzed and presented. A big electro-reflectance signal has

been observed in ortho-TaS<sub>3</sub> for the first time. As for blue bronze, the infrared reflectance of ortho-TaS<sub>3</sub> varies with position when a voltage above the threshold for CDW depinning is applied. The larger electro-optic effect for ortho-TaS<sub>3</sub> is encouraging for our study since it makes measurements on the tiny available crystals much easier.

## 1.2 Theory of Charge-Density-Wave Ground State

Consider a quasi-one dimensional metal with a linear chain of molecules separated by the distance  $a$ . The Hamiltonian of a one-dimensional coupled electron-phonon system is

$$H = \sum_{k,\sigma} \varepsilon_k a_{k,\sigma} a_{k,\sigma}^+ + \sum_{k,\sigma} \hbar \omega_{q_0} b_q^+ b_q + \sum_{k,q,\sigma} g(k) a_{k+q,\sigma}^+ a_{k,\sigma} (b_q + b_q^+) \quad (1.1)$$

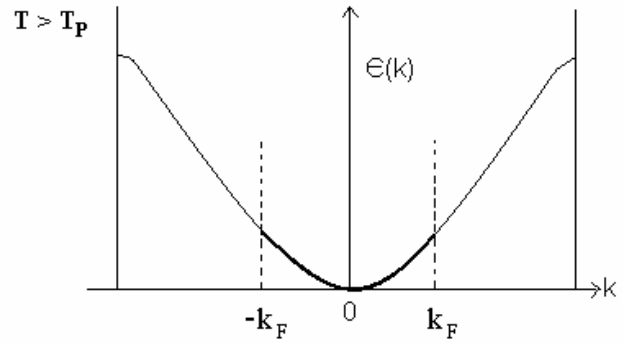
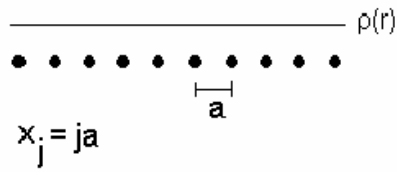
where  $a_k^+$  ( $a_k$ ) and  $b_q^+$  ( $b_q$ ) are the electron and phonon creation (annihilation) operators with momenta  $k$  and  $q$ ,  $\sigma$  is the spin,  $\varepsilon_k$  and  $\omega_{q_0}$  are the electron and phonon frequencies and  $g(k)$  is the electron-phonon coupling constant.

Peierls suggested that such a one-dimensional metal is not stable at low temperatures. The ground state is a charge-density-wave state (CDW) with a gap at the Fermi wave vector  $k_F$  as shown in Figure 1.1. The main features of the phase transition and CDW state can be described by the above Hamiltonian. Details of the theory can be found in the book ‘Density Waves in Solids’ by G. Grüner.<sup>9</sup> The single-particle energy gap\*  $\Delta$  is proportional to the amplitude of the lattice displacement  $\delta$  from the equilibrium position, and for small displacements the decrease of the electronic energy is proportional to  $\delta^2 \ln \delta$ . At the same time, the lattice distortion leads to an increase of the elastic energy which is proportional to the square of the lattice displacement,  $\delta^2$ . Therefore, the

---

\* Unlike a semiconductor for which the energy gap at the Fermi level is due to the ionic potential, and therefore bound to the crystal frame, the Peierls (CDW) energy gap is associated with a lattice deformation, which might move within the crystal.

a) One dimensional metal



b) Peierls distortion

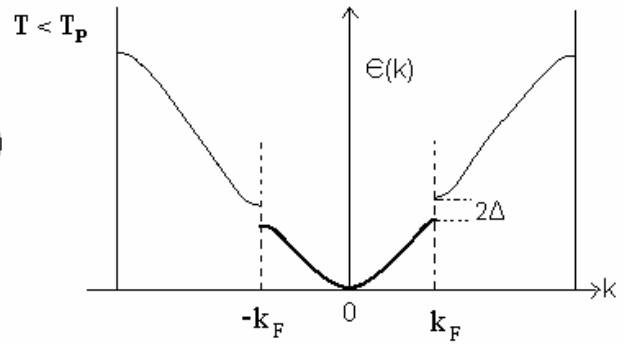
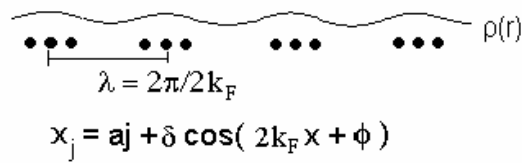


Figure 1.1 The band structure of a one-dimensional electron gas: (a) An undistorted system at  $T > T_P$ . (b) Peierls insulator at  $T < T_P$ . This figure is appropriate for a one-third filled band.



total energy  $\delta^2 \ln \delta + \delta^2$  decreases in the CDW ground state, and hence this CDW state is the preferred ground state for quasi-one-dimensional metals at low temperatures.

The electronic charge density associated with the collective mode is given by <sup>6</sup>

$$\rho(\vec{x}) = \rho_0 + \rho_1 \sin(2\vec{k}_F \cdot \vec{x} + \phi) \quad (1.2)$$

where  $k_F$  is the Fermi wave vector,  $\phi$  is the phase of the charge density modulation with respect to the lattice,  $\rho_0$  is the uniform electronic density, and  $\rho_1 = \frac{\rho_0 \Delta}{\lambda v_F k_F}$  is the amplitude of the charge density modulation ( $v_F$  is the Fermi velocity). The formation of the CDW state can be directly observed in X-ray experiments.

For strictly one-dimensional materials, there is no real phase transition and therefore  $T_p = 0$ . However the interchain coupling in a quasi-one dimensional material allows a three-dimensional phase transition to occur at  $T_p < T_p^{MF}$  (mean field transition temperature) and, Lee, Rice and Anderson <sup>10</sup> have calculated  $T_p \approx T_p^{MF} / 4$ .

The CDW can be either commensurate or incommensurate with respect to the underlying lattice. If the CDW period  $\lambda = \pi / k_F$  is a rational fraction of the lattice constant 'a', the CDW is commensurate and it has a preferred position. In many cases, the period ' $\lambda$ ' is incommensurate with the underlying lattice (i.e.  $\lambda$  is not a rational fraction of the lattice constant 'a'), and the phase ( $\phi$ ) can assume an arbitrary value for a perfect crystal. Therefore, an incommensurate CDW state does not have a preferred ground state and the ground state energy of the system would not change if the CDW is displaced. Because of this, Fröhlich <sup>11</sup> suggested that the ability of an incommensurate CDW to move freely in a crystal may be a possible mechanism of superconductivity. Instead, the CDW is usually pinned to the lattice by impurities, defects, or by its commensurability with the lattice, locking it into a preferred ground state <sup>6, 12</sup>.

Consequently, contrary to Fröhlich's expectation, the collective mode contribution to the dc conductivity at low electric fields is zero. However, if an electric field is applied that is strong enough to overcome the pinning potential of impurities, the CDW can be depinned and can slide in the crystal. The sliding of the CDW results in an increase of the conductivity of the crystal. This non-Ohmic behavior is a unique character of CDW (and related spin density wave) materials. The conductivity saturates at the value of its normal state due to scattering of the CDW from the normal electrons.

### 1.3 Pinning in the CDW State

The pinning mechanism plays a vital role in the static and dynamic properties of the CDW state. Pinning can be due to impurities, other crystal defects, commensurability or surfaces. Commensurability of CDWs with the underlying lattice makes CDWs virtually unmovable and fixed to the lattice. In incommensurate materials, randomly distributed impurities or defects are the reasons for the CDW pinning.<sup>13</sup> The pinning energy per electron is much smaller than the single-particle energies  $\Delta$  and  $\varepsilon_F$ . Because of this reason, the response to finite amplitude dc and to ac excitations is dominated by the dynamics of collective modes.

The pinning due to impurities in the crystals has been developed in the context of Fukuyama-Lee-Rice model of the CDW state. According to Fukuyama, Lee, and Rice (FLR) theory, impurities could pin an elastically deformable CDW, independent of the size of the impurity potential, and they introduce two types of pinning: strong and weak pinning.<sup>12, 14</sup> The impurity potential can change both the amplitude and the phase ( $\phi$ ) of the CDW condensate near the impurity site. There are two competing energies in the system, the impurity energy and the elastic energy. These two energies (per impurity) are given by

$$E_{imp} \approx V_0 \rho_1 \tag{1.3a}$$

$$E_{elas} \approx \hbar n_i v_F \tag{1.3b}$$

where  $\rho_1$  is the amplitude of the CDW modulation,  $n_i$  is the impurity concentration. The dimensionless parameter  $\epsilon = V_0\rho_1/\hbar n_i v_F$  distinguishes whether the impurity-density wave interaction or the elastic term is more important. For  $E_{imp} \gg E_{elas}$  case,  $\epsilon \gg 1$  and the impurity pinning is said to be strong. Strong pinning occurs either by a strong impurity potential or a low impurity density. In the strong pinning case, the phase  $\phi(x_i)$  is locked at each impurity site  $x_i$  so that the potential energy of the system becomes minimum. When  $E_{imp} \ll E_{elas}$  (i.e.  $\epsilon \ll 1$ ), the pinning is said to be weak impurity pinning. Weak pinning occurs either by a weak impurity potential or a high impurity density and the impurity potential is not strong enough to fix the phase at pinning centers but the system breaks into domains and the phase is pinned by a collective potential of impurities.

For both strong and weak pinning cases, long range phase coherence is destroyed and it leads to a finite phase-phase coherence length  $L_0$  (also known as FLR domain length). For large distances, the phase coherence is given by the equation,

$$\langle \phi(\vec{r}), \phi(0) \rangle \approx \exp(-\vec{r}/L_0) \quad (1.4)$$

For strong pinning, the phase coherence length  $L_0 \approx 1/r_i$  is the average distance between impurities since the phase is adjusted to the impurity positions at every impurity site. In the limit of weak pinning, the phase in a domain is on average rigid, but these domains are not separated by sharp domain walls but by a smooth change in the phase. Therefore the length scale over which the phase varies by one wavelength is much larger than the average distance between impurities. In three dimensions, the characteristic length  $L_0$  is given by<sup>9, 14</sup>

$$L_0 \approx \frac{(\hbar v_F)^2}{(3/4)^2 (V_0 \rho_1)^2 n_i} \quad (1.5)$$

i.e. the phase-coherence length is inversely proportional to the impurity concentration  $n_i$ . Detail theoretical derivations can be found in References <sup>9, 12, 14</sup>. In general, for weak pinning, the FLR domain contains many impurities and for strong pinning, the domain contains one impurity which fixes the CDW phase. The typical size of the (weak pinning) phase coherence length in the chain direction is  $0.3 \mu\text{m}$  for nominally pure ortho-TaS<sub>3</sub> <sup>15</sup> and  $> 0.7 \mu\text{m}$  for blue bronze <sup>16</sup>. However due to the anisotropic nature of the material, the phase coherence length in the transverse direction is one or two order of magnitude smaller than its value in the chain direction. Therefore, a typical sample with a length of 1 mm contains at least  $10^4 - 10^6$  domains.<sup>17</sup> The FLR theory also predicted that the threshold field depends on impurity concentration ( $n_i$ ) by  $E_T \sim n_i$ , for strong pinning, and  $E_T \sim n_i^2$ , for weak pinning.<sup>10</sup> The dependence of threshold field on impurity concentration has been supported by experimental results.<sup>6</sup>

In the dynamic state, a pinned CDW breaks up into regions of uniform phase velocity and it is more appropriate to describe the CDW state by a velocity coherence length. The dynamic phase-phase coherence length is much shorter than the velocity-velocity coherence length. Fisher suggested that the velocity coherence length diverges near threshold as the velocity of the CDW goes to zero so that the behavior near threshold is a dynamic critical phenomenon.<sup>18</sup> That is, near threshold, the velocity coherence length is comparable to the total length of the sample. In this case the CDW velocity is uniform in time and space in the bulk of the sample.

## 1.4 Phase Slip Processes

In quasi-one dimensional charge-density-wave (CDW) materials like NbSe<sub>3</sub>, TaS<sub>3</sub>, K<sub>0.3</sub>MoO<sub>3</sub>, the presence of coherent voltage oscillations (narrow-band noise, NBN) appears when the applied field exceeds a threshold value.<sup>2, 19, 20</sup> The voltage oscillation phenomenon of these materials has been considered to be a signature of the collective motion of the electrons. The narrow-band noise frequency ( $f_{CDW}$ ) is proportional to the

CDW current ( $I_{CDW}$ ), (i.e.  $f_{NBN} = v_{CDW} / \lambda \propto I_{CDW}$ , where  $v_{CDW}$  is the velocity of the CDW,  $\lambda$  is the CDW wavelength) and this linear relationship between them provides direct evidence that it arises from sliding CDWs. However, the physical mechanism for the voltage oscillations has been strongly debated,<sup>21</sup> as discussed in Section 3.1. Our attempt to search for narrow-band noise modulations of the infrared transmission of blue bronze in the context of finding the associated physical process of NBN is also presented in Chapter 3.1 of this thesis.

The idea of phase-slip process in reference to quasi-one dimensional conductors with CDW state has been introduced independently by Ong, Verma, and Maki<sup>22</sup>, and Gor'kov<sup>23</sup> to explain the mechanism of narrow-band noise (NBN) generation. The phase-slip process can be thought of as the way the CDW reduces stress that is built up by the dc electric field. The phase is considered to be fixed at the end of the sample. A sliding charge-density wave moving towards the contact tries to compress the CDW near the contact because of this boundary condition. If CDW wave fronts were not removed periodically at one contact and injected at the other, a large phase difference would build up very quickly across each contact and this would destroy the condensed state. However the stress built up by phase difference is released by introducing an array of phase vortices or dislocations which moves along the phase boundary perpendicular to the sample length.<sup>22</sup> This mechanism of releasing stress in the system by phase slippage method at the electrical contact is referred to as the phase-slip process. It is believed that continuous phase-slip process provides the conversion of single-particle (normal) current into CDW current (and vice-versa) near contacts, and it was suggested that it causes in the generation of the periodic voltage oscillations when the current is regulated.<sup>22</sup>

Although the explanation based on the vortex model for the origin of narrow-band noise remains controversial, there have been experimental evidences for phase-slip processes in the CDW state. (The competing bulk model for the origin of NBN is discussed in Chapter 3.1.) Recently, Requardt et al. have reported the results of spatially resolved synchrotron X-ray studies in NbSe<sub>3</sub> and they observed the associated deformation profile near contacts.<sup>24</sup> Similarly, in electromodulated transmission

measurement, the extra changes in transmission assumed to be proportional to the contact strain which drives phase-slip process appears within distance of  $\sim 100 \mu\text{m}$  from the contacts for blue bronze.<sup>25</sup> Since phase-slip is required for conversion between CDW current and single-particle current at the contacts, it plays a central role in CDW transport.

As mentioned above, the contact strains are believed to drive CDW phase-slip through the growth and climb of macroscopic CDW dislocation loops. However, the actual formation of the dislocation loops is poorly understood. A proposed microscopic picture of the current conversion process and formation of dislocation loops is as follows: when an electron enters a CDW chain, it forms a  $\pi$ -soliton state with energy near the center of the CDW gap. This process is equivalent to a local phase change by  $\pi$  in the CDW condensate. These  $\pi$ -solitons are expected to quickly ( $\approx 1$  ps) pair into  $2\pi$ -solitons, with energy levels near the edge of the gap.<sup>26</sup> Therefore,  $2\pi$ -solitons as shown in Figure 1.2 correspond to 2 electrons entering or leaving the CDW at contacts. Dislocation loops are thought to form from the condensation of  $2\pi$ -phase-solitons on the individual chains. A microscopic illustration of formation of  $\pi$ -phase-solitons,  $2\pi$ -phase-solitons, and phase-slip nucleation are shown in Figure 1.3. It is not known how quickly these  $2\pi$ -solitons coalesce into dislocation lines and whether their energies remain well-defined (within  $k_B T_p$ ) near the gap edge, or whether they oscillate through the gap<sup>27</sup>. Furthermore, such current-induced intragap soliton/dislocation states have not been observed, although related states arising as growth defects upon cooling or doping may have been seen spectroscopically.<sup>28, 29</sup>

Solitons play a central role in the transport properties of a doped conducting polymer, polyacetylene, which has a large band gap of  $\sim 1.5$  eV. The midgap state associated with the soliton in doped polyacetylene was seen by optical absorption as appearance of the midgap absorption.<sup>30, 31</sup> The soliton theory of polyacetylene is well established now. Even though solitons in doped polyacetylene and quasi-one dimensional conductors may have different origins, their basic mathematical description

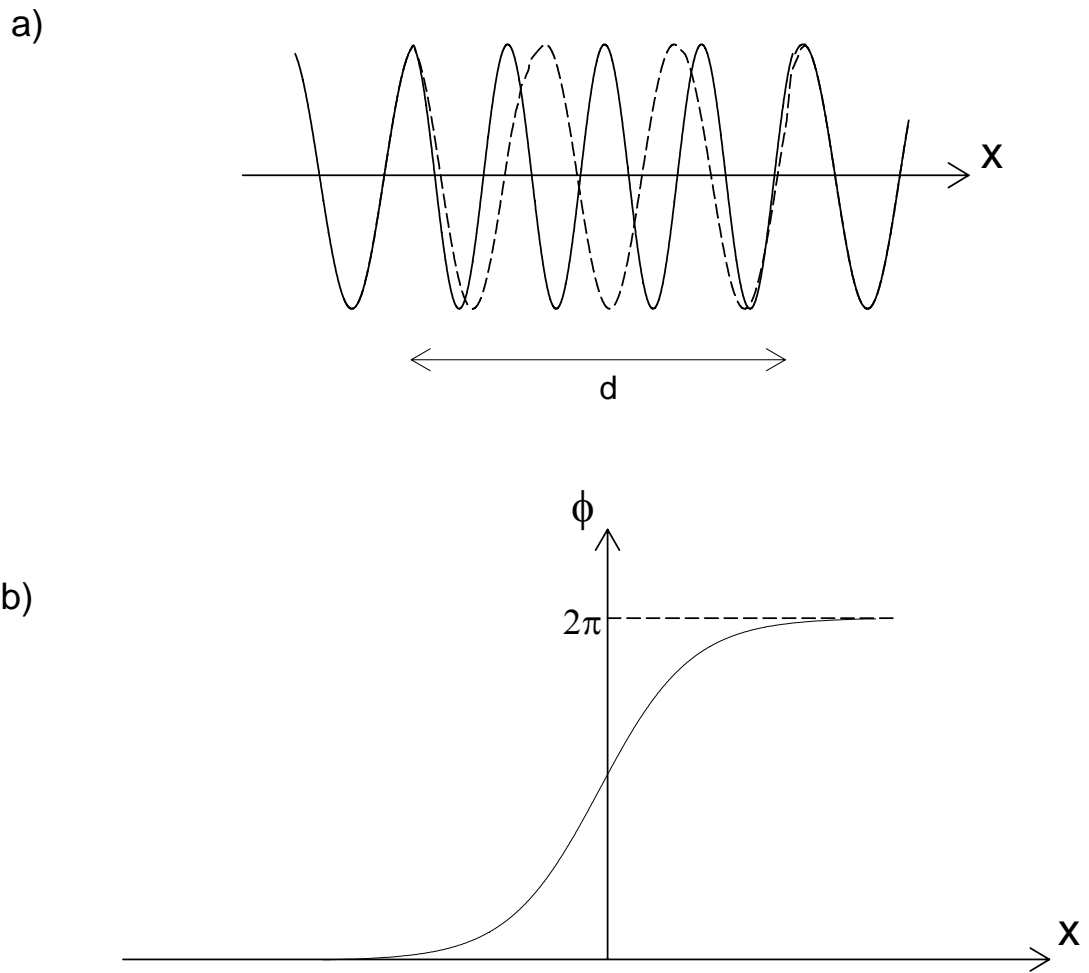


Figure 1.2 (a) A charge-density wave with a local distortion in the phase (full line), and dashed line is undistorted CDW. (b) Spatial dependence of the phase  $\phi$ .

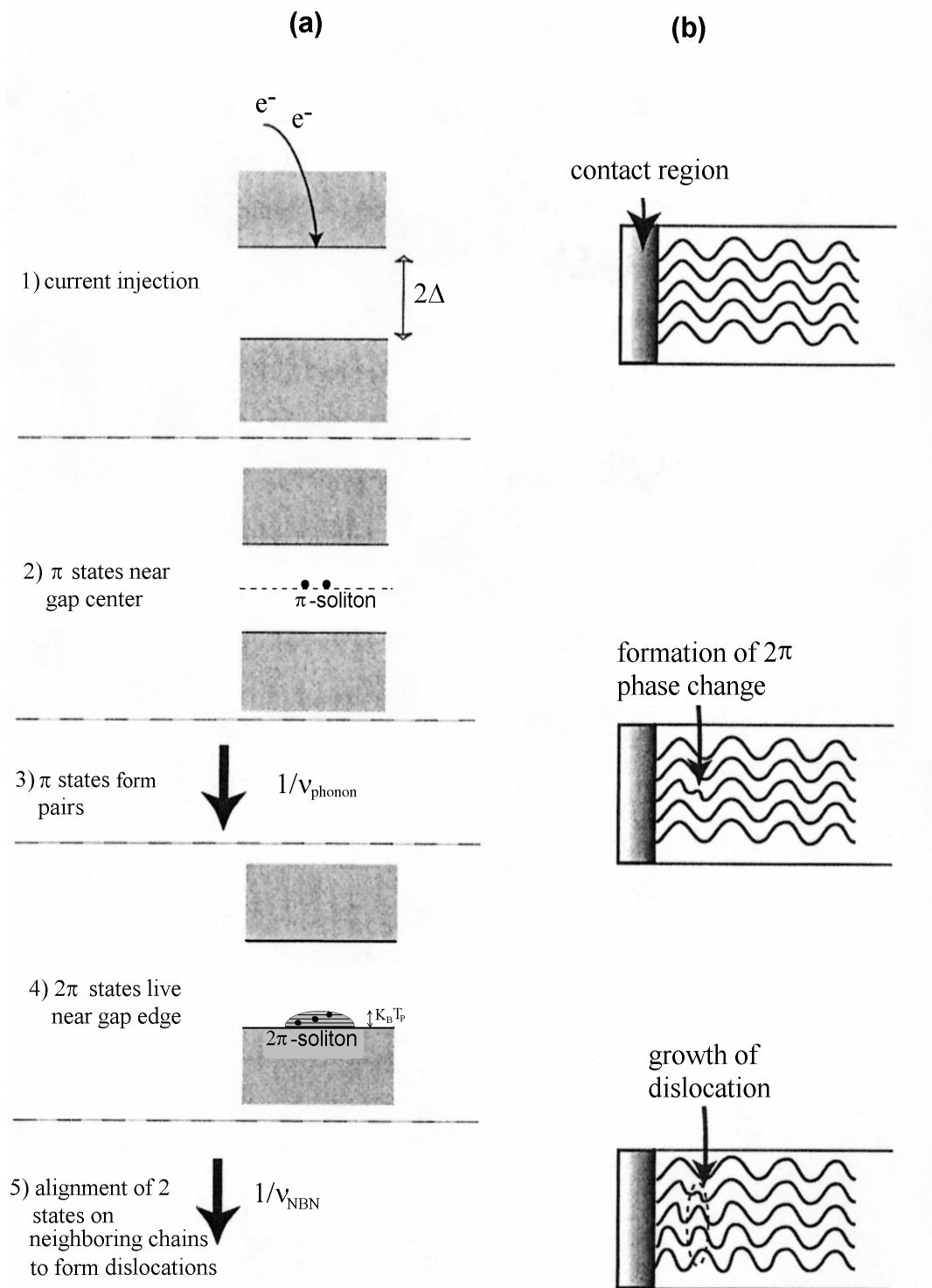


Figure 1.3 <sup>32</sup> (a) Energy bands for current conversion sequence. (b) Dislocation nucleation sequence in current conversion process.



is similar. Therefore, an important open question to address is whether solitons in a CDW state occur and if so, are they optically excitable? The electro-optic (reflectance) spectroscopy can be used to search for midgap (soliton) states associated to current conversion processes at contacts in a CDW conductor.

## 1.5 Review of Physical Properties of $K_{0.3}MoO_3$

The bronzes with stoichiometric composition and chemical formula of  $A_{0.3}MoO_3$ , where  $A = K, Rb, \text{ or } Tl$ , are quasi-one-dimensional metals with a deep blue appearance.<sup>33</sup> The schematic structure of  $K_{0.3}MoO_3$  is shown in Figure 1.4. The structure of the blue bronzes is built up from chains of  $MoO_6$  octahedra, separated by chains of alkali metal atoms, leading to a quasi-one-dimensional electronic band structure. The  $MoO_6$  layers are built by clusters of ten edge and corner sharing octahedra connected by corner sharing along the  $[010]$  and  $[102]$  directions. The monoclinic unit cell contains two clusters or 20 formula units. The single crystals of blue bronze cleave in a plane parallel to the monoclinic  $b$  axis and the  $[102]$  direction. The infinite chains of  $MoO_6$  along the crystallographic  $b$ -direction results anisotropy in conductivity,  $\sigma_b : \sigma_{[102]} : \sigma_{[201]} \approx 1 : 0.1 : 0.001$  at all temperatures<sup>33, 34</sup>, as shown in Figure 1.5a. Since the stoichiometry of the blue bronzes is exact, i.e.,  $K_{0.3}MoO_3$ , three electrons are transferred to the  $Mo_{10}O_{30}$  bands to partially fill them.  $K_{0.3}MoO_3$  has an approximately 3/4 filled conduction band at room temperature<sup>35</sup>. The metallic conductivity of  $K_{0.3}MoO_3$  for temperatures above  $T_P$  is due to the K ions which donate their electrons to the Mo 4d conduction band.

The blue bronzes undergo metal-insulator (MI) transitions at 180K as shown in Figure 1.5.<sup>36</sup> This MI transition has been attributed to a coupled instability of the conduction electrons and phonons at  $2k_F$ . Below the transition temperature  $T_P$ , all conduction electrons except thermally excited quasiparticles condense into the collective CDW state<sup>6</sup>, the Fermi surface is completely destroyed, and the material behaves like a narrow gap semiconductor. The single-particle energy gap ( $2\Delta$ ), which is temperature

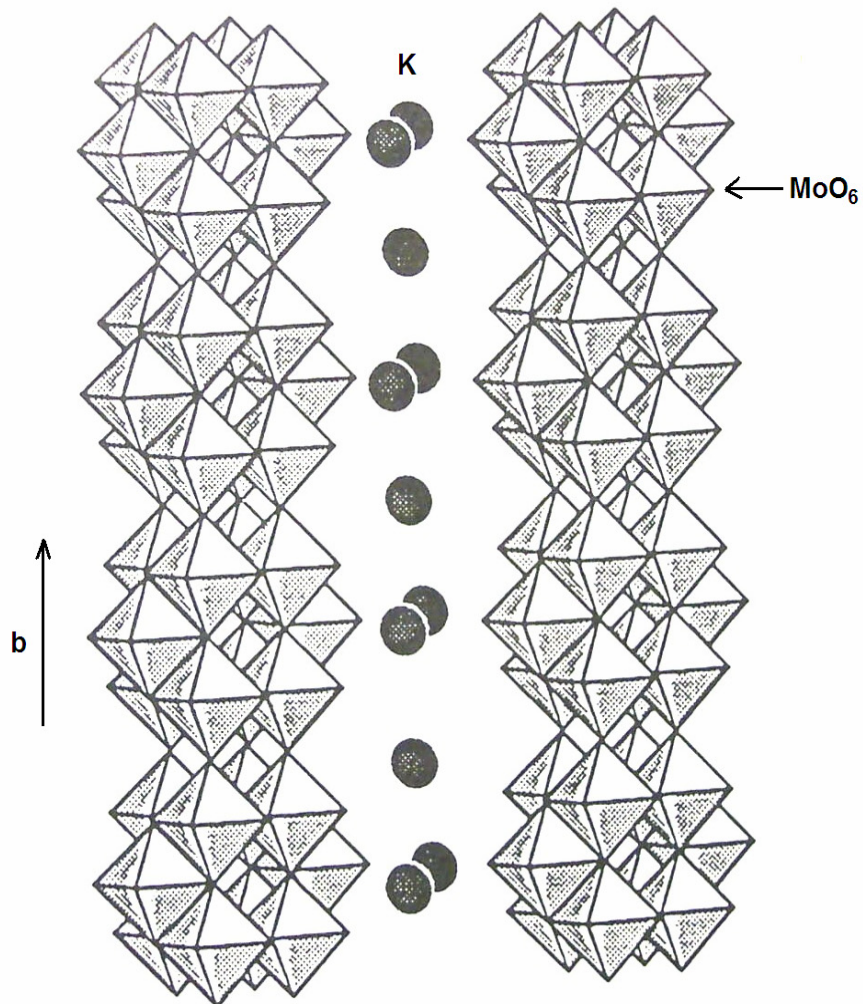


Figure 1.4 Linear chains of MoO<sub>6</sub> octahedra along the monoclinic b axis in blue bronze. Unit cell parameters at room temperature:  $a = 18.249 \text{ \AA}$ ,  $b = 7.560 \text{ \AA}$ ,  $c = 9.855 \text{ \AA}$ , and  $\beta = 117.53^\circ$ . (From reference <sup>36</sup>)

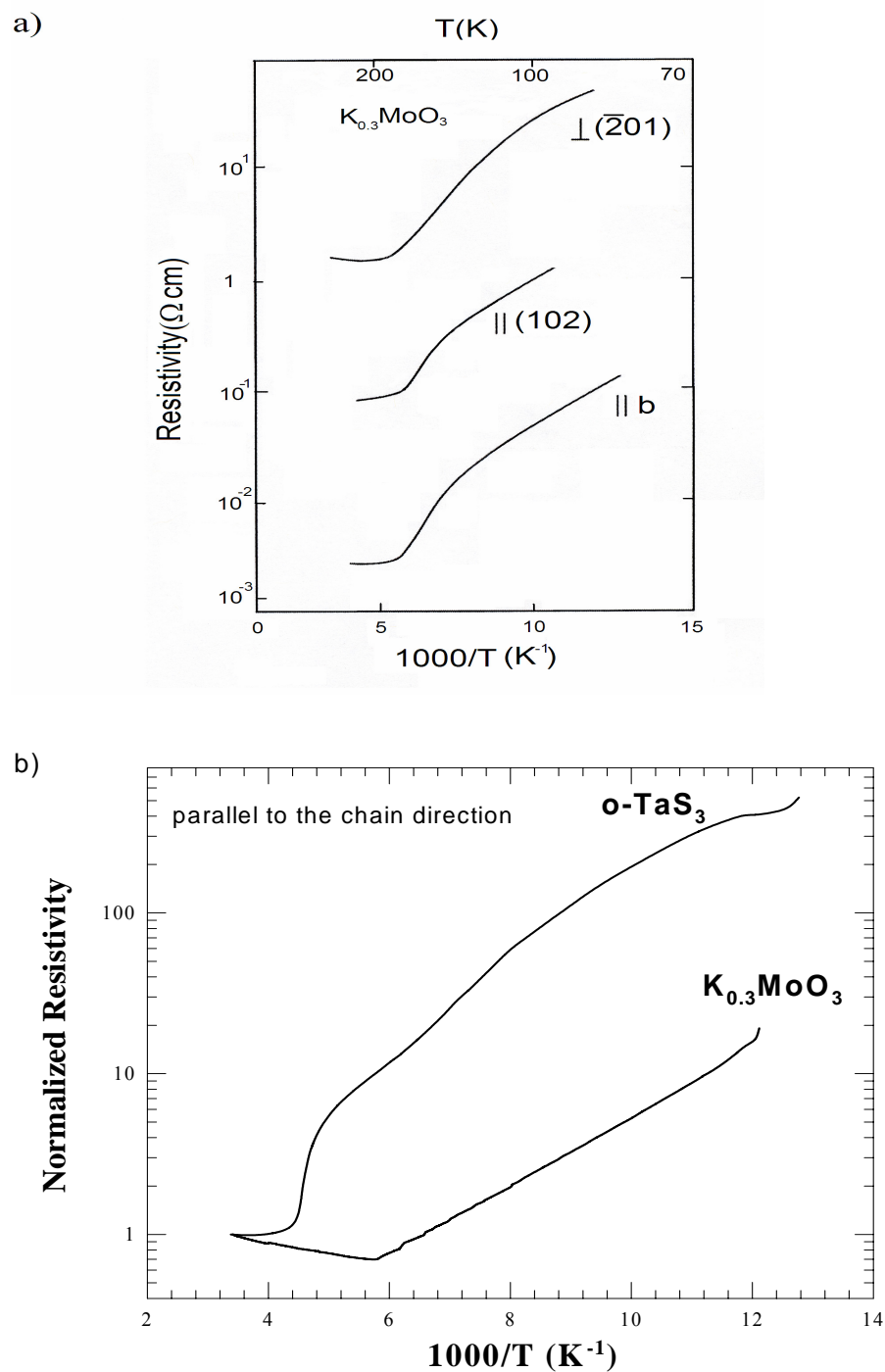


Figure 1.5 (a) Resistivity of  $K_{0.3}MoO_3$  as a function of  $1000/T$  along the b-direction, along  $[102]$  direction, and perpendicular to  $[\bar{2}01]$  direction<sup>36</sup>. (b) Normalized resistivity of ortho-TaS<sub>3</sub> and  $K_{0.3}MoO_3$  as a function of  $1000/T$  along the b-direction (measured in our lab).

dependent, has not been determined unambiguously. For example, the estimated value of the gap from transport measurement<sup>37</sup> and magnetic susceptibility measurement<sup>38</sup> is about  $800\text{ cm}^{-1}$ , from tunneling spectroscopy<sup>39</sup> is  $1050\text{ cm}^{-1}$ , from the IR absorption edge<sup>40</sup> is  $1150\text{ cm}^{-1}$ , and from a model fit to the infrared spectrum<sup>41</sup> is  $1400\text{ cm}^{-1}$ . Perhaps some of the inconsistencies in the experimental results of the gap may be due to the fact that fluctuations broaden the edge and different experiments may take different averages.

## 1.6 Review of Physical Properties of TaS<sub>3</sub>

The transition metal trichalcogenides, MX<sub>3</sub> (where M = Ta, Nb, X = S, Se) compounds are composed of linear chains built up by chalcogen trigonal prisms stacked along a metallic chain axis as shown in Figure 1.6. This linear chain structure results in highly anisotropic electronic properties due to the overlap of the electronic orbitals in the chain direction and poorer overlap in transverse direction. MX<sub>3</sub> has an approximately quarter filled electron band involving the d-orbitals of the transition metal atoms.

Tantalum trisulfide exists in two crystallographic forms, one with a monoclinic unit cell<sup>42</sup> with a structure similar to that of NbSe<sub>3</sub>, as shown in Figure 1.6a, and the other with an orthorhombic unit cell structure whose structure has not been determined yet in spite of many attempts. From the original work by Bjerkelund and Kjekshus<sup>43</sup>, the unit cell parameters of ortho-TaS<sub>3</sub> are;  $a = 36.804\text{ \AA}$ ,  $b = 3.340\text{ \AA}$ ,  $c = 15.173\text{ \AA}$ . The structure of ortho-TaS<sub>3</sub> is believed to be composed of linear chains built up by chalcogen trigonal prisms. Meerschaut and Rouxel<sup>36, 42</sup> proposed a model of the structure of ortho-TaS<sub>3</sub> as shown in Figure 1.6b. According to the proposed model, its orthorhombic unit cell contains 24 chains (or 96 atoms) compared to 6 chains in the monoclinic structure.

Monoclinic TaS<sub>3</sub> undergoes two phase transitions at temperatures  $T_{p1} = 240\text{ K}$  and  $T_{p2} = 160\text{ K}$ . The first transition is a metal-semiconductor and second transition is a semiconductor-semiconductor.<sup>36</sup> Orthorhombic TaS<sub>3</sub> undergoes a single Peierls transition<sup>4</sup> at temperature  $T_P = 220\text{ K}$  as shown in Figure 1.5b. Below  $T = 130\text{ K}$ , the charge-density wave (CDW) is approximately commensurate with the underlying lattice

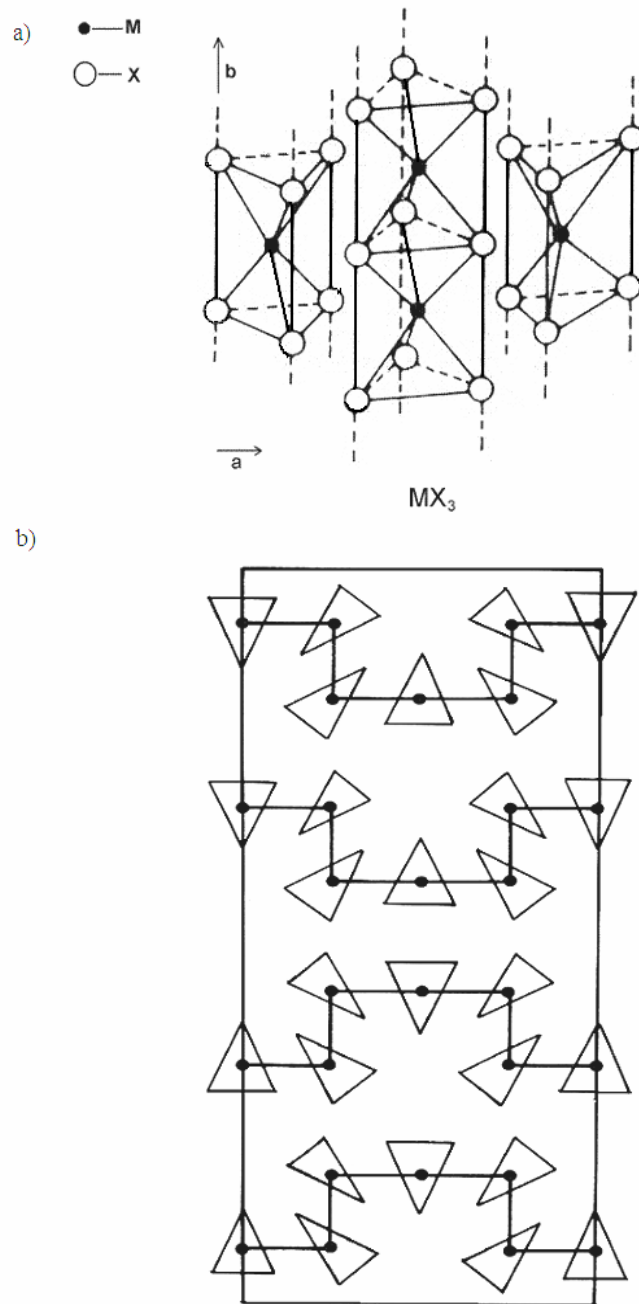


Figure 1.6<sup>17</sup> (a) Structure of NbSe<sub>3</sub>. Three linear chains with slightly different values of X-X bond lengths are shown here. (b) A model for the unit cell of the orthorhombic TaS<sub>3</sub>. Each unit cell has 24 chains roughly similar to the chains in NbSe<sub>3</sub> structure, but the detailed structure of the chains has not been determined.<sup>36</sup>

and has a periodicity close to  $4c$ , where  $c$  is the lattice constant along the chain direction.<sup>3</sup> Our electro-optic work has been limited to orthorhombic TaS<sub>3</sub> because of the availability of the crystals.

The conductivity of ortho-TaS<sub>3</sub> is highly anisotropic at room temperature<sup>44</sup>,  $\sigma_{\parallel} : \sigma_{\perp 1} : \sigma_{\perp 2} \approx 150 : 1 : 0.2$ . In order to estimate the Peierls gap  $2\Delta$ , the dc conductivity below  $T_p$  is expressed approximately by

$$\sigma_{\parallel} = \sigma_{\parallel}^0 \exp(-\Delta(T)/k_B T) \quad (1.6)$$

where  $\sigma_{\parallel}^0$  is the dc conductivity above  $T_p$ . The gap  $2\Delta(T)$  value, which is temperature dependent as expected from the mean-field theory, reported from the bolometric measurement was  $1240 \text{ cm}^{-1}$  at  $T = 21 \text{ K}$ <sup>45</sup>. With this gap value, the mean-field transition temperature is  $T_{MF} = E_g(T = 0K)/3.5k_B = 504 \text{ K}$ . For a one-dimensional band, the CDW transition is expected to be suppressed (to  $\sim T_p \sim T_{MF}/4$  in the simple model<sup>13</sup>) by large 1-D fluctuations.

Much attention has been devoted to ortho-TaS<sub>3</sub> since T. Sambongi et al.<sup>4</sup> reported the Peierls transition in this material in 1977. The non-Ohmic conductivity of ortho-TaS<sub>3</sub> with a sharp threshold field and a giant dielectric constant in the CDW state were reported by A. H. Thompson et al.<sup>46</sup> in 1981. This strongly non-linear conductivity is a result of depinning the CDW from the lattice when the voltage across the sample exceeds the pinning potential. Frequency dependent conductivity<sup>47</sup>, narrow-band noise oscillations<sup>48</sup> in sliding CDW, memory effects and metastable states associated with the CDW condensate have been reported for ortho-TaS<sub>3</sub>. A strong absorption doublet<sup>28</sup> observed with bolometric spectroscopy<sup>49</sup> at  $500 \text{ cm}^{-1}$  was associated with soliton absorption<sup>50</sup>. Therefore, ortho-TaS<sub>3</sub> has been considered to be a good candidate to search for intragap (soliton) states in the past. While solitons are believed to be created at current contacts, such solitonic states associated with current conversion processes at the current contacts have not been observed.

For the first time, we have observed the electro-optic effect in ortho-TaS<sub>3</sub>. The electro-reflectance signal with a size up to ~3 % for light polarized parallel to the chain direction has been seen in the sliding CDW state of ortho-TaS<sub>3</sub>. The electro-optic effect in ortho-TaS<sub>3</sub> is larger than electro-optic effect in K<sub>0.3</sub>MoO<sub>3</sub> by two orders of magnitude for parallel polarized light.

We attempted to investigate the electromodulated spectrum on ortho-TaS<sub>3</sub> but we were not able to get reproducible spectra. The small widths of twinned crystals and their generally faceted and stepped surfaces make spectroscopic measurements very difficult and non reproducible. However, the dynamics of electro-reflectance can be studied even for samples for which spectra can not be obtained. Indeed, the electro-optic response allows one to study the dynamics of CDW polarization without introducing possible perturbations from multiple contacts. Thus, the dynamical studies of electro-reflectance have been done on ortho-TaS<sub>3</sub>, the results of which are presented in Chapter 3.3 of this thesis.

## **1.7 Review of Electro-optic Effect in Blue Bronze**

As discussed in Section 1.5, the quasi-one dimensional metal, blue bronze (K<sub>0.3</sub>MoO<sub>3</sub>) undergoes a metal-insulator (MI) transition at 180 K. The ground state is the charge-density wave (CDW) state with a variety of unusual electronic properties <sup>6</sup> such as non-Ohmic conductivity, gigantic dielectric constants, unusual elastic properties, various memory effects, and rich dynamical behavior etc. Most of the unusual properties are associated with sliding of the CDW in an applied electric field greater than the threshold needed to depin it from the impurity potential. Along with all these unusual properties, blue bronze exhibits a novel electro-optic effect in which it changes its optical properties in the sliding CDW state.

The very first report of Drs. Brill and Itkis <sup>8</sup> on the electro-optic effect was the change in infrared transmission ( $\tau$ ) with photon energy less than the CDW gap; the transmission increases near the positive contact and decreases near the negative contact in

the CDW state. The relative changes in infrared transmission ( $\Delta\tau$ ) were found to be thermally activated, suggesting that the electromodulated transmission was associated with changes in the intraband absorption of quasiparticles  $n_{qp}$ , whose density changes to screen deformation of the CDW in the applied field. Since the relative changes in transmission varied with position in the sample i.e.  $\Delta\tau/\tau \propto \Delta n_{qp} \propto \partial\phi/\partial x$ , where  $\phi$  is the CDW phase,  $\Delta\tau/\tau$  could be used to probe the local gradient of the CDW phase  $\phi$ , in the applied electric field. In a 5  $\mu\text{m}$  thick blue bronze crystal, electromodulated transmission signal as large as  $\sim 1\%$  was reported.<sup>8</sup> Because of the anisotropy in conductivity, both  $\tau$  and  $\Delta\tau$  were essentially polarized perpendicular to the conducting chains for unpolarized incident light.<sup>51</sup>

Most of the electro-optic measurements were done on cleaved single crystal samples by applying square wave voltage pulses while illuminating the sample with chopped infrared light. The applied voltage pulses were either (symmetric) bipolar or unipolar square wave voltages. The infrared light sources used were a broadband source (globar) and tunable diode lasers covering a spectral region  $400\text{ cm}^{-1}$  to  $1300\text{ cm}^{-1}$ . All the previous electro-optic measurements on blue bronze were done for light polarized perpendicular to the chain direction of the blue bronze. The detector (a Zinc doped Germanium photodetector) signal was measured simultaneously with two lock-in amplifiers, usually operating in parallel mode. The first lock-in, operating at the chopping frequency, measured the transmitted intensity and the second lock-in, operating at the square wave frequency, measured the changes in transmitted intensity in the applied field. The ratio of two lock-in amplifier readings is the electromodulated transmission signal  $\Delta\tau/\tau$ . Here, the change in transmission measured with bipolar voltages ( $\pm V$ ) is represented by

$$\Delta\tau = \tau(+V) - \tau(-V) \tag{1.7}$$

and the change in transmission measured with unipolar voltages is represented by



$$\Delta\tau = \tau(V) - \tau(0) \quad (1.8)$$

It is clear that the magnitude of  $\Delta\tau$  signal is directly proportional to the magnitude of  $\tau$  signal for a fixed voltage at one frequency. Although the lock-in amplifier readings do not represent the absolute values of  $\tau$  and  $\Delta\tau$ , their ratio  $\Delta\tau/\tau$  is self normalized.

### 1.7.1 Spatial and Voltage Dependences of the Electro-optic effect

The electro-transmission of blue bronze does not appear until the applied field is strong enough to polarize the CDW state; the effect usually peaks at the dc threshold field and starts decreasing in magnitude with higher field as shown in Figure 1.7a. The solid line shows the current as a function of voltage across the sample. Above threshold  $V_T$ , the CDW is sliding and the current becomes nonlinear with excess current  $I_{CDW} = I - V/R_0$ , where  $I$  is total current,  $V$  is the voltage across the sample and  $R_0$  is the Ohmic resistance of the sample. The onset of electromodulated transmission ( $\Delta\tau/\tau$ ) indicates that the CDW state is macroscopically polarized<sup>25</sup> (i.e. strained) at a voltage  $V_p < V_T$ . Also the spatial dependences of  $\Delta\tau/\tau$  at different voltages are shown in Figure 1.7b. For  $V_p < V \leq V_T$ , the CDW overcomes pinning in the bulk of the sample but still remains pinned at the contacts. In this case,  $\Delta\tau/\tau$ , due to the bulk polarization, varies linearly with position, changing sign in the center of the sample. This linear dependence implies that the strain in the CDW state is a linear function of position (i.e.  $\partial\phi/\partial x$ ) below or at threshold. For  $V > V_T$  however, the CDW depins at the contacts as well and the current conversion process occurs at the contacts. Therefore, the additional strains in  $\Delta\tau/\tau$  which appear in narrow regions ( $\sim 100 \mu\text{m}$ ) near the contacts are associated with phase-slip processes needed for current conversion from normal to the CDW current and vice versa.<sup>25</sup> It is obvious that the contact strain becomes more prominent with increasing voltage since phase-slip processes occur with ease at higher voltages.

The open and closed symbols in Figure 1.7a show the electromodulated transmission at two positions at the end of the sample. Qualitatively, the difference

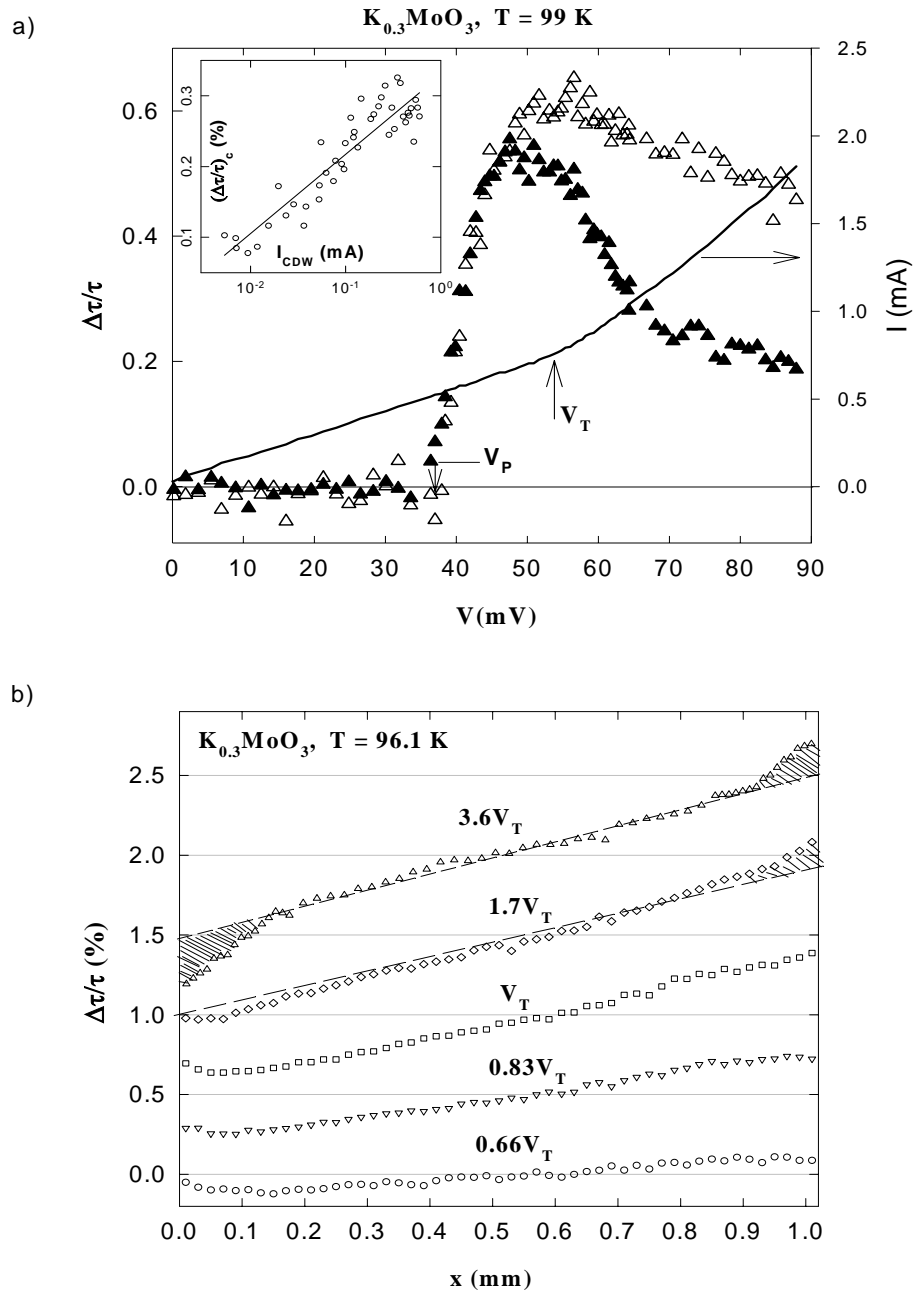


Figure 1.7<sup>25</sup> (a) Open and closed triangles show electromodulated transmission at  $x = 1.02$  (the end of the sample) and  $0.80$  mm, respectively, for a sample at  $99$  K; Solid curve shows current vs voltage. (b) Spatial dependence of the electromodulated transmission at different voltages for a different sample. Data for successive voltages are vertically offset by  $0.5\%$  for clarity. Dashed curves show the approximate bulk strains and shading shows the contact strains.

between these signals  $(\Delta\tau/\tau)_C$  is approximately the contact contribution and it is plotted versus  $I_{CDW}$  as shown in the inset. The contact contribution is logarithmically proportional to the CDW current  $I_{CDW}$ , consistent with studies done on  $NbSe_3$  in which the rate of phase slip, and therefore  $I_{CDW}$  was considered to be an exponential function of the strain.<sup>32</sup> Therefore, the nonlinear current appears to only depend on the contact deformation not associated with the bulk polarization. It was also reported that the contact and the bulk electromodulated transmission signals have different temperature dependence in blue bronze.<sup>25</sup> Below 100 K, both components decrease because the density of quasiparticles which screens the CDW deformation goes down with decreasing temperature. However, above 100 K, the bulk component  $(\Delta\tau/\tau)_B$  falls rapidly with increasing temperature whereas the contact component  $(\Delta\tau/\tau)_C$  only falls slowly with increasing temperature, again suggesting that the screening charge depends primarily on the rate of current conversion. The disappearance of the bulk component at higher temperatures suggests that the phase-slip processes occur relatively with ease in the bulk.

In addition to spatial and voltage dependences, the electro-optic effect in blue bronze exhibits frequency (i.e. of the applied bipolar voltage) dependent behavior. While the bulk deformation seems to grow out of the contact deformation, they have very different dynamics.<sup>25</sup> It was observed that the contact component which is small and localized was much faster than the bulk component in blue bronze. The observed time constant for the bulk component was on the order of 100  $\mu s$  and for the contact component was less than 10  $\mu s$ .

### 1.7.2 Theory of the Electro-optic Effect for Blue Bronze

Blue bronze in its CDW state exhibits a unique electro-optic effect which varies spatially throughout sample, occurs at a small voltage  $V_p$  which corresponds to the threshold for depinning in the bulk of the sample, and occurs over a very wide spectral range below the CDW gap<sup>52</sup> as shown below in Figure 1.10 The observed polarity dependence of  $\Delta\tau/\tau$  as shown in Figure 1.7b indicates that it is caused by strain and not

by current. In other words, the electro-optic effect in the CDW state is caused by the polarization of the CDW in an electric field. The fact that the electromodulated transmission is observed for all photon energies below the gap suggests that it is caused by intraband absorption of the quasiparticles screening the deformations.<sup>8</sup> The model for the electro-optic effect in blue bronze is shown in Figure 1.8. This model is based on an idea of the energy band bending and redistribution of quasiparticles in the presence of external electric field. With applied field  $V > V_p$ , the CDW state is compressed at the positive contact and rarified at the negative contact, shifting the chemical potential and concentration of quasiparticles. In blue bronze, the dominant quasiparticles are electrons<sup>37</sup>, which will accumulate at the negative contact to screen the CDW deformations. Therefore, the transmission signals decrease at the negative contact and increase at the positive contact of the sample as observed in the experiment. Mathematically, a change in the density of the CDW condensate  $\Delta n_{CDW}$  (which is equal and opposite to the change in the density of quasiparticles  $\Delta n_{qp}$ ) is represented as<sup>6,51</sup>

$$\Delta n_{CDW} = (1/\pi\Omega) \partial\phi/\partial x = -\Delta n_{qp} \quad (1.9)$$

where  $\phi$  is the CDW phase and  $\Omega$  is the area/conducting chain. Neglecting multiple internal reflections, the transmission for near normal incidence is given by

$$\tau \approx (1-R)^2 \exp(-\alpha d) \quad (1.10)$$

so that

$$\Delta\tau/\tau = -2\Delta R/(1-R) - d\Delta\alpha \quad (1.11)$$

where  $R$  is the reflectivity,  $\alpha$  is the absorption coefficient, and  $d$  is the thickness of the sample. However the electromodulated reflectance signal is expected to have a relatively weak dependence on the quasiparticle density and it is mostly dominated by the phonon lines, which is discussed elsewhere in Section 3.2. Therefore neglecting changes in  $R$ , the electromodulated transmission signals due to the changes in the quasiparticle density can be written as

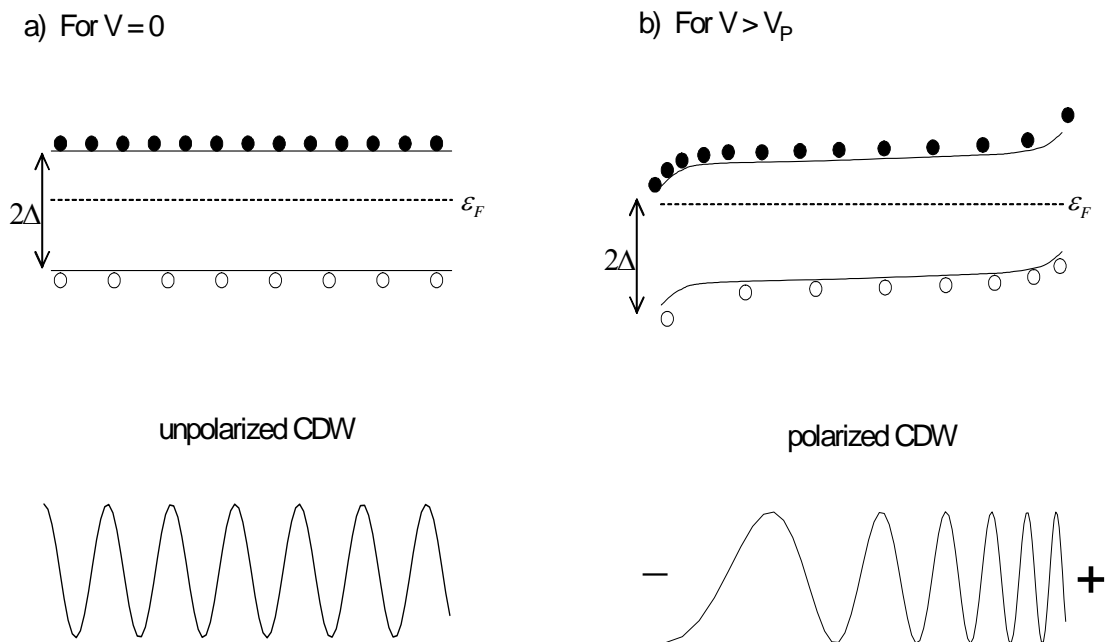


Figure 1.8 Closed and open circles represent electrons and holes. The  $\epsilon_F$  is the Fermi energy. (a) An undistorted CDW state and its energy band without any external field. (b) Polarization of the CDW state in the presence of an external field and resulting band bending near the gap, causing changes in quasiparticle density.

$$\Delta\tau/\tau \propto \Delta\alpha \propto \Delta n_{qp} = (1/\pi\Omega) \partial\phi/\partial x \quad (1.12)$$

$$\therefore \Delta\tau/\tau \propto \partial\phi/\partial x \quad (1.13)$$

This implies that the electromodulated transmission signals due to the intraband absorption of quasiparticles are directly proportional to the phase gradient of the CDW state. However  $\Delta\tau/\tau$  is not completely caused by intraband absorption of quasiparticles, but the changes in phonons due to the CDW deformation have also contributed to the electromodulated transmission in blue bronze. The electro-optic effect due to phonons will be discussed in Section 1.7.4.

The profile of  $\Delta\tau/\tau$  in blue bronze is similar to the gradient of the local CDW phase in NbSe<sub>3</sub> measured from muticontact transport measurements<sup>53, 54</sup> and x-ray measurements.<sup>24, 55</sup> In both experiments, the local CDW phase gradients varied with the positions and were largest near the contacts, supporting the additional tail like features observed in  $\Delta\tau/\tau$  near contacts. The additional features near contacts have been connected with the phase-slip processes responsible for the current conversion from normal to the CDW current and vice versa.

### 1.7.3 Comparison of $\Delta\tau/\tau$ for Unipolar and Bipolar Voltages

As discussed above, the electromodulated transmission signals in blue bronze have a bulk component arising from polarization of the CDW throughout the sample and a contact component mainly arising from the phase-slip processes near contacts. These two components of  $\Delta\tau/\tau$  can be measured separately by applying two different types of square wave pulses.<sup>32</sup> The bulk component is measured by applying bipolar pulses of magnitude  $V_T$  and the contact component is measured by applying unipolar pulses at voltages  $V > V_T$ .

Figure 1.9a illustrates the voltage dependences of  $\Delta\tau/\tau$  near a contact for unipolar and bipolar square wave voltages. Also included in this graph with open circle is the voltage dependence of the CDW current. For bipolar voltages, the onset of  $\Delta\tau/\tau$  is

at  $V_p$ . However the onset of  $\Delta\tau/\tau$  for unipolar voltages is  $V_T$ , which coincides with threshold for depinning the CDW at the contacts. The CDW response to unipolar and bipolar square wave voltages is clearly different. When bipolar voltages ( $\pm V > V_T$ ) are applied, both the bulk polarization and the contact component of strain reverse sign with changing voltages<sup>56</sup> and the CDW response contains both the bulk and the contact contributions as seen in Figure 1.9. With unipolar voltages, the applied voltage is either on or off, thus polarizing the CDW in one direction only. In this case, the contact component relaxes quickly while the bulk polarization relaxes very little in one period of square waves due to pinning in the bulk. Therefore, the unipolar square wave voltages with  $V > V_T$  modulates only the contact component.

The spatial dependences of  $\Delta\tau/\tau$  for bipolar and unipolar square wave voltages are shown in Figure 1.9b. Here again, for unipolar voltages  $\Delta\tau/\tau$  appears only in the region near contacts, implying that it contains only contact component of the strain. For bipolar voltage at  $V_T$ , the spatial distribution of  $\Delta\tau/\tau$  is linear, reflecting the only bulk polarization. No additional features near contact regions are observed. For bipolar voltages with  $V > V_T$ , there appears an additional feature near contacts which is already discussed in Section 1.7.1.

Due to the different voltage, spatial, and temporal dependences of the bulk and contact deformations, the electro-optic effect can be used as a tool to probe the dynamics of the sliding CDWs and search for intragap soliton states associated with current conversion processes. The use of the electro-optic effect to investigate voltage oscillations in the nonlinear region, phase-slip processes required for current conversion, and dynamical studies of the sliding CDWs is the main focus in this thesis. Detailed experimental procedures and results are presented in the later chapters.

#### 1.7.4 **Electro-optic Effect Due to Changes in Phonons**

The spectroscopic measurements on blue bronze have shown that the electro-optic

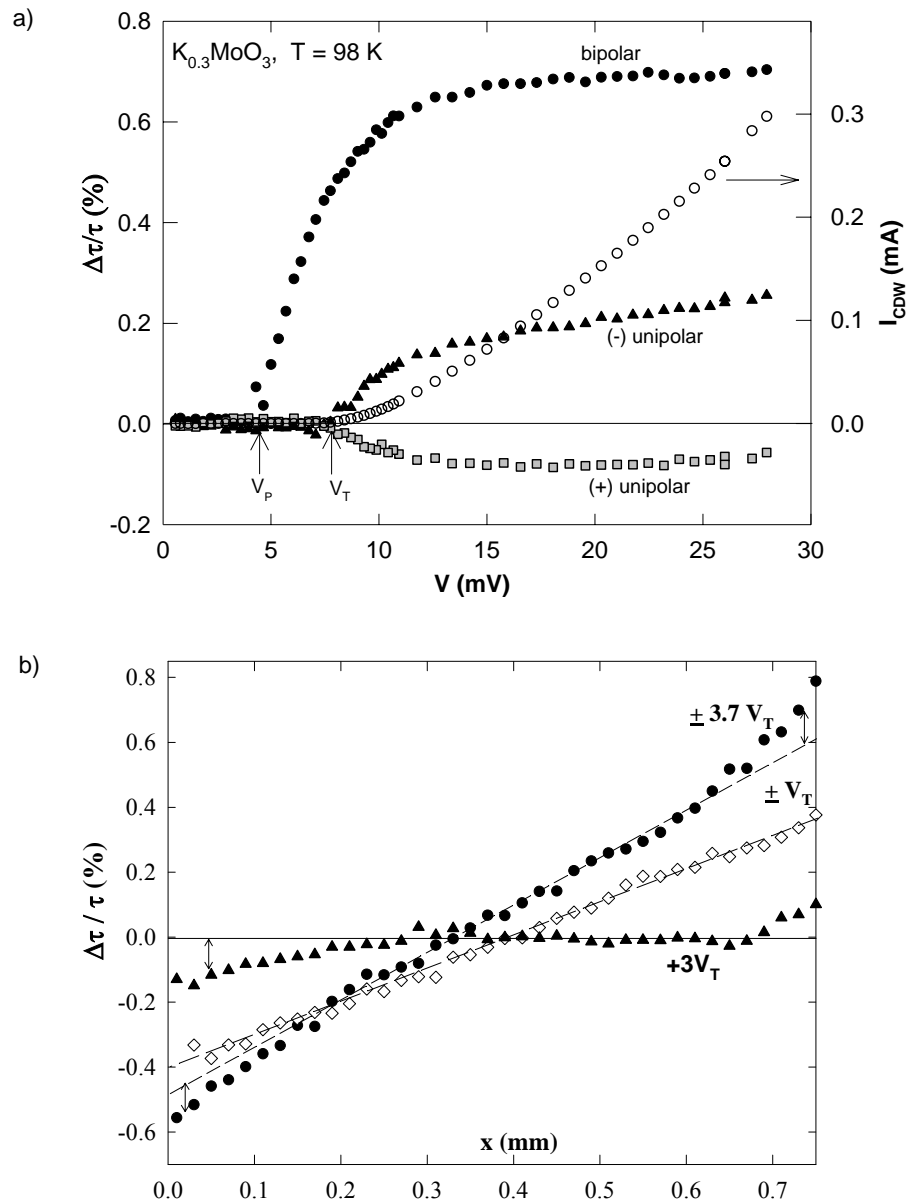


Figure 1.9 (a) Voltage dependence of  $\Delta\tau/\tau$  for bipolar, unipolar, and inverted unipolar square wave pulses, and the CDW current<sup>56</sup> (Note that the polarity of  $\Delta\tau/\tau$  is inverted for the unipolar voltages in this reference). (b) Spatial dependence of  $\Delta\tau/\tau$  for bipolar square waves at  $\pm 3.7 V_T$  and  $\pm V_T$ , and a unipolar square wave at  $+3V_T$ . The vertical arrows indicate representative contact contributions.<sup>57</sup>



effect was not only caused by changes in electronic intraband absorption but also caused by changes in phonon properties.<sup>56-58</sup> That is, phonons are apparently affected by the CDW deformation in the electric field and hence this interaction of the CDW with phonons causes the electro-optic effect. These unusual changes in the phonon spectra caused by the CDW polarization have been estimated by the electro-optic measurements of Emerling et al.<sup>57</sup> Figure 1.10 shows the  $\Delta\tau/\tau$  spectrum and the corresponding absorption spectrum (i.e. optical density  $-\ln(\tau/\tau_0)$ ), measured simultaneously on a single crystal blue bronze sample. The  $\Delta\tau/\tau$  spectrum showed three types of changes near phonon absorption lines.<sup>57, 59</sup> For most phonons,  $\Delta\tau/\tau$  had a derivative line shape, indicating that the major effect was a change in the phonon frequency. Linewidth changes appear as second-derivative line shapes for a few phonons. One phonon simply had a peak in  $\Delta\tau/\tau$ , indicating change in the oscillator strength of  $\sim 0.1\%$ , while the linewidths or frequencies of most phonons changed by  $\sim 0.01 \text{ cm}^{-1}$  when the CDW polarized.<sup>57</sup> These changes in phonons seem rather small but they have strikingly large effects on the electro-optic spectrum.

The changes in linewidths can be understood in terms of changes in phonon damping through quasiparticle scattering. For example if the quasiparticle density decreases at the positive contact, phonon damping by quasiparticle scattering also decreases, and the phonon line sharpens. In the case of phonons with frequency shifts, the phonons softened on the positive side of the sample and hardened on the negative. It was speculated that these shifts reflected mixing between the phonons and virtual electron-hole excitation across the CDW gap.<sup>59</sup> This mechanism gives the correct sign for the observed frequency shifts but experiments did not show that the frequency shifts were thermally activated, as expected. Instead, the temperature dependence of the shifts was weak. The physics underlying the change in oscillator changes is also unclear. It was suggested that the particular phonon which changed oscillator strength was a phase-phonon.<sup>32</sup> However, that would require a mixing of polarizations, since phase phonons are expected to occur for longitudinal modes, and would also require a change in amplitude of the CDW as well as its phase deformation.<sup>60</sup>

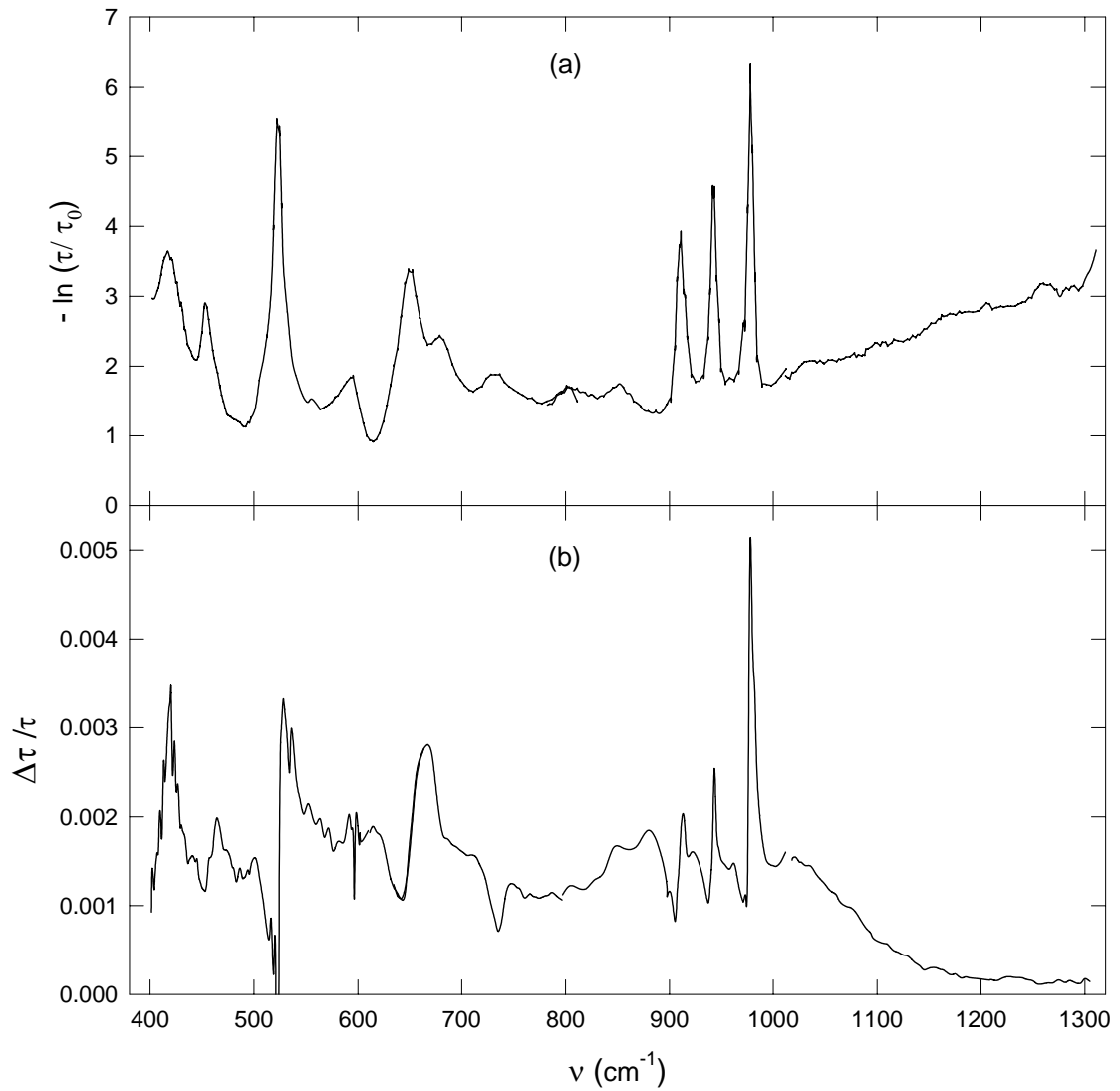


Figure 1.10<sup>59</sup> (a) The optical density, and (b) the electromodulated transmission spectra of blue bronze at 82 K. These spectra were taken with bipolar square wave voltages,  $V = \pm 1.7 V_p$ , (where  $V_p = 15$  mV for the sample).

# Chapter 2

## Experimental Procedures

In this chapter, the experimental procedures used in the electro-optic measurements are described. The infrared light source (tunable diode lasers), infrared microscope and sample preparation for measurements are also described.

### 2.1 Introduction

The electro-optic measurements on quasi-one-dimensional conductors began in 1994. Since then many improvements have been made in the electro-optical system. Early measurements were performed with a Perkin-Elmer 301 spectrophotometer with a broad-band (globar) source. A zinc doped germanium photoconductor which operates at liquid helium temperature was used as the signal detector. In these measurements, the intensity of the transmitted light using the globar source and grating was very small especially near phonon lines. The small size of the transmission signal produced an extremely small electromodulated transmission signal and measurements became very difficult and usually took a long time. Therefore, a light source with more intensity than the globar source was needed to continue and extend spectral electro-optic measurements on CDW materials. Therefore, four infrared tunable diode lasers (TDLs), along with a new spectrometer, were integrated into the system in 1997. These four diode lasers are cooled with a helium refrigerator and cover the spectral range from  $400\text{ cm}^{-1}$  to  $1200\text{ cm}^{-1}$ . (Whereas we previously had a laser which reached  $1300\text{ cm}^{-1}$ , as shown in Figure 1.10, when it failed, its replacement only reaches  $1200\text{ cm}^{-1}$ ) All the important results of previous electromodulated transmission experiments have been briefly reviewed in Section 1.7.

The results of electromodulated transmission experiments for perpendicular polarized light on blue bronze revealed that the experiments for parallel polarized light were needed to complement the previous results. However the electromodulated transmission experiments for parallel polarized light would require samples much thinner than practically obtainable by cleaving. This idea prompted the electro-reflectance measurements which were not readily done in the previous optical system. Also the results of previous work indicated that the sensitivity and spatial resolution of the system needed to be improved in order to study very thin samples, such as crystals of orth-TaS<sub>3</sub>. Therefore, the infrared microscope with a capability of doing both reflectance and transmission measurements (for both polarizations) was integrated into the laser system in 2002. Most of the results presented in this thesis have been taken using the infrared microscope.

## **2.2 Electro-optic System**

The electro-optic (reflectance) measurements were done using a Thermo-Nicolet infrared microscope with tunable diode lasers (TDLs) as light sources. For some of the measurements on blue bronze, the Perkin-Elmer 301 spectrophotometer with the global source was also used, using some spectral broad filters rather than a grating to increase the intensity. Our electro-optic system is unique in the sense that the infrared microscope, which is most often used with Fourier transform spectrometers, and TDLs, which are usually used to study narrow gas-phase molecular lines, were used together to study solid state spectra. The block diagram of the electro-optic system is shown in Figure 2.1. The unique electro-optic system consists of mainly four components. The first component is the tunable diode lasers and a closed-cycle (helium) refrigerator. Since these lasers operate only below 100 K, they need to be cooled down to bring them to the operating condition. Therefore, the lasers are cooled with a closed-cycle refrigerator continuously during the measurements. The second component (shown in Figure 2.2 below) is a specially designed spectrometer for TDLs. These lasers were first calibrated in the spectrometer before using them. The third component is the liquid nitrogen cryostat for sample cooling. The fourth component is the infrared microscope. The infrared

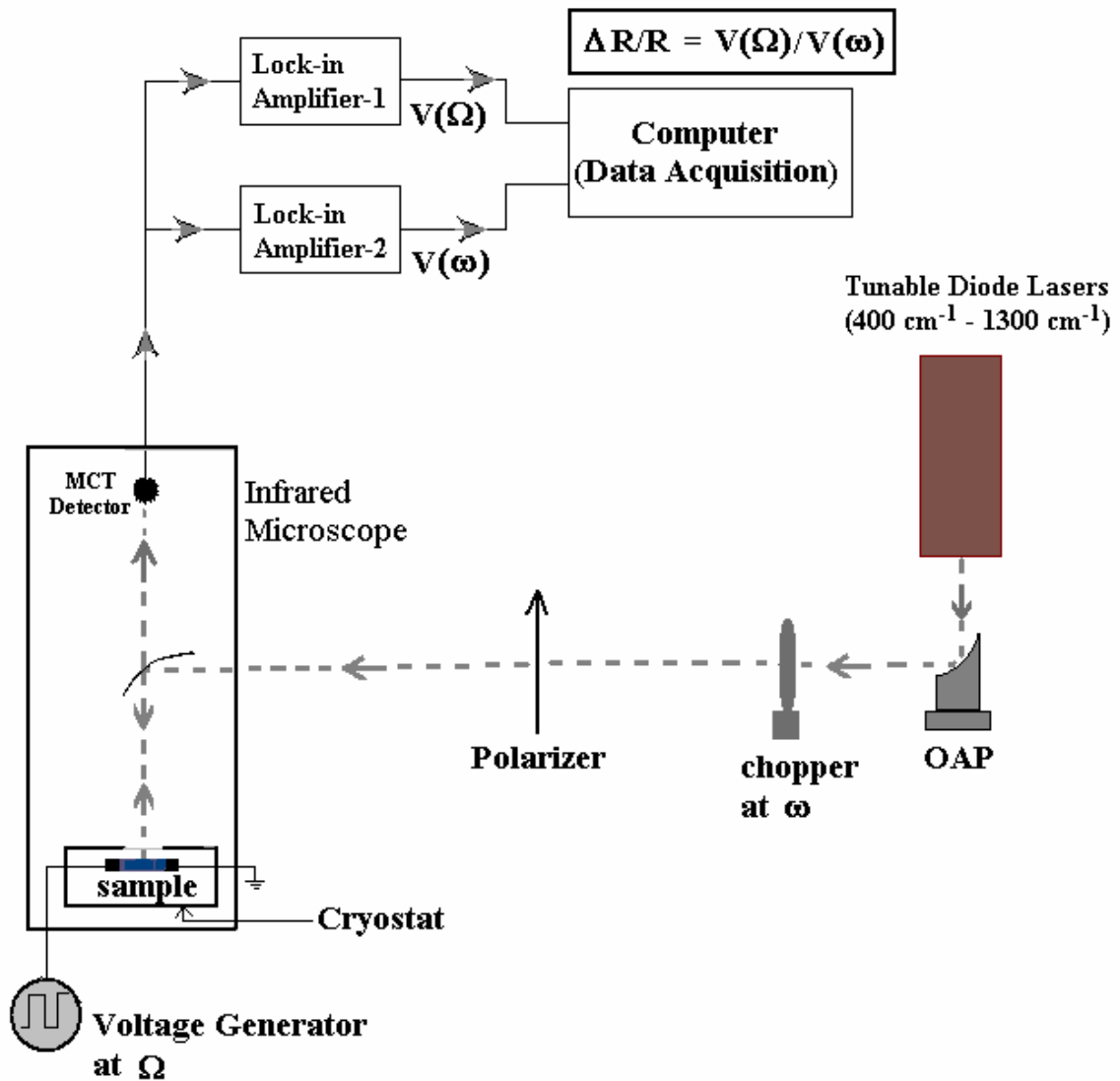


Figure 2.1 Block diagram of the electro-optical system. This schematic is drawn for electro-reflectance measurements. However, the electro-optical system can be used for both transmission and reflection measurements.

microscope has two photoconductive mercury-cadmium-telluride (MCT) detectors for signal measurements. The detector signal was measured simultaneously with two lock-in amplifiers and recorded in the computer through the interfacing. All the components are described in detail in the next section.

### 2.2.1 Tunable Diode Lasers

Infrared tunable diode lasers are lead-salt semiconductor diodes such as  $Pb_{1-x}Sn_xSe$  (lead-tin-selenide),  $Pb_{1-x}Sn_xTe$  (lead-tin-telluride), and  $PbS_{1-x}Se_x$  (lead-sulfide selenide) with variable compositions.<sup>61-64</sup> Our electro-optic system has  $Pb_{1-x}Sn_xSe$  diodes (L-series) from Laser Components, Inc.. The laser emission wavelength depends on the alloy composition value (x) and lies in the spectral range of from less than 3  $\mu\text{m}$  to over 30  $\mu\text{m}$ . Lasers are fabricated by forming a p-n junction in the crystal, then cutting into rectangular parallelepipeds typically 200  $\mu\text{m}$  x 300  $\mu\text{m}$  in cross-section (  $\sim$ 100  $\mu\text{m}$  in length); after polishing and attaching ohmic contacts the diode is mounted onto a gold-plated copper stud.<sup>64</sup> The emitting area of a TDL is typically <sup>65</sup>  $\sim$  50  $\mu\text{m}$  x 10  $\mu\text{m}$ .

The tunable diode laser is similar in many respects to the light emitting diode (LED). Both devices consist of a tiny p-n junction diode formed in a single crystalline semiconductor, and emit radiation when electrical current of the correct polarity (forward biased) is passed through the junction. For a TDL, the threshold current for emission is typically a few hundred millamperes (mA). The wavelength,  $\lambda$  of emitted radiation is determined by the semiconductor's energy gap through the expression <sup>62</sup>

$$\lambda = \frac{hc}{E_g} = \frac{1.24}{E_g} \text{ (\mu m)} \quad (2.1)$$

where h is Planck's constant, c the velocity of light and  $E_g$  is the bandgap energy in electron volts.

Laser emission is produced by multiple reflections and amplification between the parallel end faces of the diode which define the resonant cavity.<sup>64</sup> While the wavelength of the emission is determined by the bandgap, the precise modes are governed by the refractive index of the material and the cavity length, and is given by the equation<sup>62</sup>

$$\lambda_m = 2nl / m \quad (2.2)$$

where  $n$  is the refractive index,  $l$  the cavity length, and  $m$  is the number of half wavelengths within the cavity. The separation between two modes is given by

$$\Delta\lambda = \frac{\lambda^2}{2nl[l - \lambda/n(dn/d\lambda)]} \text{ cm} \quad (2.3)$$

The energy bandgap,  $E_g$ , and the refractive index,  $n$  are temperature dependent and they change differently with temperature. Therefore, the laser wavelengths can be tuned by varying laser temperature and the output wavelengths are governed by Equations 2.1 and 2.2. Usually tuning is accomplished by varying the heat sink temperature of the device. Since changing the forward biased current also changes the temperature of the p-n junction, the laser wavelengths can also be tuned by varying the current. By changing the temperature of a TDL, the wavelength can be varied up to 200  $\text{cm}^{-1}$ . However by varying the current, a tuning range is usually about 10  $\text{cm}^{-1}$ . Generally, the current is varied if fine tuning is required. In general the lasers emit in several spectral modes simultaneously when the current is significantly above threshold. Typically the spectral modes for tunable diode lasers are separated by 1 to 3  $\text{cm}^{-1}$  and mode selection is easily achieved with a grating. The linewidth<sup>62</sup> of a single mode is  $\sim 10^{-4} \text{ cm}^{-1}$ . Also the intensity of laser radiation is strong compared to the broad-band radiation. Because of narrow linewidths and high intensity of radiation, TDLs have been used extensively for high resolution spectroscopy<sup>62, 64</sup>.

All the TDLs operate at cryogenic temperatures, typically between 10 K and 100 K. The properties of TDLs are critically temperature dependent and generally require

temperature stability better than a small fraction of an K.<sup>62</sup> As discussed in Section 2.1, the electro-optic system has four tunable diode lasers with a typical power of 0.5 mW, operating in a multi-mode condition, covering the spectral range  $400\text{ cm}^{-1}$  to  $1200\text{ cm}^{-1}$ . These TDLs are mounted in a row (represented as 1-4 in Figure 2.2) on the cold finger of a coldhead (shown in Figure 2.2) of a closed-cycle refrigerator (CTI air-cooled 8200 compressor) for their operation. High pressure ( $\sim 250$  psig) helium gas is cycled through the compressor to operate the closed refrigerator system. To keep the refrigerator working in a good condition, the adsorber in the compressor, which removes impurities from the high purity helium gas, is changed every 12 months. As the working temperatures of TDLs are below 100 K, the coldhead needs to be kept in a good vacuum in order to maintain its temperature for a long period of time. To maintain a good vacuum, a Modion ion pump with a gauge (bar graph display) is attached to the coldhead and is operating all the time. The pressure of the pump was recorded every day. Any increase in pressure reading is an indication of a bad vacuum which causes the base temperature of the lasers to increase. As a regular maintenance, the coldhead was brought to above 100 K and pumped out to less than 10 microns pressure with a diffusion pump (with a liquid nitrogen trap) every month.

The TDLs are operated through a stabilized dc current source, the L5830 TDL controller (Laser Photonics). This controller is a microprocessor-controlled temperature and current controller designed for use with the TDL lasers. The current can be varied from 0 to 1000 mA. During the measurements, the TDL current was kept fixed at one appropriate value and lasers were tuned by changing the temperature. The temperature can be accurately maintained over the full range from room temperature (300 K) to 20 K with 10 mK resolution. With the L5830 controller, the TDLs can be used either in a modulated mode or in a continuous mode. For the electro-optic measurements, the modulated TDLs were used in continuous mode.

### **2.2.2 Optics Module**

The TDLs are used with a specially designed optics module as shown in Figure



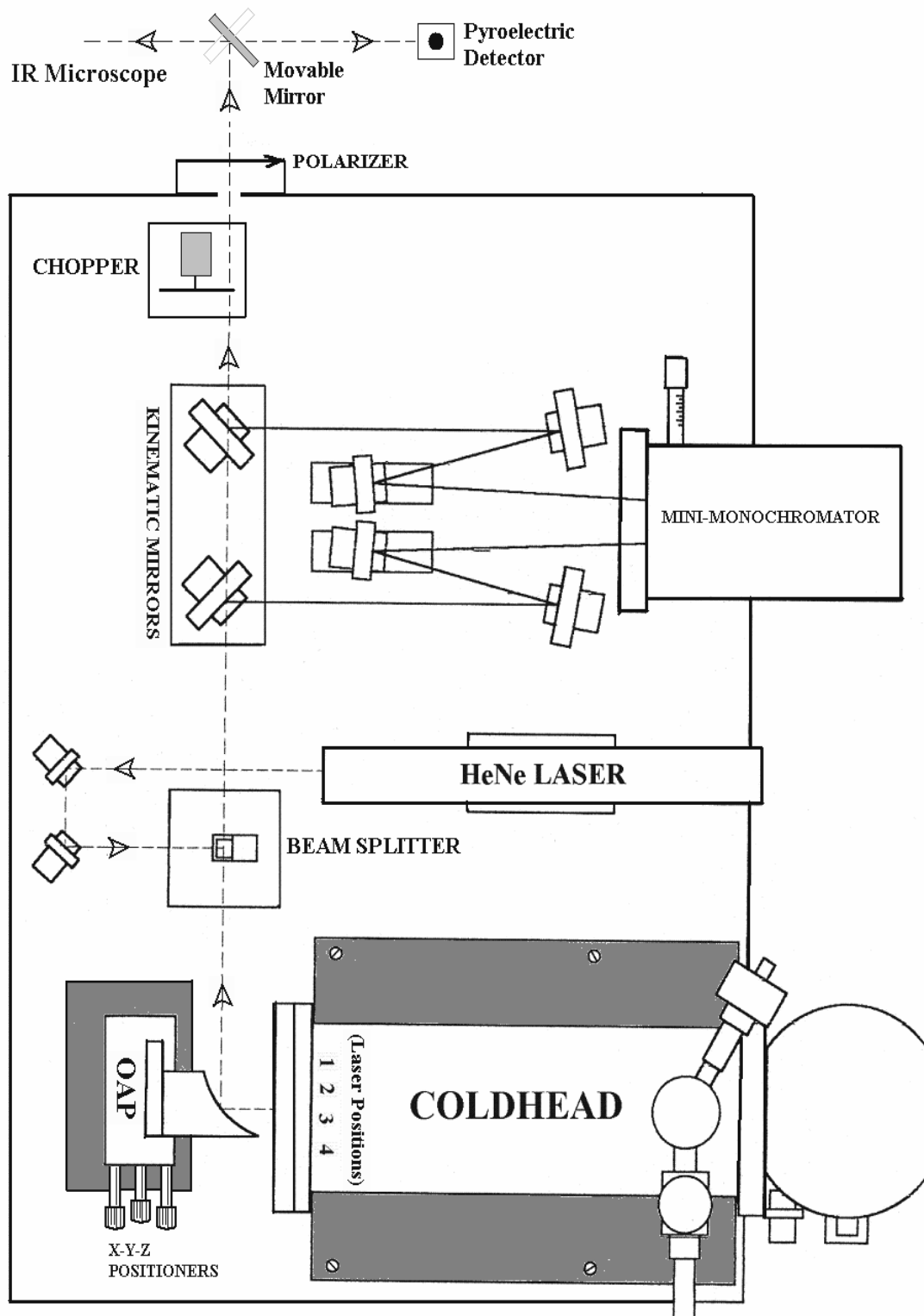


Figure 2.2 Optics module designed for tunable diode lasers (TDLs)

2.2. This optics module is designed to provide beam collimation and optical alignment capabilities for use with infrared diode laser sources. This module has a diamond-turned aluminum coated, 1.5 inch focal length, 90° off-axis-parabolic (OAP) mirror to collect and collimate the divergent TDL output. With this arrangement, the collimated beam diameter is typically within the range of 10 to 15 mm. The OAP is mounted on a micrometer controlled X-Y-Z positioner for fine adjustment. The positioner was utilized for adjustment of each laser position during the measurements.

The alignment HeNe laser, which is coupled to the optical axis by means of a kinematically mounted cube beamsplitter, provides visible light. The beamsplitter produces forward and backward beams to align both downstream optics and the OAP to the laser chip. The HeNe is also utilized as a wavelength standard for calibration of the grating (mini-monochromator). Two kinematic mirrors are used for redirecting laser signals towards the mini-monochromator and back to the original direction. This module also includes a rotary chopper (Model: Stanford Research System 540) for signal modulation. It was found that more than half of the laser photons were always polarized in one direction; however an external polarizer was used to accomplish ~ 99 % polarization in the desired direction. Finally the light coming out of the optics module was redirected by a movable mirror either towards the pyroelectric detector for laser calibration or towards the IR microscope for the electro-optic measurements. In addition to the mini-monochromator, this optics module has one removable monochromator which can be placed in the position of the movable mirror. The removable monochromator was also used occasionally for the laser calibration.

Normally the alignment procedure makes use of the HeNe beam for coarse alignment and the IR signal itself for fine alignment. The pyroelectric detector, which operates at room temperature and has a diameter of about 1 mm, was utilized for alignment and calibration of lasers. With the cube beamsplitter in place and the HeNe on, the light spot was brought as closely as possible onto the diode laser chip by adjusting the horizontal (Y) and vertical (Z) stages. The focus of the OAP (X) can not be accurately adjusted using the HeNe spot. Therefore, the X micrometer was initially set to the middle

of its adjustment range. In this pre-aligned position, it was possible to detect a signal from the HeNe laser, with the minimonochrometer operating at a high order, with the (ac coupled) pyroelectric detector. The alignment was made easier by observing the signal with an oscilloscope. Once the pre-alignment was completed, the beamsplitter and the kinematic mirrors were removed from their positions and an TDL laser was turned on. The OAP alignment was optimized by observing the pyroelectric signal. Optimizing the OAP focus for maximum signal, which may require some iteration, results in the properly collimated laser beam. The OAP alignment was optimized the same way for each laser and the X-Y-Z micrometer readings were recorded for each laser. To help better collimate the beam, a circular aperture with a typical size of  $\sim 0.5$  cm was placed just before the polarizer.

### **2.2.3 Cryostat**

Figure 2.3 is a schematic of the continuous flow liquid nitrogen cryostat (MicrostatN cryostat) designed to allow a sample to be cooled to a low temperature and studied with the infrared microscope. Since a continuous flow cryostat does not have an internal reservoir to store a supply of cryogen, the liquid nitrogen is supplied from a separate storage vessel through an insulated transfer tube. A gas flow (diaphragm) pump and a gas flow controller are used to control the flow of gas through the cryostat. A thermometer and a heater, which are mounted on the heat exchanger, were used with a temperature controller (model: Intelligent temperature controller - 601, Oxford Instruments) to achieve the desired temperature of the sample between 77 K and 500 K. The leads for the thermometer, heater, and sample were heat sunk onto the cold plate and passed through a hermetic feed-through to the outside.

The sample was mounted in vacuum on a sample holder attached to the heat exchanger and cooled by conduction. Two KRS-5 (thallium bromoiodide, which is transparent to the mid IR) windows were permanently bonded on the top and bottom O-ring sealed flanges of the cryostat for optical access. The KRS-5 window allowed the sample to be brought close to the objective lens of the microscope. The sample space was

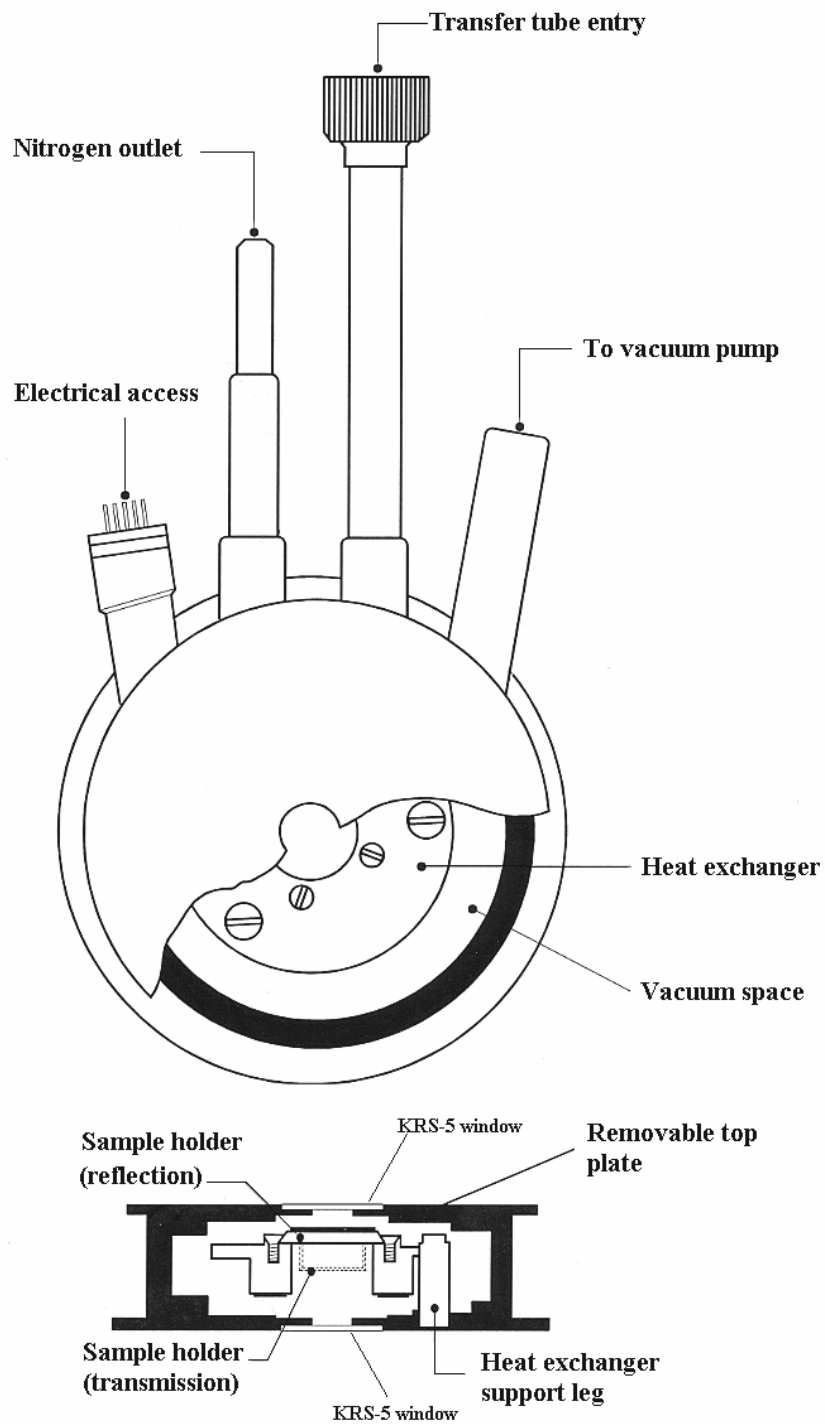


Figure 2.3 Schematic diagram of the MicrostatN cryostat for sample cooling (Reproduced from Operator's Handbook, Oxford Instruments, Inc.).

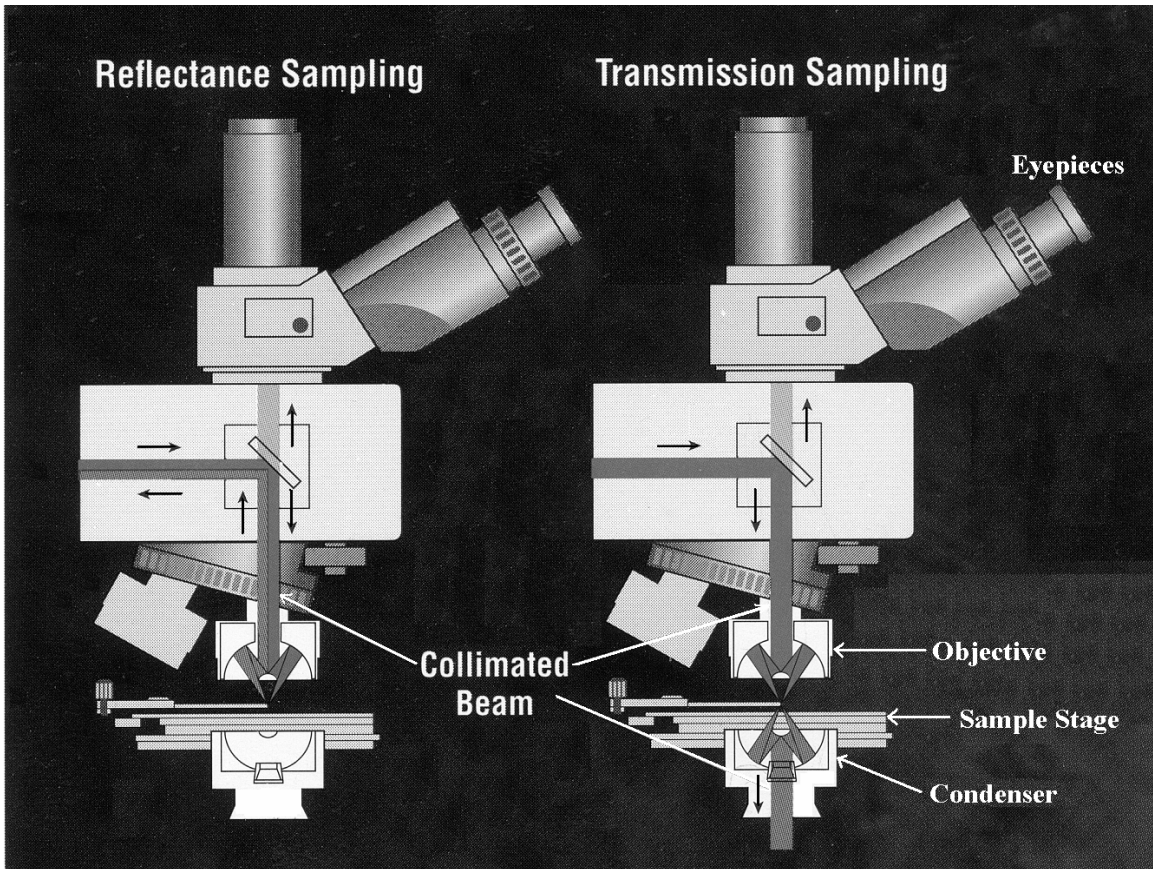
thermally isolated from the room temperature surroundings by the vacuum chamber which was pumped continuously with a rotary pump while the cryostat was running. The rotary pump was attached to a fore-line trap to prevent oil mist from the pump backstreaming into the vacuum chamber.

The cryostat was held tightly with two screw-knobs on the sample stage of the microscope. The cryostat was pumped very well (usually overnight) before the sample was cooled down to the desired temperature. Since thin samples of blue bronze samples are very brittle and fragile, a slow cooling rate of  $\sim 1.5$  K/min was always used during the sample cooling.

## 2.2.4 Infrared Microscope

The Thermo-Nicolet Continuum infrared microscope was used for the electro-optic measurements. Figure 2.4 shows a part of the continuum infrared microscope. The condenser, objective, and the sample stage of the microscope are shown here. The continuum IR microscope has an infinity corrected optical design. An infinity corrected optical design transmits light in the form of collimated rather than focused beams. The collimated beams increase the signal-to-noise because spherical aberrations are greatly minimized and provide the visual image quality with a flat field of view at the sample. The spatial resolution of the microscope is  $5 \mu\text{m}$ . One convenient feature of the microscope is that the sample can be seen even during the data collection.

The continuum IR microscope has two photoconductive mercury-cadmium-telluride (MCT) detectors with very high peak detectivity. Both detectors, which are mounted in separate steel dewars, operate at 77K, requiring the use of liquid nitrogen. The first detector covers the spectral range of  $450 \text{ cm}^{-1}$  to  $1300 \text{ cm}^{-1}$ , with the peak detectivity of  $6.6 \times 10^9 \text{ cm}\sqrt{\text{Hz}}/W$  at  $465 \text{ cm}^{-1}$ . The second detector covers the spectral range of  $600 \text{ cm}^{-1}$  to  $3000 \text{ cm}^{-1}$ , with the peak detectivity of  $4.4 \times 10^{10} \text{ cm}\sqrt{\text{Hz}}/W$  at  $740 \text{ cm}^{-1}$ . The first detector, which covers most of the spectral range of our TDLs from  $400 \text{ cm}^{-1}$  to  $1200 \text{ cm}^{-1}$ , was primarily used for electromodulated spectra measurements. The



Figures 2.4 Part of the infrared microscope. The collimated beams are shown for reflectance and transmission sampling modes.

second detector was also used occasionally. (Of the four TDLs, Laser #1, which covers the spectral range of  $400\text{ cm}^{-1}$  to  $600\text{ cm}^{-1}$ , was the weakest in intensity. The other three lasers # 2, 3, and 4 were more powerful, and therefore their signals would overload the lock-in amplifier. In order to use the second detector with these three lasers, the detector signal needs to be attenuated using a divider circuit. Moreover both detectors have similar experimental values of signal-to-noise ratio, although the second detector has higher intrinsic detectivity value than the first since most of our noise come from the vibration of the lasers due to the mechanical vibration of the cold head.)

The sample cryostat was placed on the sample stage of the IR microscope. For reflection measurement, the reflection viewing mode was selected by pressing the mode selection switch on the front panel. The size, shape, and orientation of the aperture image were adjusted by using the reflex aperture controls. The sample image was focused by using the stage focus knob (an electrical motor-driven knob with fine adjustment). With a detector cooled with liquid nitrogen and a laser on, the laser signal was optimized by using the stage focus knob. Once the signal was optimized, the sample stage was left undisturbed to begin the measurements.

### **2.3 Laser Calibration**

The TDLs were calibrated before using them. As discussed in Section 2.2.1, lasers were tuned for a fixed forward biased current by varying their temperature. For the calibration of each laser, the biased current was chosen somewhere between the threshold current for lasing and the maximum operating current. Four TDLs named 1 through 4 were calibrated at forward biased currents of 400 mA, 500mA, 700 mA, and 800 mA respectively. The minimonochromator and pyroelectric detector were used for the calibration of each laser. The laser signal was modulated with a rotary chopper for lock-in measurements. For convenience, an oscilloscope was used for observing the IR signal.

During the calibration process, the laser current was fixed and the temperature of the laser was increased from 20 K to the maximum operating temperature in steps of 2 K.

Since each laser diode emits several modes, the intensity and the wavenumber (i.e. drum reading of minimonochromator) corresponding to each lasing mode were recorded at each temperature. All the weighted average of the modes was found for each calibration temperature. Typical calibration curves for the TDLs are shown in Figure 2.5. The bandwidth of the multi-mode, which was a function of temperature, was typically  $10 \text{ cm}^{-1}$  as represented by an error bar in the calibration curve. It was found that the number of modes decreased at higher temperatures; therefore the bandwidth also decreased.

Each calibration curve is linear at higher temperatures but it is not linear at lower temperatures as seen in Figure 2.5. Therefore, a polynomial (i.e. either quadratic or cubic) fitting with the temperature as a variable was done for each curve separately. The fitting parameters were the calibration parameters for each laser. It is well known that these TDLs change their lasing properties with time and temperature cycling. Therefore, the laser calibration was checked for a few temperatures every 2 weeks. If the calibration was changed by more than  $1 \text{ cm}^{-1}$  then the laser was recalibrated.

## **2.4 Sample Preparation**

Blue bronze and  $\text{TaS}_3$  crystals were provided by Professor R. Thorne's group of Cornell University. For the electro-optic measurements, single crystal samples with small threshold fields are necessary. Samples with higher threshold fields would require higher voltages to be applied, causing heating problems. Since blue bronze crystals and ortho- $\text{TaS}_3$  crystals have different physical shapes and properties, they have to be handled differently when preparing for experiments.

To find a good batch of crystals, the threshold fields of blue bronze crystals were measured at liquid nitrogen temperature. These characterizations were quickly done on thicker samples. Once the crystals with lower threshold were found, the further preparation of the sample was performed.

Electromodulated transmission experiments require very thin ( $< 5 \mu\text{m}$ ) samples



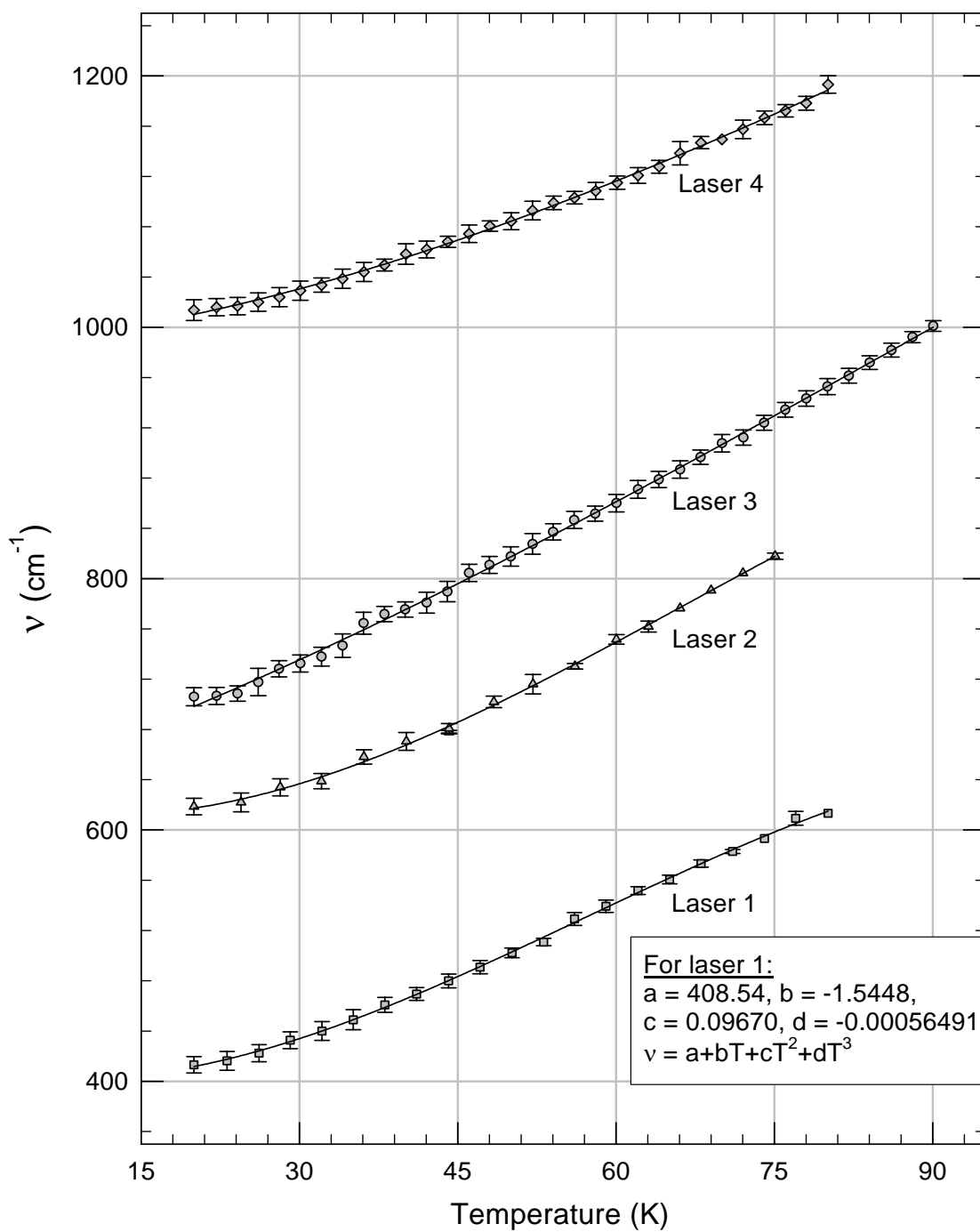
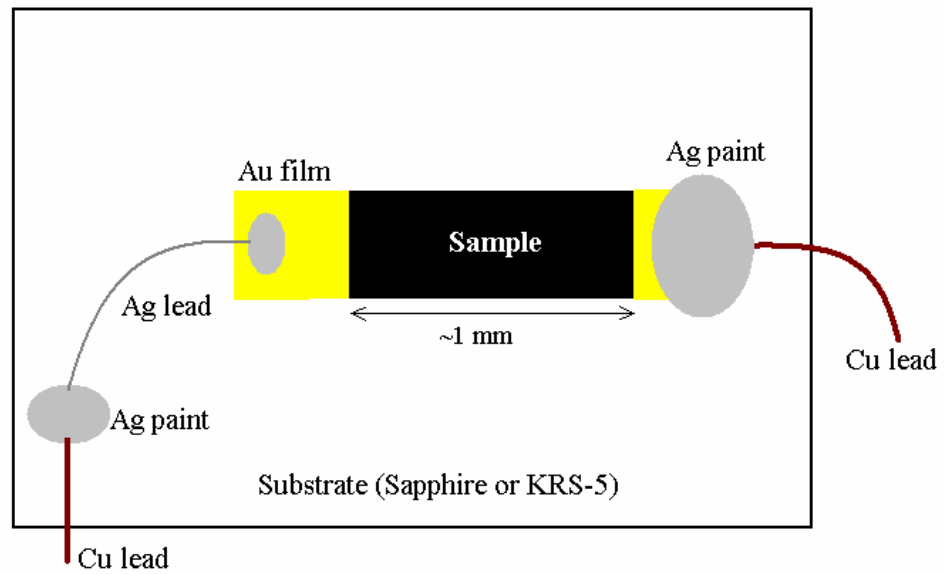


Figure 2.5 Typical calibration curves for four tunable diode lasers (TDLs) operating at different currents; laser 1 at 400 mA, laser 2 at 500 mA, laser 3 at 700 mA, and laser 4 at 800 mA. The solid lines are polynomial fits to the data. The cubic fitting parameters for laser 1 are shown in the box.

while electro-reflectance experiments require samples with a smooth surface. Making samples thin was really a difficult task since thin samples are very fragile and tend to break easily. For electromodulated transmission measurements, samples were  $\sim 7 \mu\text{m}$  thick. However samples were  $\sim 15 \mu\text{m}$  thick for electromodulated reflectance measurements. The single crystals of blue bronze were made thinner by cleaving along the plane parallel to the monoclinic  $b$  axis and  $[102]$  crystallographic directions. For the cleaving process, a large crystal was first glued down to a glass slide using fingernail polish and sticky tape was used to cleave the crystal until the desired thickness was reached. After cleaving, the crystal was typically  $\sim 1.5 \text{ mm}$  long in the chain direction and  $0.5 \text{ mm}$  wide. The crystal sample was removed from the glass slide by dissolving the nail polish in acetone. To clean the surfaces, the sample was etched in dilute  $\text{NH}_4\text{OH}$  (3:1, distilled water to commercial  $\text{NH}_4\text{OH}$  (29%)). Gold films were evaporated on the ends of the sample for current contacts, and the sample was mounted with silver paint on a substrate for current and thermal contacts. As a thin sample is extremely fragile, only one end of the sample was attached directly to the substrate with the silver paint. The other end of the sample was attached with a thin silver wire (i.e. flexible wire), which would help prevent the sample from breaking during the thermal cycling due to differences in the thermal contraction of the sample and substrate. The other end of the silver wire was painted onto the substrate. Finally, the substrate was glued to the cold finger of a MicrostatN cryostat (discussed in Section 2.2.3) with the silver paint or varnish. The sample was configured for two-probe measurements. A mounted blue bronze sample for the electro-optic measurements is shown in Figure 2.6a.

Two different types of substrates were used for mounting the blue bronze sample. The sample was mounted with silver paint on the KRS-5 substrate for electromodulated transmission measurements and on the sapphire substrate for electromodulated reflectance measurements. Sapphire substrate was used for reflectance since it has better thermal conductivity than KRS-5 and also it has better match of the thermal expansivity with blue bronze. KRS-5 substrates were needed for transmission as they are transparent to the mid-IR, however they have the disadvantage that their thermal expansivity differs considerably from that of blue bronze, increasing the probability of the sample breaking

a)



b)

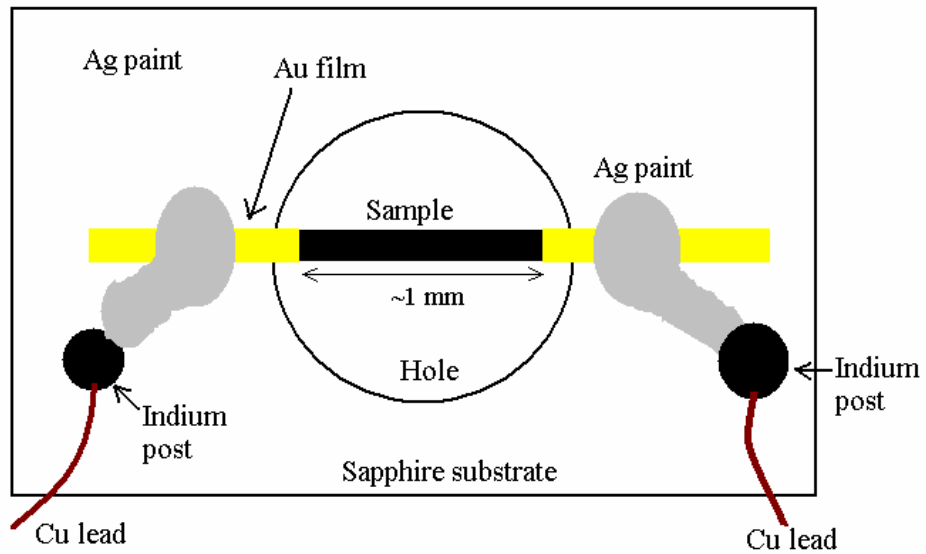


Figure 2.6 (a) Blue bronze sample mounted on a sapphire substrate for reflectance and a KRS-5 substrate for transmission. (b) Ortho-TaS<sub>3</sub> sample mounted on a sapphire substrate.

when changing temperature.<sup>57</sup>

The orthorhombic TaS<sub>3</sub> crystals grow as whiskers. The wider (> 20 μm) and smoother crystals were first selected from the crystal container. Thicker crystals were cleaved by using two tiny wooden brushes. Cleaving was not necessary for some crystals as they were found in the desired dimensions. Samples were first rinsed in ethanol with a final rinse in acetone. Typical crystal dimensions were 2 mm x 25 μm x 5 μm. Gold films were evaporated on the ends of the sample for electrical and thermal contacts.

A sapphire substrate (with thermal expansion coefficient  $\sim 7.5 \times 10^{-6}$  /K)<sup>66</sup> was used for mounting TaS<sub>3</sub> samples since it has a good match of the thermal expansion coefficient with TaS<sub>3</sub> ( $\sim 8 \times 10^{-6}$  /K)<sup>67</sup>. When samples were mounted on KRS-5 (with thermal expansion coefficient  $\sim 6 \times 10^{-5}$  /K)<sup>68</sup>, they bowed and twisted substantially when cooled since the KRS-5 contracts much more than TaS<sub>3</sub>. A hole with a diameter of 1 mm was drilled in the sapphire substrate. Since TaS<sub>3</sub> crystals were much stronger than blue bronze, both ends of TaS<sub>3</sub> crystals were mounted with silver paint on the top of the hole in sapphire substrate for current and thermal contacts. Some earlier samples were mounted on the substrate without any hole. The idea of putting the sample on the top of a hole was to avoid mixing of the reflected light from the sample surface with any reflected light from the substrate surface. With nothing near the sample edges, light apertures bigger than the sample width could be used, so that the entire cross-section could be measured, decreasing effects of diffraction. Two indium posts were used to connect the sample with the external leads. The sapphire substrate was glued to the cold finger of a MicrostatN cryostat with silver paint or varnish. Figure 2.6b shows the mounted TaS<sub>3</sub> sample for the electro-reflectance measurements.

## 2.5 Experimental Set-up for Electro-Optic Measurements

The experimental set up for electromodulated reflectance measurements using the IR microscope and electromodulated transmission measurements are discussed in this section. Search for narrow-band-noise (NBN) modulations of the infrared transmission in

blue bronze was done before the IR microscope was integrated into the electro-optic system. Only a brief experimental procedure for the infrared transmission is discussed in Section 2.5.1 below. The main focus of this thesis is on experiments to search for intragap states associated with the current conversion processes and dynamical studies of the sliding CDW state. For both experiments, electro-reflectance measurements have been performed. Although the experiments for the spectra of blue bronze and dynamical studies of ortho-TaS<sub>3</sub> are different, the general procedure for electro-reflectance measurements is discussed in Section 2.5.2 below.

### **2.5.1 Electro-Transmission Measurements**

As discussed above, the search for the narrow-band-noise (NBN) modulations of the infrared transmission in blue bronze was done using the previous electro-optic system (i.e. without an IR microscope). The detailed experimental procedures for the previous configuration of the system can be found elsewhere.<sup>32</sup> The block diagram for the NBN modulation measurements is shown in Figure 2.7.

For these measurements, samples, typically 1 mm long, were placed over narrow windows (0.1 – 0.3 mm long) in opaque films on IR transparent substrates (i.e. KRS-5 substrates). A Janis supertran continuous flow cryostat was used for sample cooling. Tunable IR diode lasers were used as light sources for most of the measurements, but some measurements were also made with the globar light source, as mentioned below. The dc voltages were applied to the sample, and modulation in the transmission intensity and electrical NBN in the sample were measured with a digital oscilloscope (Tektronix model: TDS 724 D) and fast-Fourier transformed with a typical effective frequency resolution of 1.5 kHz. The NBN in the electrical signal and the transmission signal (with its anticipated NBN modulation) were measured one at a time for several dc voltages. The electrical NBN was measured by directly connecting the sample ends with a BNC cable to the digital oscilloscope. Measurements were made on three samples at  $T \approx 78$  K with light polarized transverse to the conducting chains.

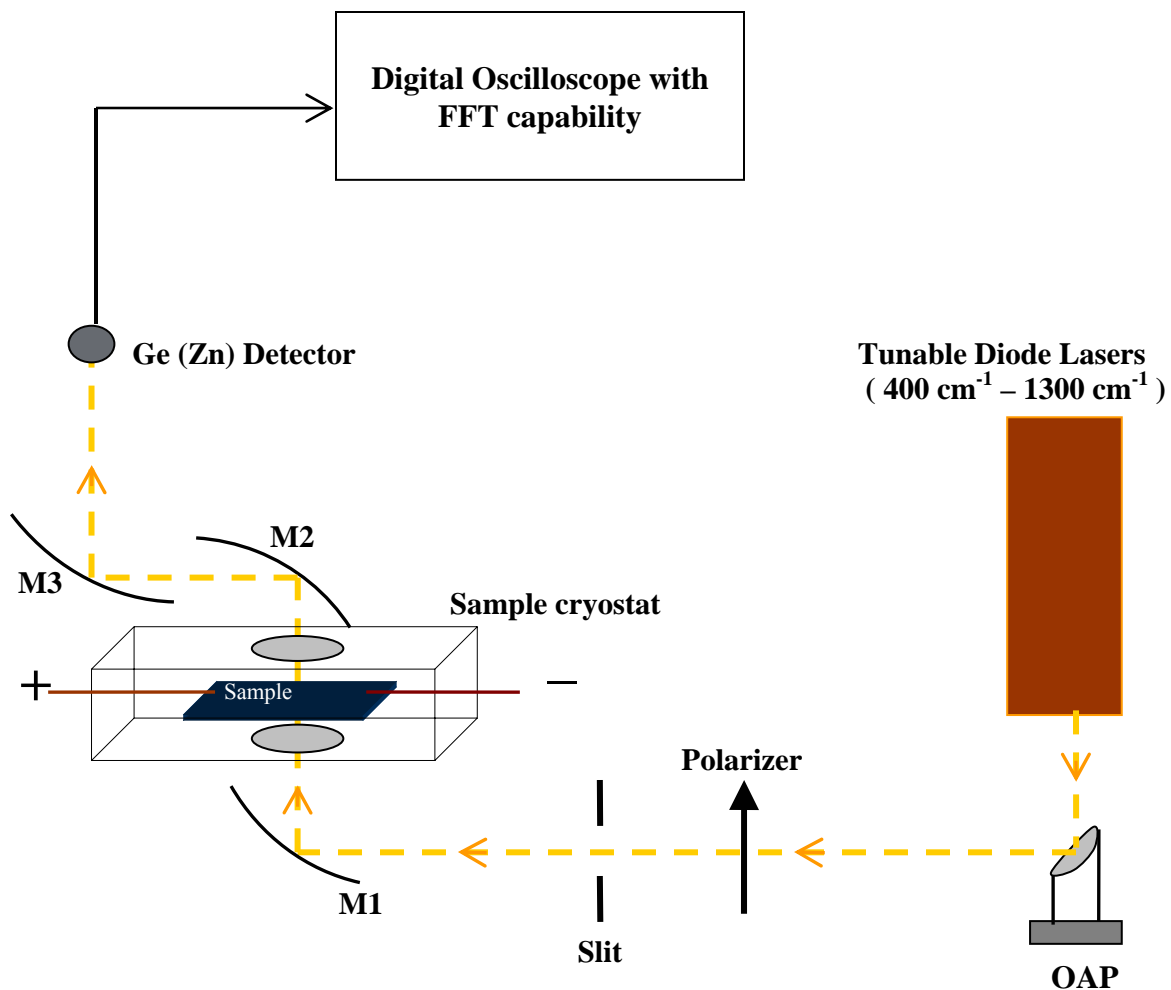


Figure 2.7 Block diagram for the electro-transmission measurements with a digital oscilloscope. M1, M2, and M3 are  $90^{\circ}$  off-axis-ellipsoidal mirrors, Ge(Zn) is a zinc doped germanium photoconductor detector, and OAP is a  $90^{\circ}$  off-axis-parabolic mirror.

For two samples, a Ge(Zn) photoconductor was used as detector and measurements were made at several photon energies between  $600 \text{ cm}^{-1}$  and  $1000 \text{ cm}^{-1}$ . The intrinsically large sensitivity ( $\sim 1.6 \times 10^{10} \text{ cm}\sqrt{\text{Hz}}/W$ ) of this high impedance ( $\sim 3 \text{ M}\Omega$ ) detector was compromised somewhat to obtain the required large bandwidth ( $\sim 150 \text{ kHz}$ ). The bandwidth of the preamplifier was increased by reducing a load resistance from  $3 \text{ M}\Omega$  to  $300 \text{ k}\Omega$ . Moreover, the load resistance was placed inside the liquid helium detector dewar in order to reduce the thermal noise. A low impedance ( $\sim 69 \text{ }\Omega$ ) mercury-cadmium-telluride (MCT) photoconductive detector was used for Sample #3 with somewhat improved sensitivity ( $\sim 1.2 \times 10^{10} \text{ cm}\sqrt{\text{Hz}}/W$ ). Measurements were made at photon energies  $> 770 \text{ cm}^{-1}$  for this sample. Unfortunately, the sample broke before measurements for photon energies  $< 770 \text{ cm}^{-1}$  were completed.

## 2.5.2 Electro-Reflectance Measurements

The block diagram of the experimental set-up for the electro-reflectance is shown in Figure 2.1. The IR microscope can be used for both reflectance and transmission measurements. The internal optics of the IR microscope is automatically adjusted for either reflectance or transmission by pressing the mode selection switch. The IR microscope and the optics module are continuously purged with dry nitrogen to remove moisture from the system. The size of the illuminated light spot can easily be varied in the IR microscope. The typical size of the light spot used for the electro-reflectance spectra of blue bronze was  $50 \text{ }\mu\text{m} \times 50 \text{ }\mu\text{m}$ . However, the smaller size ( $25 \text{ }\mu\text{m} \times 50 \text{ }\mu\text{m}$ ) of light spot was used for dynamical studies of the electro-optic response of ortho-TaS<sub>3</sub>.

After the sample was mounted in the cryostat and the cryostat chamber evacuated, the system was cooled and stabilized at a desired temperature. Then we characterized the non-ohmic response of the sample in order to determine the value of the threshold voltage. This was done by measuring the dc current versus voltage and plotting the voltage versus resistance. The sample was then aligned in the IR microscope to maximize the reflected signal. As the sample can be seen under the microscope, the alignment

process was easy and quick. The spatial controls of the sample stage that came with the microscope had a resolution of 100  $\mu\text{m}$ . Therefore, two micrometer heads were added to the sample stage so that the position could be set with 10  $\mu\text{m}$  resolution. To maximize the signal, the sample stage was moved up and down with an electrical motor-driven fine adjustment knob.

Square-wave voltages were applied to the sample, and changes in the reflected intensity in phase with the applied voltage were measured with a lock-in amplifier operating at the square wave frequency ( $\Omega$ ), which was usually kept high enough (253 Hz) so that signals due to modulations of the sample's temperature were negligible. Simultaneously, the intensity of the reflected light, chopped at a different frequency ( $\omega$ ), was measured with a second lock-in amplifier operating at the chopping frequency. Although neither the reflectance ( $R$ ) nor its change with voltage ( $\Delta R$ ) was measured precisely by itself, the ratio of the two lock-in signals provides a precise measurement of the relative change,  $\Delta R/R$ . Therefore, the relative change in reflectance is given by the ratio of the lock-in signals,  $S$ :<sup>58</sup>

$$S(\Omega)/S(\omega) = \Delta R/R \equiv [R(+V) - R(-V)]/R_{ave} \quad (2.4)$$

where  $R_{ave}$  is the average reflectance. The gold current contacts on the samples provided references for absolute reflectivity spectra, but these measurements were rough because of imperfect films and surfaces, possible diffraction effects, and lack of reproducibility of the lasers. The vibration of the lasers in the helium refrigerator typically limited the sensitivity in  $\Delta R/R$  to  $\sim \pm 5 \times 10^{-6}$ .

Two lock-in amplifiers were interfaced with a computer through a GPIB (general purpose interface bus) board, i.e. IEEE-488 interface bus. The previous electro-optic system was interfaced with an APPLE II+ computer through a home-made serial bus. The GPIB bus can communicate simultaneously with multiple devices and can transfer data at much faster rate than the serial bus. QuickBasic was used as a programming language.



Several QuickBasic programs were written for different kinds of measurements e.g. voltage and spatial dependences of electro-reflectance, frequency dependence of electro-reflectance, electro-reflectance spectrum etc. Although it would have been possible to also automate control of the laser controller (i.e. wavelength), this was not done so that the operator could maintain complete control of the experiment, desirable for measuring the very small and noisy signals. Data acquisitions were done by a computer and data were analyzed in Sigma plot 8.0 and Origin 6.0.

# Chapter 3

## Results and Discussions

In this chapter, the experimental results of the narrow-band-noise modulations of the infrared transmission of blue bronze <sup>69</sup>, electro-reflectance spectra of blue bronze <sup>58</sup>, and dynamics of the electro-optic response of ortho-TaS<sub>3</sub> <sup>70</sup> will be presented.

### 3.1 Search for Narrow-Band-Noise Modulations of the Infrared Transmission of Blue Bronze

One of the salient features of a sliding CDW is the presence of “narrow-band-noise” (NBN), oscillation of the voltage across the sample at a frequency proportional to the CDW current.<sup>6</sup> Although NBN is generally accepted as due to the CDW current, there has been a long-standing question about its origin. It has been suggested that NBN is generated in the sample bulk by modulations of the CDW current caused by defects <sup>71</sup>, <sup>72</sup>, but it has also been associated with dislocation motion (i.e. phase-slip) at contacts.<sup>22, 23</sup> Transport experiments designed to distinguish between these two cases had mixed results <sup>73, 74</sup>; of course, such experiments could only measure NBN at the contacts.

Figure 3.1 shows the voltage oscillations in time and frequency domains for an ortho-TaS<sub>3</sub> sample at 78 K for  $I = 3.5 \mu\text{A}$  and  $I = 3.2 \mu\text{A}$ . For this two probe measurement, the dc current was applied to the sample and voltage oscillations were measured in time with a digital oscilloscope, with fast Fourier transform (FFT) software. In the Fourier spectrum, one fundamental and ten harmonics are observed. The NBN is observed only above the threshold voltage for depinning the CDW state. The overall features of NBN depend on crystal quality and on the coherence associated with the current carried by the collective mode.<sup>9</sup>

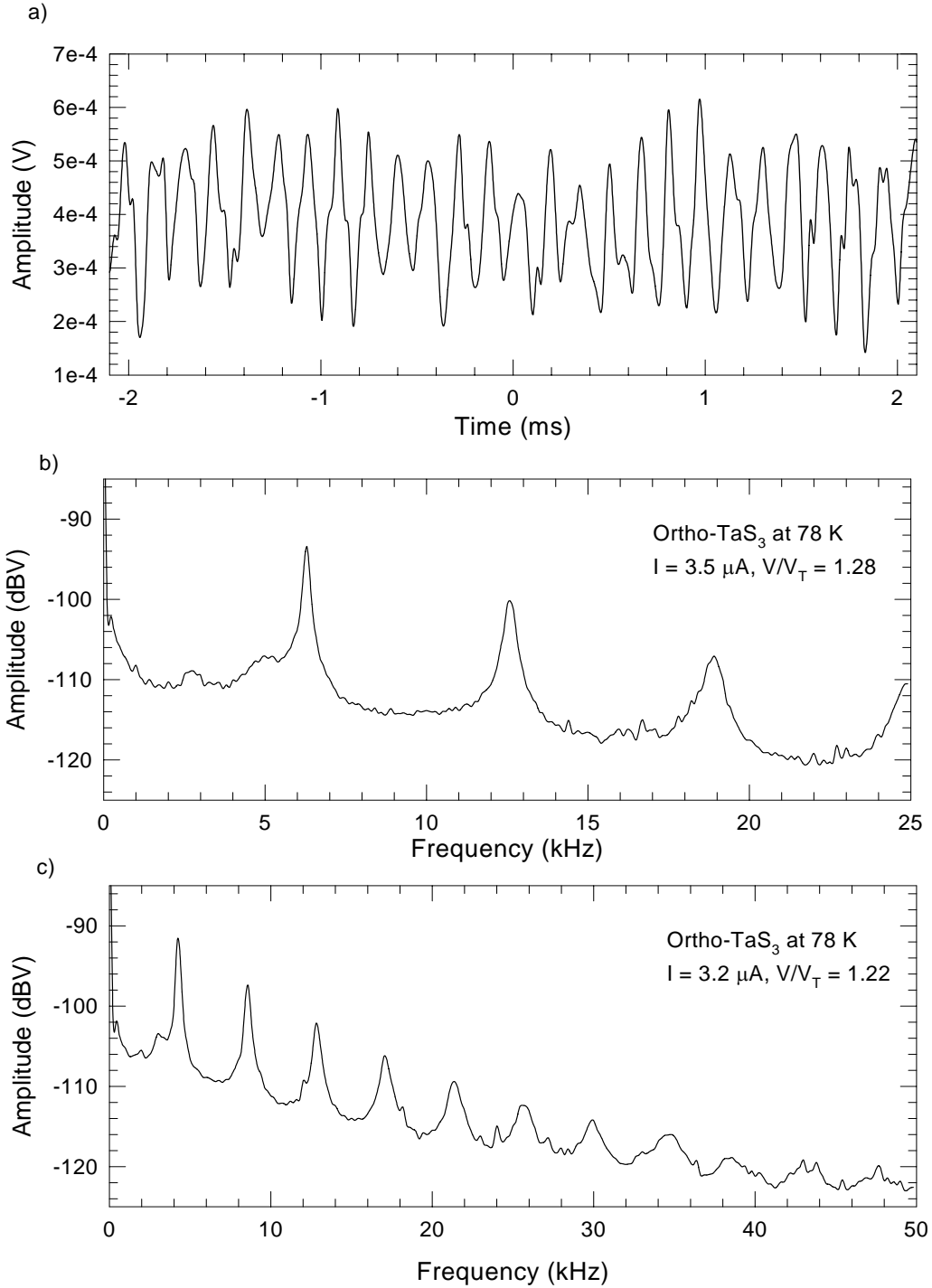


Figure 3.1 Voltage oscillations for an ortho-TaS<sub>3</sub> sample (dimensions: 1.5 mm x 20  $\mu$ m x 5  $\mu$ m,  $R = 13.5$  k $\Omega$ , and  $I_T = 2.3$   $\mu$ A) at 78K. (a) Voltage oscillations for  $I = 3.5$   $\mu$ A directly observed on an oscilloscope, (b) Fourier transformed of Fig (a), and (c) Fourier transformed of voltage oscillations for  $I = 3.2$   $\mu$ A.

As discussed in Section 1.7, for energies less than the CDW gap, the infrared transmittance,  $\tau$ , of the CDW conductor blue bronze ( $\text{K}_{0.3}\text{MoO}_3$ ) changes when the CDW becomes depinned, with  $\tau$  increasing (typically by a few tenths of a percent) near the positive current contact and decreasing near the negative.<sup>8</sup> (Corresponding changes in the absorption coefficient are given by  $\Delta\alpha \sim -(1/d)\Delta\tau/\tau \sim 3/cm$ , where  $d \sim 10 \mu\text{m}$  is the sample thickness.). Most of the changes were related to changes in the density of thermally excited quasiparticles (mostly electrons in blue bronze) screening deformations of the CDW in the applied electric field.<sup>25</sup> These results suggested that the IR transmittance might also be modulated at the narrow-band-noise (NBN) frequency, and that a comparison of the magnitude of such modulation at different locations in the sample might be used to distinguish between bulk and contact generated noise.

If the NBN current (at frequency  $f$ ) is not homogeneous in the sample, the condensate density will also locally oscillate at the NBN frequency. These changes will be screened by the quasiparticles:

$$\Delta\rho_{NBN}^{qp} = -\Delta\rho_{NBN}^{CDW} = I_{NBN} / (f w d \zeta) \quad (3.1)$$

where  $w$  is the width of the crystal and  $\zeta$  is the “NBN coherence” length, i.e. the longitudinal velocity coherence length ( $\xi_{||}$ ) if the NBN voltage is generated in the sample bulk and the phase-slip length ( $\Lambda$ ) if at the contacts, suggesting that the IR transmission may also be modulated at the NBN frequency, allowing a contactless, position dependent measurement of the NBN.

In addition to modulations of quasiparticle density, there are two other possible mechanisms which can lead to NBN modulations of the IR transmission: a) we have found that phonon frequencies, line widths, and oscillator strengths were affected by CDW deformations<sup>57</sup> (see Figure 1.10), opening the possibility that they may also oscillate at the NBN frequency, b) It has been suggested that the energies of the soliton states required for current conversion oscillate through the gap at the NBN frequency.<sup>27</sup>

Figure 3.2a shows sample-voltage NBN spectra for Sample #2; two fundamental frequencies are observed above  $I = 140 \mu\text{A}$ . The second and third harmonics (not shown for all currents) of the sharper (i.e. upper) fundamental were also observed. Both fundamental frequencies were observed to increase with the CDW current as shown in the inset of Figure 3.2a. Multi fundamental peaks are not uncommon,<sup>75</sup> and indicate that the CDW current differs in different portions of the sample. The other two samples we investigated, however, had only one fundamental frequency indicating more uniform current flow. Fourier spectra of voltage oscillations for different dc currents are shown for Sample #3 in Figure 3.2b. The linear relationship between  $f$  and  $I_{CDW}$  can be explained with the simple assumption that  $f$  is proportional to the CDW drift velocity  $v_{CDW}$ , i.e.  $f = v_{CDW} / \lambda$ , where  $\lambda$  is a characteristic length. Since the drift velocity is given by;  $v_{CDW} = I_{CDW} / neA$ ,  $f = I_{CDW} / ne\lambda A$ , where  $n$  is the density of the CDW condensate,  $e$  is the electron charge, and  $A$  is the cross-sectional area of the sample. A phenomenological model<sup>71</sup> for the dynamics of a sliding CDW in a periodic potential leads to the above relation. For Sample #2, with two fundamentals, only the lower varies linearly with the average CDW current (i.e. the excess current:  $I - V/R_0$ ), while the current becomes more uniform (i.e. the two frequencies approach each other) at high voltages.

Figure 3.3 and 3.4 show the Fourier transformed spectra of the transmittance (normalized to its dc value) at several laser frequencies  $\nu$  and the sample voltage ( $\Delta V_{NBN}$ , measured with the same oscilloscope/FFT settings) for Sample #2 and Sample #3 at a dc voltage of  $V = 1.5V_T$ , where  $V_T$  is the depinning threshold.<sup>6</sup> For sample #2, a NBN peak is observed at 29 kHz; the second and third harmonics (not shown) of this peak are also observable. The lower, broad fundamental is also observable above 10 kHz (also see Figure 3.2a). As shown in the Figure, there are no NBN features in the transmittance. For Sample #2 at  $615 \text{ cm}^{-1}$ , where the product laser power x transmission is maximal;  $\Delta\tau_{NBN} / \tau < 0.03 \%$  and  $\Delta\alpha < 0.3 / \text{cm}$ . (At this wavelength and voltage, the (dc) change in transmission near the contact is 0.8 %.)

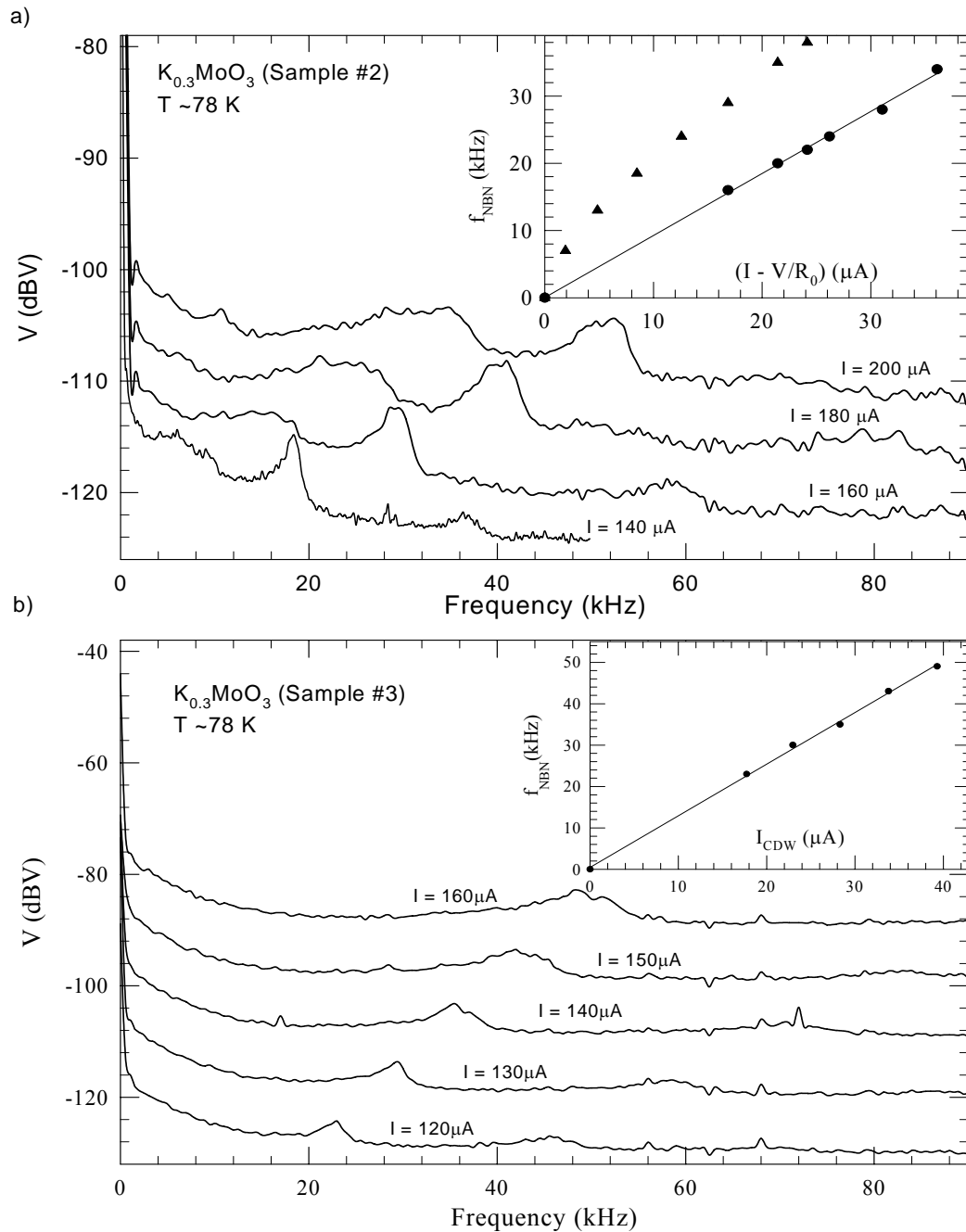


Figure 3.2 Sample-voltage NBN spectra at different dc currents for (a) Sample #2 ( $I_T = 110 \mu A$ ) at 78 K. For clarity, spectra for  $180 \mu A$  and  $200 \mu A$  are shifted up by 5 dB and 10 dB respectively. (b) Sample #3. Each spectrum is shifted by 10 dB (except for  $I = 120 \mu A$ ) for clarity. The inset graphs show the linear relationship between the fundamental (NBN) frequencies and the CDW currents. Sample #2 has two large fundamental frequencies whereas Sample #3 has just one fundamental frequency for each dc current.

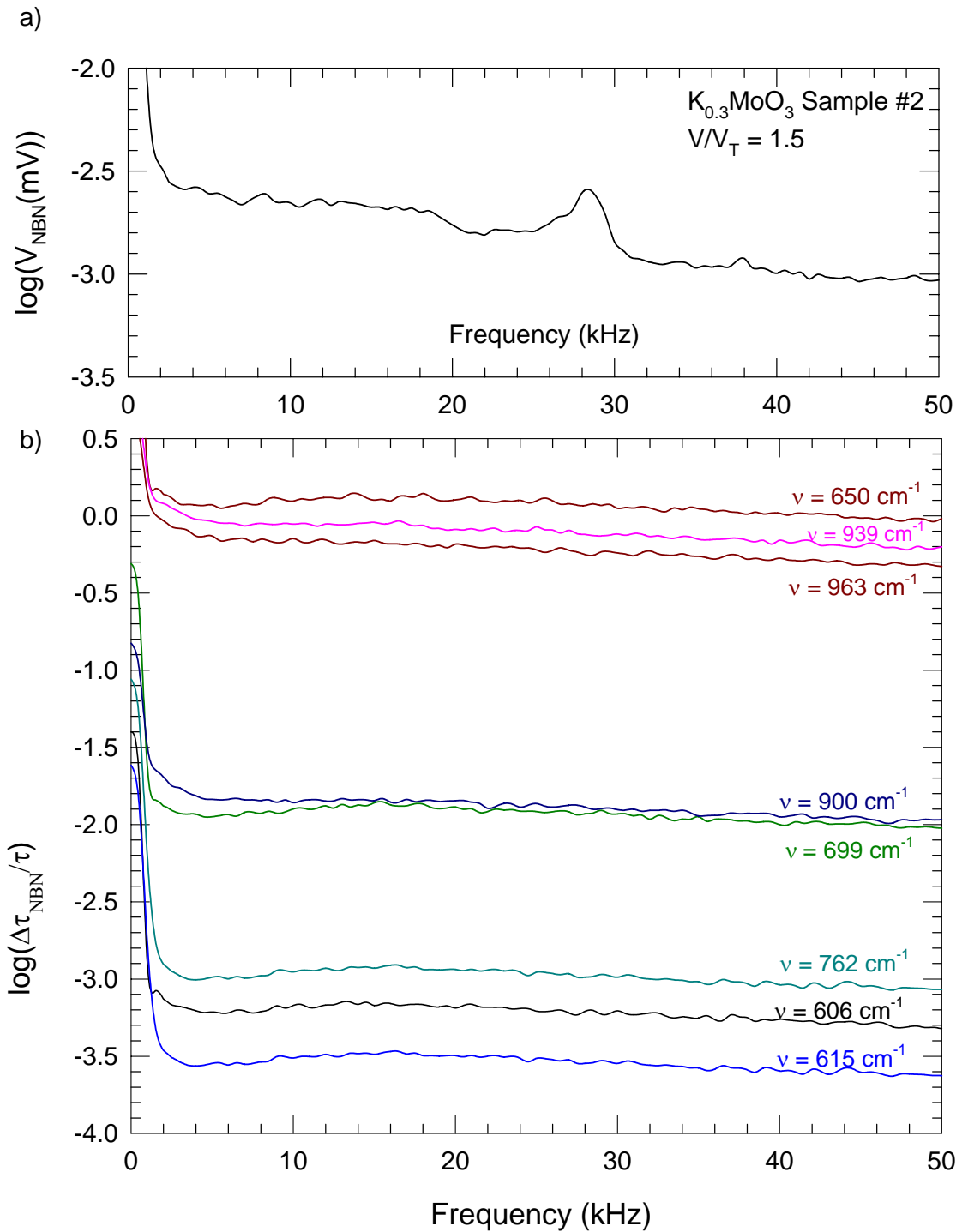


Figure 3.3 (a) NBN spectra of voltage across Sample #2 at  $V = 1.5V_T$ . (b) Fourier transforms of IR transmission signal through Sample #2 at  $V = 1.5V_T$ , position near ( $\sim 100 \mu\text{m}$ ) positive current contact.

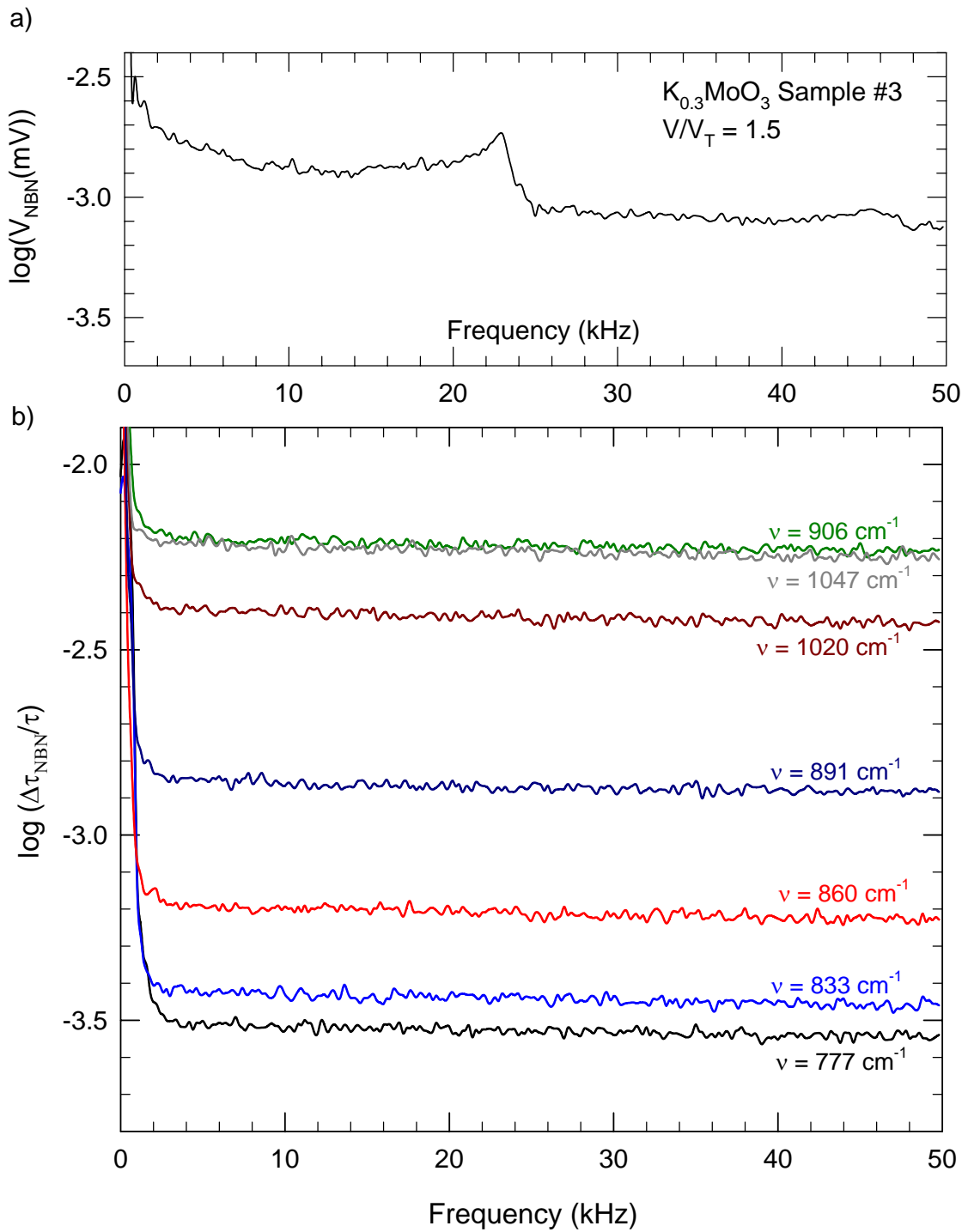


Figure 3.4 (a) NBN spectra of voltage across Sample #3 at  $V = 1.5V_T$ . (b) Fourier transforms of IR transmission signal through Sample #3 at  $V = 1.5V_T$ , position near ( $\sim 100\text{ }\mu\text{m}$ ) positive current contact.



The IR data of Figure 3.3 and 3.4 were taken with light transmitted through 0.1 mm windows adjacent to a contact. Similar null results (with similar noise floors) were obtained at other slit locations and sample voltages. Since the energy of  $\nu = 615 \text{ cm}^{-1}$  is near maximal in both the transmittance and laser power, this gives our minimum upper limit for  $\Delta\alpha_{NBN}$ . This limit corresponds to  $\Delta\alpha_{NBN} / \alpha < 0.05 \%$ .<sup>51</sup>

Similar measurements for NBN modulations of the infrared transmission were performed with a global light source. When the global was used for measurements, the laser system was turned off so that the noise introduced by mechanical vibration of the coldhead of the closed-cycle refrigerator was completely removed. However, the noise floor in the Fourier spectra with a global was comparable to the noise floor with a laser light source. No modulations in the infrared transmission were observed. (Fourier spectra with the global are not shown here).

If the NBN voltage is generated throughout the crystals<sup>76</sup>, then the measured NBN voltage is given by:

$$V_{NBN} = I_{NBN} R [\xi_{\parallel} \xi_{\perp}^2 / L w d]^{1/2} \quad (3.2)$$

where L and R are the sample length and resistance,  $\xi_{\parallel} \xi_{\perp}^2$  is the CDW velocity coherent volume<sup>77</sup>, and the last factor accounts for the incoherence of the current oscillations. The measured average absorption due to quasiparticles,  $\alpha^{qp}$ , will then oscillate at the NBN frequency with amplitude<sup>51</sup>:

$$\Delta\alpha_{NBN}^{qp} = [\Delta\rho_{NBN} / \rho] \text{Re}(\epsilon_0 / \epsilon_{\perp})^{1/2} (\sigma_{\perp} / \epsilon_0 c d) [\xi_{\parallel} \xi_{\perp} / d s^2]^{1/2} \quad (3.3)$$

Combining Equations 3.1-3.3, we find:

$$\Delta\alpha_{NBN}^{qp} = (L/w)^{1/2} \sigma_{\perp} \text{Re}(\epsilon_0 / \epsilon_{\perp})^{1/2} \Delta V_{NBN} / (s \epsilon_0 c R f \rho d \xi_{\parallel}) \quad (3.4)$$

where  $\sigma_{\perp}$  and  $\varepsilon_{\perp}$  are the transverse conductivity and dielectric constant,  $s^2$  ( $\sim 10^{-2} \text{ mm}^2$ ) is the illuminated area, and the term in brackets averages over the random phases of the density oscillations. Using values of  $\sigma_{\perp}$  and  $\varepsilon_{\perp}$  for blue bronze<sup>51</sup> and  $\Delta V_{NBN} = 3 \mu V$  gives  $\Delta\alpha_{NBN}^{qp} = 3 \times 10^{-5} / \xi_{\parallel}$ . Hence, our experimental limit  $\Delta\alpha_{NBN} = 0.3/cm$  implies that  $\xi_{\parallel} > 1 \mu m$ , comparable to the phase coherence length.<sup>78</sup>

If the narrow-band-noise were generated at the contacts by vortex motion<sup>22</sup>, the resulting modulation in absorption would be even smaller; since the phase-slip length<sup>25</sup>  $\Lambda \sim 100 \mu m$ , the resulting change in  $\alpha$  would be two order of magnitude smaller than our experimental limit.

In addition to absorption due to quasiparticles, there is significant phonon absorption at these subgap energies, and phonon absorption lines are also affected by CDW depinning, as discussed in Section 1.7.4. While the mechanism for these phonon changes is not known, we consider the possibility that the phonon changes may also oscillate at the NBN frequency. As shown in Figures 3.3 and 3.4, we searched, with negative results, for NBN absorption oscillations with the lasers tuned near phonon lines; since the IR absorption is strong near the lines, our sensitivity is greatly reduced. For example, near the strong  $\sim 900 \text{ cm}^{-1}$  absorption line<sup>57</sup>,  $\Delta\alpha_{NBN} < 10/cm$ , corresponding to a phonon energy oscillation  $\Delta\nu_{NBN} < 0.02 \text{ cm}^{-1}$ .

Finally, it has been suggested that the energies of intragap soliton states, needed for injection of charge into the CDW, would oscillate through the gap at the NBN frequency.<sup>27</sup> In this model of charge injection, there is one such soliton state per conducting chain, so that

$$\Delta\alpha_{NBN}^{SOL} \sim \beta \left[ \frac{\sigma^{SOL} e^2}{\hbar c \varepsilon^{1/2}} \frac{2\Delta}{\Gamma} \right] (1/\Lambda\Omega) (\eta \Gamma/\Delta) \sim 3\beta\eta/cm \quad (3.5)$$

where, as discussed in Appendix B, the factor in square brackets is the total soliton cross-section,  $\Lambda$  ( $\sim 0.1$  mm) is phase slip length,  $\Omega$  ( $\sim 15$  Å<sup>2</sup>) is the area per chain<sup>79</sup>,  $2\Delta \sim 1300$  cm<sup>-1</sup> is the CDW gap<sup>57</sup>, and  $\sigma^{\text{SOL}}$  is its geometric cross-section  $\sim 100$  Å<sup>2</sup> and  $\Gamma$  ( $\sim k_B T_C = 125$  cm<sup>-1</sup>) are the expected soliton cross-section and linewidth.<sup>57</sup>  $\eta$  is the fraction of time that the state's energy oscillates (i.e. the duty cycle) so that the factor in brackets gives the first harmonic content of the line oscillation. Finally,  $\beta$  is the coherence factor which can vary from  $\beta_{\text{MAX}} = 1$  if solitons oscillate coherently on all chains to  $\beta_{\text{MIN}} = (\Omega/sd)^{1/2} \sim 10^{-5}$  if the oscillations are incoherent on each chain. Our result  $\Delta\alpha_{\text{NBN}} < 0.3/\text{cm}$  implies that  $\beta\eta < 10^{-1}$ , limiting the duty cycle for coherent oscillations but not restricting  $\eta$  if the oscillations are incoherent.

In conclusion, we have searched for narrow-band-noise modulations of the infrared transmission in blue bronze, using tunable diode lasers. No modulation was observed, setting limits for various CDW properties.

### 3.2 Electro-Reflectance Spectra of Blue Bronze

As mentioned in Section 1.4, a long-standing question has concerned the mechanism by which electrons enter and leave the sliding CDW at current contacts. X-ray<sup>24</sup> and transport measurements<sup>53, 54</sup> have studied the spatial dependence of the CDW current and deformations, and have shown that current conversion involves additional CDW strains at the contacts above the more gradual, “bulk” CDW polarization strain; both bulk and contact strains have also been observed through position dependent changes in the infrared transmission<sup>25</sup>. The contact strains are believed to drive CDW phase-slip through the growth and climb of “macroscopic” CDW dislocation loops.<sup>24, 53, 54, 80, 81</sup> Microscopically, these loops are thought to form from the condensation of  $2\pi$  phase-solitons (corresponding to 2 electrons entering or leaving the CDW), with energy levels near the edge of the CDW gap, on the individual chains.<sup>26</sup> However, such current-induced intragap soliton/dislocation states have not been observed.

The sample preparation procedure was described in Section 2.4; however a brief review is presented here. Smooth sample surfaces were prepared and gold films were evaporated on the ends of the crystals for current contacts, separated by  $\sim 1$  mm. Electrical and thermal contacts to the sample were made by attaching its ends with silver paint to a sapphire substrate in a liquid nitrogen cryostat. All measurements were made with the sapphire substrate at  $\sim 78$  K, although the sample may have been a few degrees warmer than this. Infrared diode lasers, covering the range  $400\text{ cm}^{-1}$  to  $1200\text{ cm}^{-1}$  with a typical power of  $0.5\text{ mW}$ , were used as light sources. The lasers were not mode selected and typically there were several modes spread over  $\gamma \sim \pm 7\text{ cm}^{-1}$ . An IR microscope was used to vary the position of the illuminated light spot (typically  $50\text{ }\mu\text{m} \times 50\text{ }\mu\text{m}$ ) on the sample.

For all electro-reflectance measurements, square-wave voltages at frequency  $\Omega$  were applied to the sample, and changes in the reflected intensity in phase with the applied voltage as well as the intensity of the reflected light (chopped at an incommensurate frequency  $\omega$ ) were measured simultaneously with two lock-in amplifiers. The square-wave frequency  $\Omega$  was kept high enough so that signals due to modulations of the sample's temperature were negligible. We note that there was often also a small electro-reflectance response in quadrature with the applied voltage, reflecting the time delay of the CDW polarization<sup>8</sup> and residual thermal effects. The ratio of the two lock-in signals represents the relative change in reflectance (i.e. electro-reflectance signal),  $\Delta R/R$ . For reflectivity spectra, the intensity of the reflected light was measured by moving the light spot back and forth between the sample and the gold mirror (near contacts on the samples) at each laser frequency.

The infrared transmission ( $\tau$ ) varies spatially in response to an applied voltage as discussed in Section 1.7. Near the center of the sample, the relative change in transmission ( $\Delta\tau/\tau$ ) varies approximately linearly with position, reflecting the bulk polarization of the CDW, but larger changes are observed near ( $\sim 0.1\text{ mm}$ ) the current contacts<sup>25</sup>, as shown in Figure 1.9b. It was suggested<sup>8</sup> that the variation in  $\Delta\tau/\tau$  largely reflects changes in intraband absorption by thermally excited quasiparticles, although

pronounced spectral changes in  $\Delta\tau/\tau$  associated with small changes of phonon frequencies, lifetimes, and oscillator strengths caused by the strained CDW were also observed<sup>57</sup>, as shown in Figure 1.10. The bulk and contact electromodulated transmission spectra were compared to search for new absorption features that could be associated with intragap electronic states caused by current injection into the CDW. No such absorption features were observed<sup>57</sup>, giving an upper limit to  $[n\sigma/\Gamma]$ , where  $n$  is a soliton density,  $\sigma$  is the geometric cross-section, and  $\Gamma$  the soliton linewidth (see Equation 16 in Appendix B):

$$n\sigma/\Gamma \sim \varepsilon_1^{1/2} \delta(\Delta\tau/\tau)/(e^2/\hbar c)\nu_0 d < 5 \times 10^{-10} (\text{\AA cm}^{-1})^{-1} \quad (3.6)$$

where  $\delta(\Delta\tau/\tau)$  was the difference in the (normalized) contact and bulk electromodulated transmission signals ( $< 4 \times 10^{-5}$ ),  $\nu_0 = 1100 \text{ cm}^{-1}$ ,  $d \sim 3.5 \text{ }\mu\text{m}$  the thickness of the sample, and  $\varepsilon_1 \sim 12$ <sup>35, 82</sup> is the real part of the background dielectric constant. Using the expected values of  $\Gamma \sim k_B T_c (\sim 125 \text{ cm}^{-1})$ <sup>26</sup>,  $n = 10^{16}/\text{cm}^3 \sim 1/\text{chain}$ , and  $\sigma \sim \xi_{\parallel} \xi_{\perp} \sim 100 \text{ \AA}^2$ , where  $\xi_{\parallel}$  and  $\xi_{\perp}$  are the longitudinal and transverse CDW amplitude coherence lengths<sup>40</sup>, this implies that midgap states occur on less than 7% of the chains, whereas we expect all chains to have such states for large CDW currents. However, because of the strong absorption of light polarized parallel to the conducting chains, the transmission spectra could only be measured for transversely polarized light. In fact, as discussed in Appendix B, Equation 3.6 was adapted from a quasi-one-dimensional model from which it is not clear if it is appropriate to take  $\sigma \approx \xi_{\parallel} \xi_{\perp}$  for transversely polarized light. That is, it is not clear if solitons can be optically excited with transverse polarized light. Therefore, since the absorption is too strong for parallel polarized light to make transmission experiment possible, these results motivated a search for voltage induced changes in the infrared reflectivity and measurements of its spectra. The results of these measurements are reported in this section.

Although our ultimate goal was to search for differences in the parallel polarized contact and bulk electro-reflectance spectra, we first examined the spectrum, and spatial

dependence for the transverse polarization, to verify that the reflectivity behaved as expected from the transmission. Comparison of phonon modulations due to the sliding of the CDW has been done for electro-transmission and electro-reflectance spectra.

### 3.2.1 Voltage and Spatial Dependences of the Electro-Reflectance

Figure 3.5a shows the voltage dependence of electro-reflectance signals for a blue bronze sample (Sample #1 with a threshold voltage  $V_T = 15$  mV) near the positive contact at 78 K. Shown are the variations for a bipolar square wave (with  $\Delta R \equiv [R(+V) - R(-V)]$ ) and a positive unipolar square wave (with  $\Delta R \equiv [R(+V) - R(0)]$ ). Although the voltage dependence shown is for the light polarized transverse to the chain direction, qualitatively similar voltage dependences were also observed for the parallel polarized light. The open circles show the (dc) non-linear I-V curve. The sliding of the CDW at the threshold voltage of  $V_T = 15$  mV is noted by the onset for the non-linear current  $I_{CDW} = I - V/R_0$  (where  $R_0$  is the normal resistance) as shown in the figure. The electro-reflectance signal is very small for applied voltages below the dc threshold voltage (for both unipolar and bipolar square wave voltages), whereas in the case of the transmission (as discussed in Section 1.7.1), the electromodulated transmission signal had a stronger onset at  $V_p < V_T$  for bipolar voltages. For most laser wavelengths, the very small value of  $\Delta R/R$  for voltages below  $V_T$  for bipolar voltages suggests that the bulk and contact polarizations begin at approximately same voltage on the sample surface. Above the threshold voltage,  $\Delta R/R$  slowly increases with square wave voltages and does not seem to saturate even at very high voltages. Also contrary to the voltage dependence of  $\Delta\tau/\tau$ , the voltage dependence of  $\Delta R/R$  was found to be laser wavelength dependent. Although the voltage dependences of  $\Delta R/R$  are similar at higher voltages for all laser wavelengths, they are strikingly different near threshold voltage as shown in Figure 3.5b. For bipolar voltages below 24 mV,  $\Delta R/R$  changes sign at  $\sim 10$  mV for laser light  $\nu = 1050$   $\text{cm}^{-1}$  whereas  $\Delta R/R$  starts with no inversion at threshold (as for most of laser wavelengths) for laser light  $\nu = 535$   $\text{cm}^{-1}$ . Such sign inversion of  $\Delta R/R$  was not observed in electro-transmission

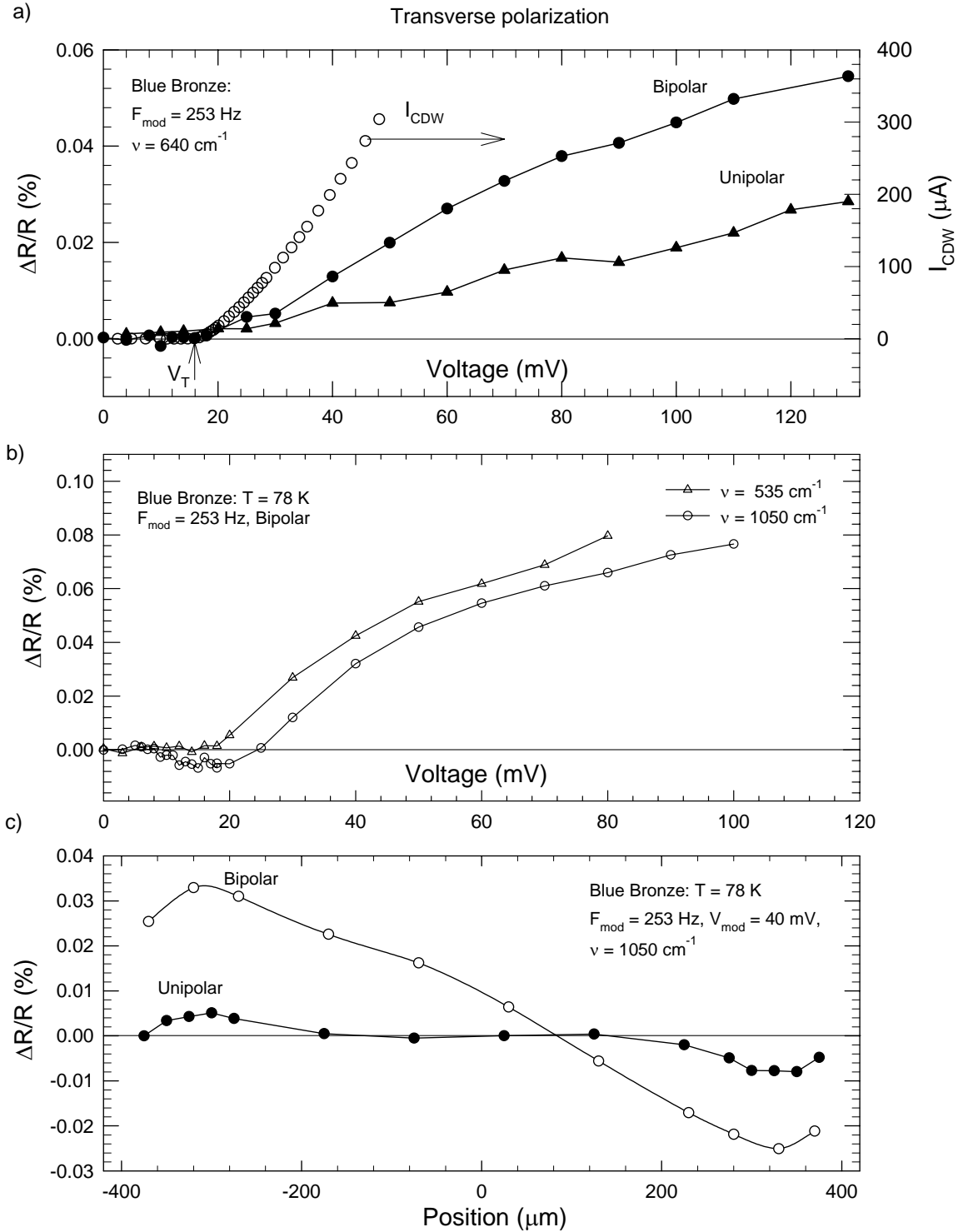


Figure 3.5 For Sample #1; (a) Voltage dependence of  $\Delta R/R$  for bipolar, unipolar voltages (adjacent to contact), and the CDW current, (b) Voltage dependence of  $\Delta R/R$  for  $\nu = 535$   $cm^{-1}$  and  $1050$   $cm^{-1}$  (adjacent to contact), and (c) Spatial dependence of  $\Delta R/R$  for bipolar and positive unipolar square-wave voltages at 40 mV.

measurements. Figure 3.5c shows the spatial dependence of  $\Delta R/R$  (at  $1050 \text{ cm}^{-1}$ ) for transversely polarized light.

This electro-reflectance, although expected in view of our transmission experiments, constitutes the first observation of position dependent changes in the reflectivity associated with CDW depinning. (We note, however, that spatially uniform changes in the far infrared reflectivity, including resonance-like features associated with CDW motion through the lattice, have been reported.<sup>83</sup>) The 40 mV spatial dependences shown in Figure 3.5c are basically similar to what was observed in transmission experiments:<sup>25, 57</sup> for the unipolar square-wave the CDW stays pinned and the polarization does not relax when the voltage is zero, so that only electromodulated signals due to the contact strains (associated with CDW motion) are observed, whereas for the bipolar square wave both contact and bulk signals are observed, and the spatial profile of  $\Delta R/R$  varies linearly near the center of the sample for bipolar voltages. However one difference between reflectance spatial profiles and our previous transmission profiles<sup>25</sup>, (e.g. Figure 1.9) is that decreases in  $|\Delta R/R|$  are observed adjacent to the contacts; no corresponding decrease was ever observed in  $\Delta\tau/\tau$ . A similar spatial profile is observed for the parallel polarization, as shown below in Figure 3.10.

In order to further study the differences with the electro-transmission, the spatial profile of  $\Delta R/R$  was measured for several voltages and frequencies as shown in Figure 3.6. For all voltages, the bulk response is linear and changes sign near the middle of the sample as expected. However the downturn in  $\Delta R/R$  near contacts as seen for 40 mV gets deeper as the applied voltage becomes smaller and finally this decrease actually becomes an inversion for voltages below 25 mV, as also seen in Figure 3.5b. No corresponding effect was observed for the transmission<sup>25</sup>, suggesting that the CDW polarization is different on the surface (probed by reflectance) than throughout the volume (probed by transmission), e.g. because of inhomogeneous current flow (e.g. current is injected from the gold contacts on the surface), band bending at the contacts, surface reconstruction of the CDW, and/or surface pinning of the CDW. As shown in Figure 3.6b, the downturn in  $\Delta R/R$  near contacts is just beginning at 1.34 kHz for 40 mV. This frequency dependence



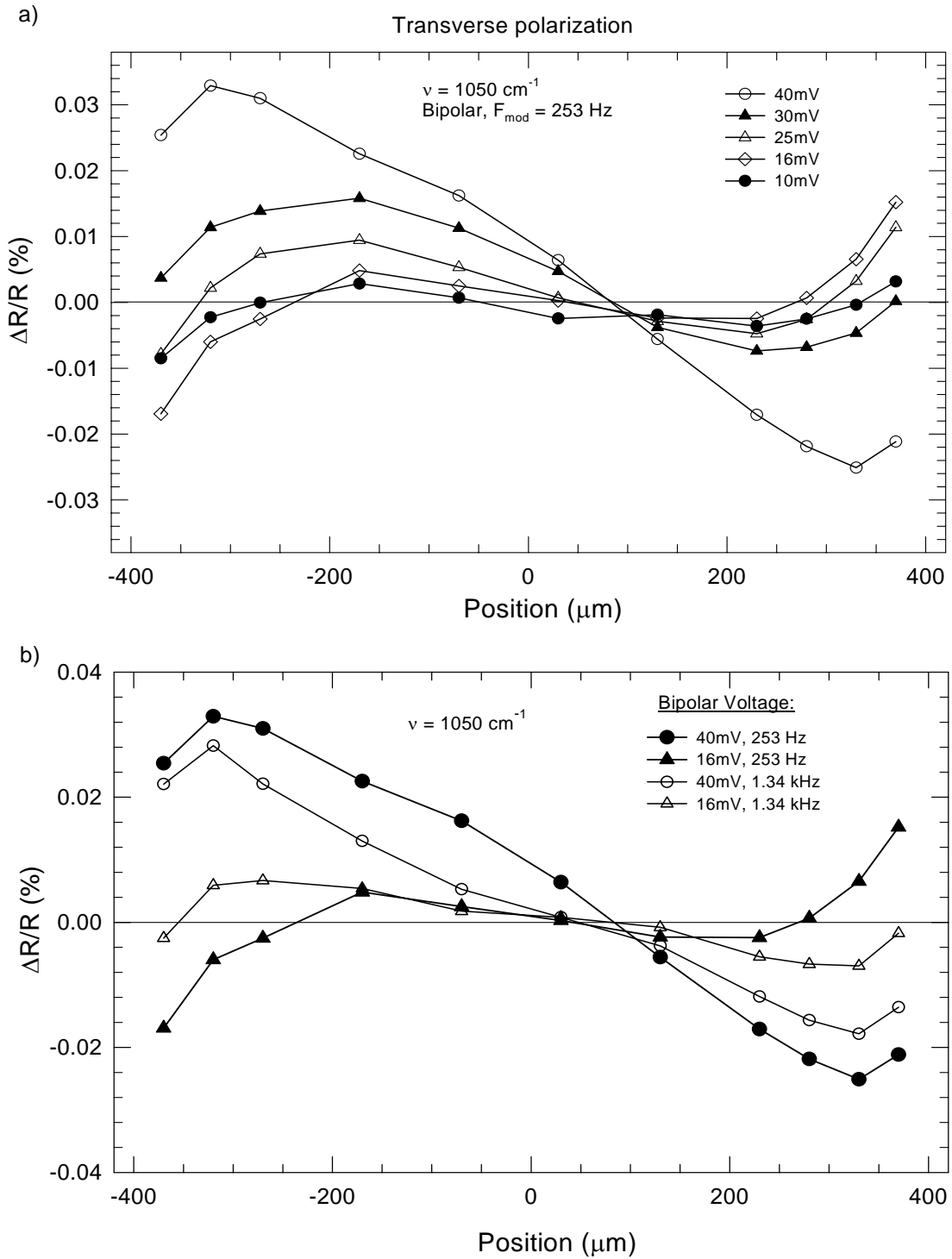


Figure 3.6 Spatial profiles of  $\Delta R/R$  for transverse polarized light at  $1050 \text{ cm}^{-1}$   
 (a) Several bipolar square-wave voltages at 253 Hz. (b) Bipolar voltages 40 mV and 16 mV at each 253 Hz and 1.34 kHz.

indicates that the inversion takes time  $\sim 1$  ms to develop. The underlying physics of this unusual inversion is not understood; it varies in different runs. The wavelength dependence, mentioned above, may affect the fact that different wavelengths probe different depths in the sample. However, we have not yet determined what parameters (e.g. history, temperatures) are important.

Reflectance measurements on the back surface (i.e. behind the contact) as well as combined transmittance/reflectance measurements may be required to understand the physical reason for such inversions. Future experiments on samples thin enough to measure both reflectance and transmission will allow a more systematic study of the differences between the transmission and reflectance spatial profiles as functions of voltage, square-wave frequency, and wavelength.

### 3.2.2 Effects of CDW Polarization on Phonons

Figure 3.7 shows that electromodulated reflectivity spectrum for the transverse polarization (at  $V = \pm 80$  mV,  $37 \mu\text{m}$  from the contact). The reflectivity spectrum, similar to that obtained by others<sup>35, 82</sup>, is shown in Figure 3.7a (plotted logarithmically to facilitate analysis of the electro-reflectance). As expected from the electromodulated transmission spectrum, there are sharp features in the electro-reflectance (Figure 3.7b) associated with phonon lines, labeled with letters (A-J) as in reference.<sup>57</sup> In fact, the phonon features seem to dominate the electro-reflectance spectrum much more than for the electro-transmission spectrum<sup>57</sup>, for which there was also a large broadband signal, as shown Figure 1.10. However, whereas changes in phonon linewidths ( $\Gamma_j$ ), frequencies ( $\nu_j$ ), and oscillator strengths ( $M_j$ ) lead to very distinct changes ( $2^{\text{nd}}$ -derivative,  $1^{\text{st}}$ -derivative, and  $0^{\text{th}}$ -derivative lineshapes, respectively) in the electro-transmission spectrum<sup>57</sup>, all three result in more complex and less distinct changes in the electro-reflectance spectrum (as shown below), complicated further by the breadth and overlap of the Fano reflectance lines. This makes it especially difficult to determine the *signs* of the changes in phonon properties, but the magnitudes of the changes can be roughly determined from

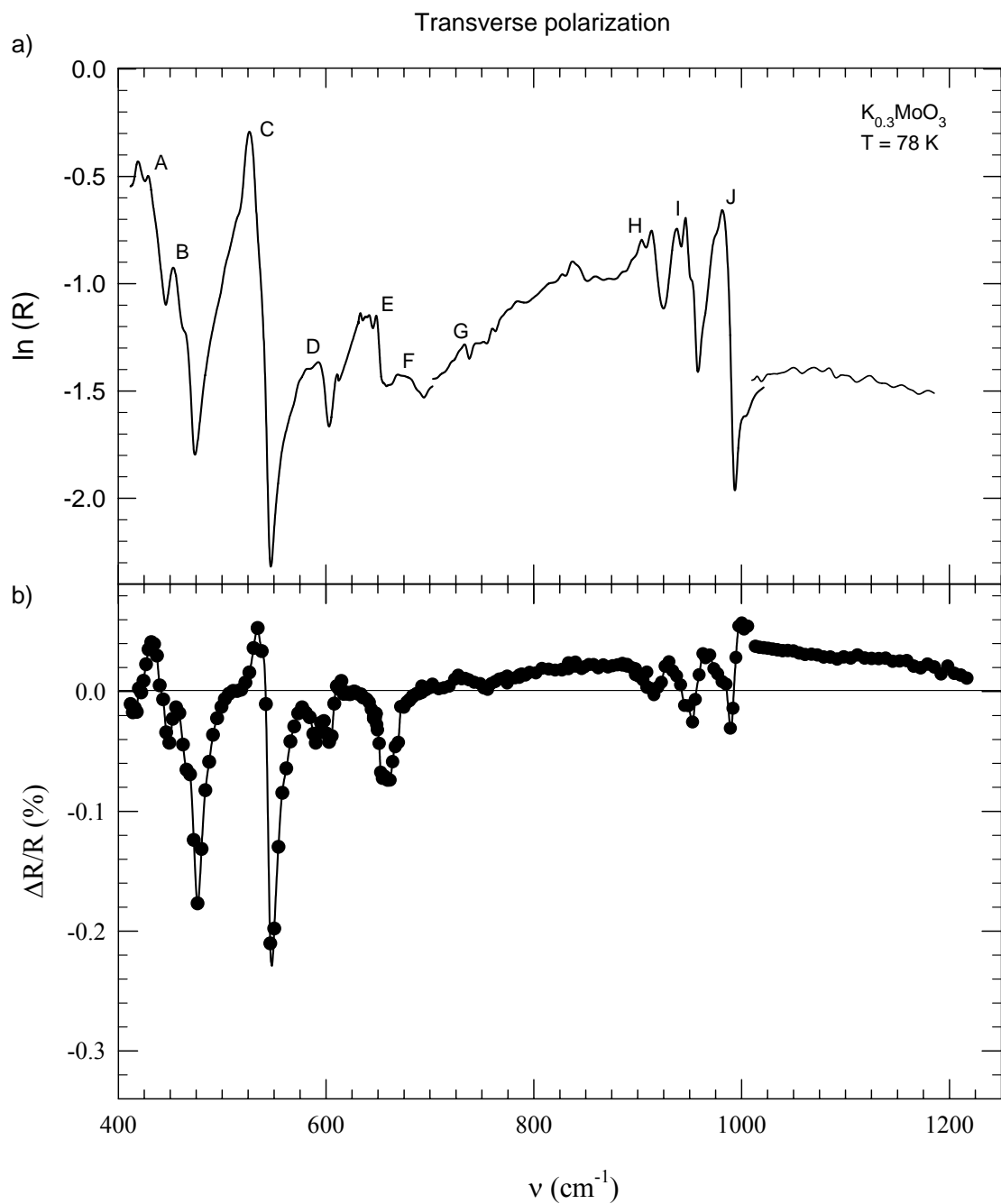


Figure 3.7 (a) Reflectivity spectrum for transverse polarization. Phonon resonances are labeled A - J. (b) Electro-reflectance spectrum for transverse polarization, measured with 253 Hz, 80 mV bipolar square-wave near the contact.

$$|\Delta\nu_j| \sim |\Delta\Gamma_j| \sim \Gamma_j |\Delta M_j / M_j| \sim \Gamma_j [\Delta R / R] / \delta \ln R, \quad (3.7)$$

where  $\delta \ln R$  is the magnitude of the drop in  $\ln R$  for that phonon. For all the phonons (except for F), we find  $|\Delta\nu_j|$  and/or  $|\Delta\Gamma_j|$  to be between  $\sim 0.01$  and  $0.04 \text{ cm}^{-1}$  (or for phonon A<sup>57</sup>, a change in oscillator strength  $\sim 0.1\%$ ), similar to what was deduced from the electro-transmission.<sup>57</sup> However, there now appears to be a very large change ( $|\Delta\nu_j|$  and/or  $|\Delta\Gamma_j| \sim 0.1 \text{ cm}^{-1}$ ) for F, for which no change could be observed in the transmission.<sup>57</sup> Whether these differences are sample (or temperature) dependent effects, artifacts of the analysis, or indications that phonon changes are different near the surface must be addressed by comparisons of the electro-transmission and electro-reflectance on the same samples with a more quantitative modeling of the spectra.

The changes in phonons due to the CDW polarization can be studied in more details by fitting the reflectance spectrum first and then fitting the electro-reflectance spectrum with parameters from the fit of the reflectance spectrum. For the fits of reflectance, only the spectral region from  $845 \text{ cm}^{-1}$  to  $1080 \text{ cm}^{-1}$  was studied since the 3 phonons in this region are relatively distinct, whereas the lower frequency phonons are complicated by their overlapping line shapes. While the phonon modulations due to the CDW polarization can be better understood if both the reflectance and transmittance spectra (Figure 1.10) were fit simultaneously, such fits were poor, possibly because the reflectance and transmittance were measured for different samples or because of small changes in the frequency calibration of the lasers used for the two measurements (which were measured at different times). Therefore, the complete studies and comparisons of the electro-transmission and electro-reflectance on the same samples with a more quantitative modeling of the spectra are left for future work.

The reflectance for normally incident light in terms of the real,  $\epsilon_1$ , and imaginary,  $\epsilon_2$ , parts of the dielectric function (see Appendix A) is

$$R = \frac{1 + \sqrt{(\varepsilon_1^2 + \varepsilon_2^2)} - \sqrt{2(\varepsilon_1 + \sqrt{\varepsilon_1^2 + \varepsilon_2^2})}}{1 + \sqrt{(\varepsilon_1^2 + \varepsilon_2^2)} + \sqrt{2(\varepsilon_1 + \sqrt{\varepsilon_1^2 + \varepsilon_2^2})}} \quad (3.8)$$

The dielectric constant due to phonons is taken as

$$\varepsilon_1(\nu) = \varepsilon_b + \sum_j \frac{A_j (\nu_j^2 - \nu^2)}{(\nu_j^2 - \nu^2)^2 + \nu^2 \Gamma_j^2},$$

$$\varepsilon_2(\nu) = \sum_j \frac{A_j \nu \Gamma_j}{(\nu_j^2 - \nu^2)^2 + \nu^2 \Gamma_j^2} \quad (3.9)$$

where  $\varepsilon_b$  is the background dielectric constant,  $A_j$  is proportional to the oscillator strength,  $\Gamma_j$  is the linewidth, and,  $\nu_j$  is the frequency of the phonon in the spectrum. For simplicity, we omit the imaginary part of the background dielectric constant since it is smaller than the real part and therefore only weakly affects the reflectivity. The reflectivity spectrum (from 845  $\text{cm}^{-1}$  to 1080  $\text{cm}^{-1}$ ) and its fit with Equation 3.8, with  $\varepsilon_1$ , and  $\varepsilon_2$  given by Equation 3.9 are shown in Figure 3.8. There are altogether 10 fitting parameters (i.e.  $\varepsilon_b$  and three parameters ( $A, \nu, \Gamma$ ) for each of the three phonons). The values of the fitting parameters are listed in Table 1. In an attempt to understand the phonon modulations due to the CDW polarization, we took these parameters and attempted to visually fit the electro-reflectance spectrum by varying one or more parameters while keeping the remaining parameters fixed. Several such “visual” fits to electro-reflectance spectra are shown in Figures 3.9a-f.

The fit by changing  $\Delta\varepsilon_b = +0.045\%$  qualitatively resembles the electro-reflectance spectrum, as shown in Figure 3.9a. For the transmittance, changes in the background conductivity (i.e. the imaginary part of the dielectric constant) and changes in the phonon parameters have additive effects on the electro-transmittance, whereas changes in  $\varepsilon_b$  affect the shapes of the phonon features, as shown in the figure. As shown in Figure 3.9b, the fit by varying  $A_j$ 's only qualitatively matches with the electro-

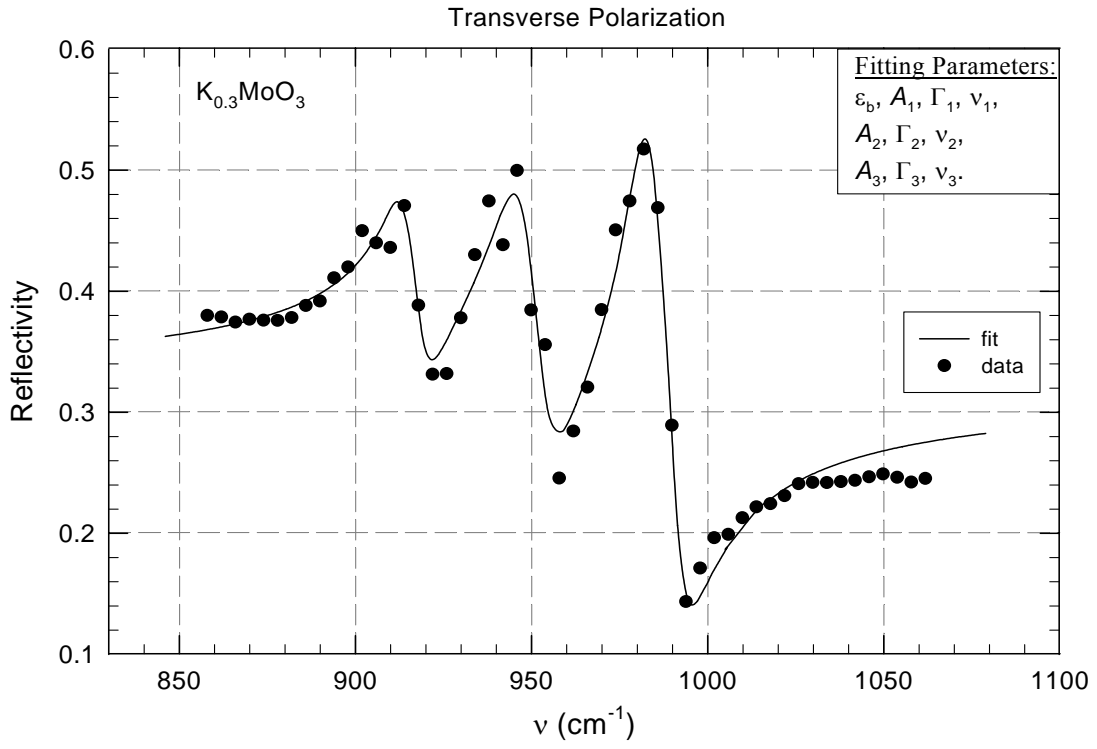


Figure 3.8 A portion of reflectivity spectrum (in Figure 3.7) for transverse polarized light. The solid line represents the fitted curve.

Table 1: The values of the fitting parameters.

$\epsilon_b$	$12.96 \pm 1.23$
$A_1$	$(1.42 \pm 0.23) \times 10^5 \text{ cm}^{-2}$
$\Gamma_1$	$10.20 \pm 2.65 \text{ cm}^{-1}$
$\nu_1$	$914.00 \pm 1.06 \text{ cm}^{-1}$
$A_2$	$(2.24 \pm 0.22) \times 10^5 \text{ cm}^{-2}$
$\Gamma_2$	$12.88 \pm 2.03 \text{ cm}^{-1}$
$\nu_2$	$945.65 \pm 0.82 \text{ cm}^{-1}$
$A_3$	$(2.06 \pm 0.123) \times 10^5 \text{ cm}^{-2}$
$\Gamma_3$	$9.50 \pm 1.04 \text{ cm}^{-1}$
$\nu_3$	$980.54 \pm 0.55 \text{ cm}^{-1}$

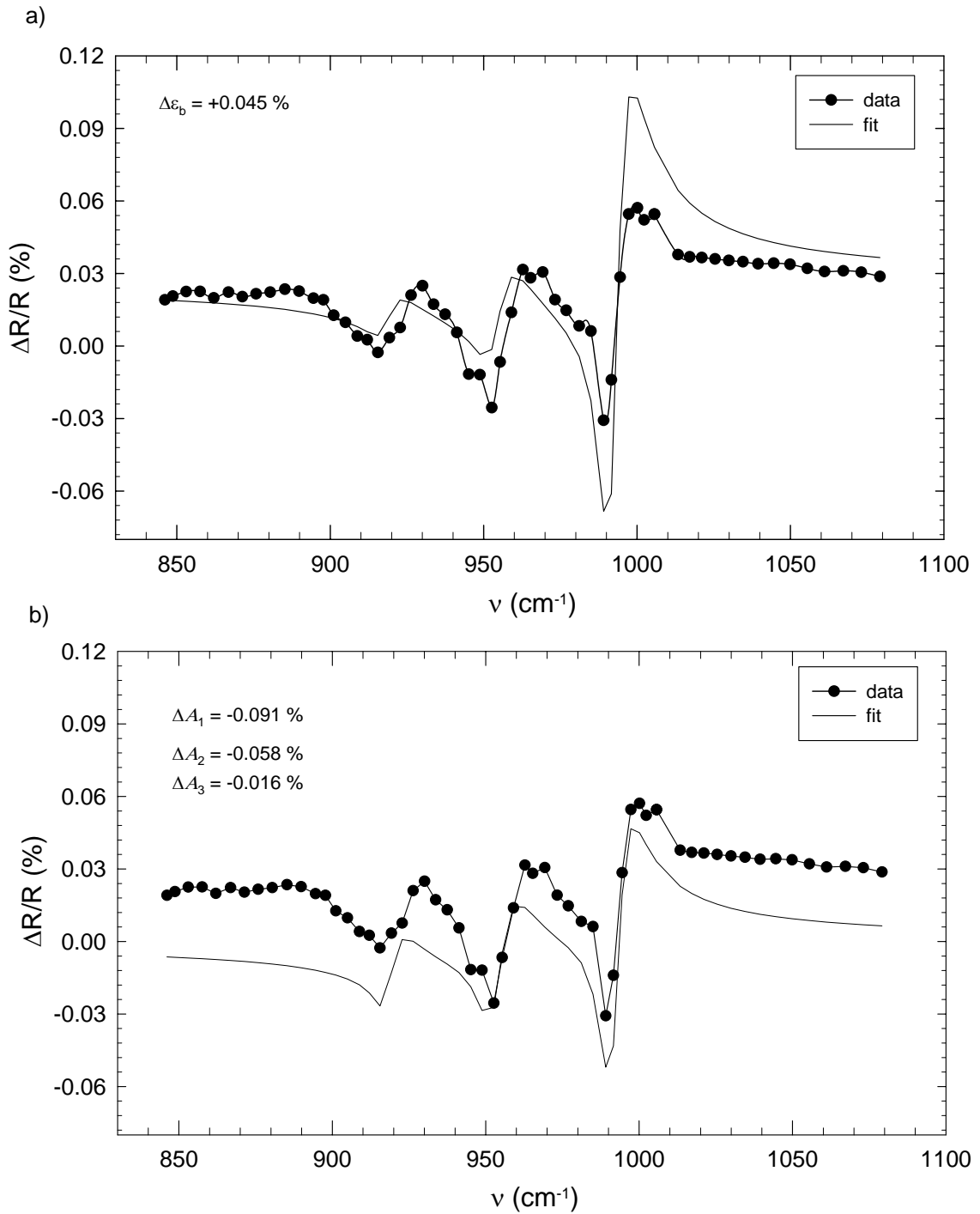


Figure 3.9 Fits of the electro-reflectance spectrum by varying different parameters as indicated in each graph: (a) only  $\epsilon_b$  is changed, (b)  $A$ 's are changed for all three phonons.

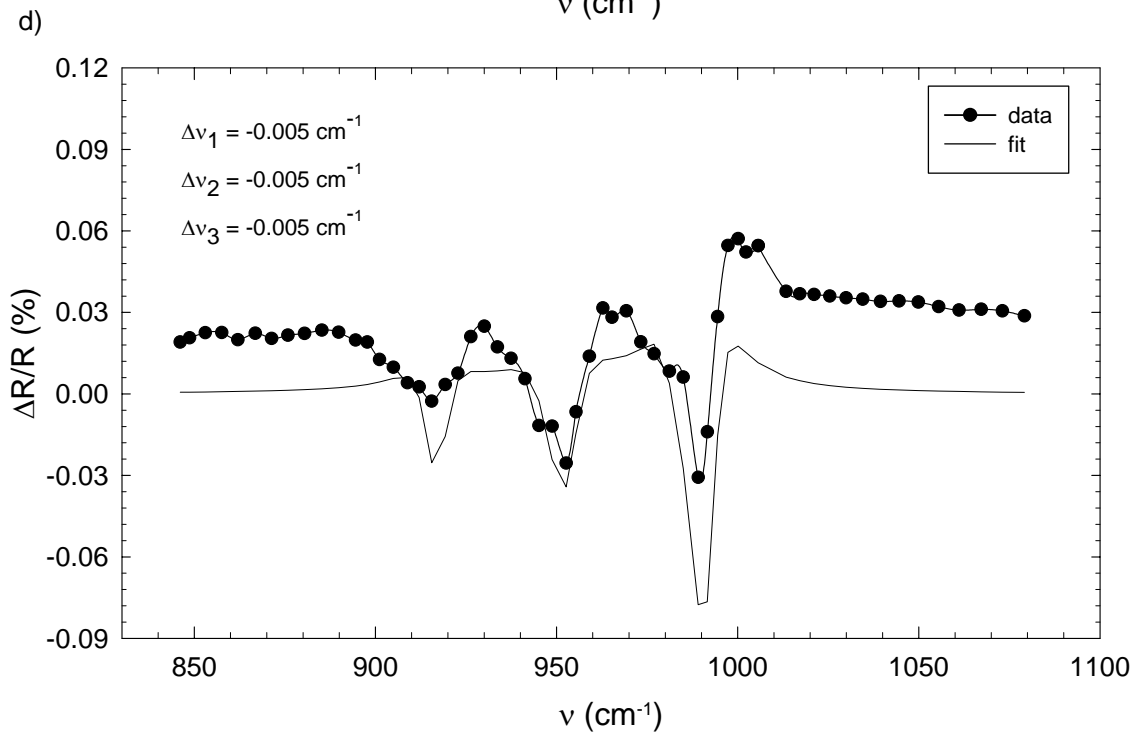
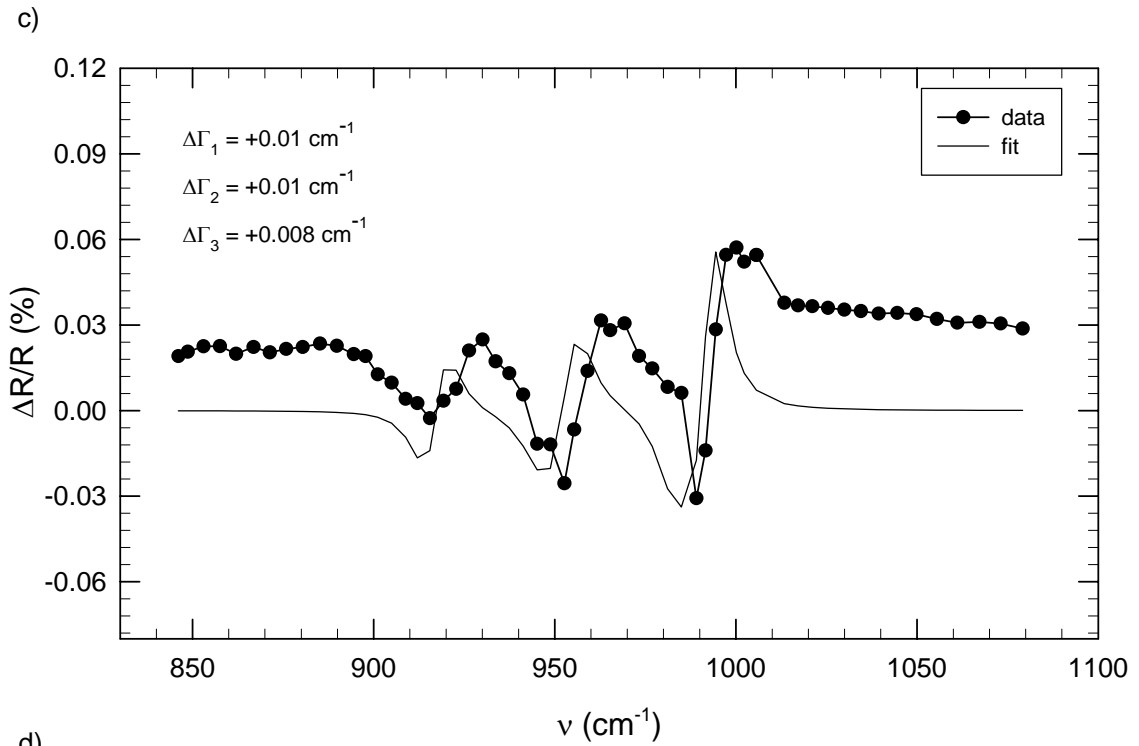


Figure 3.9 Fits of the electro-reflectance spectrum by varying different parameters as indicated in each graph: (c)  $\Gamma$ 's are changed for all three phonons, (d)  $\nu$ 's are changed for all three phonons.



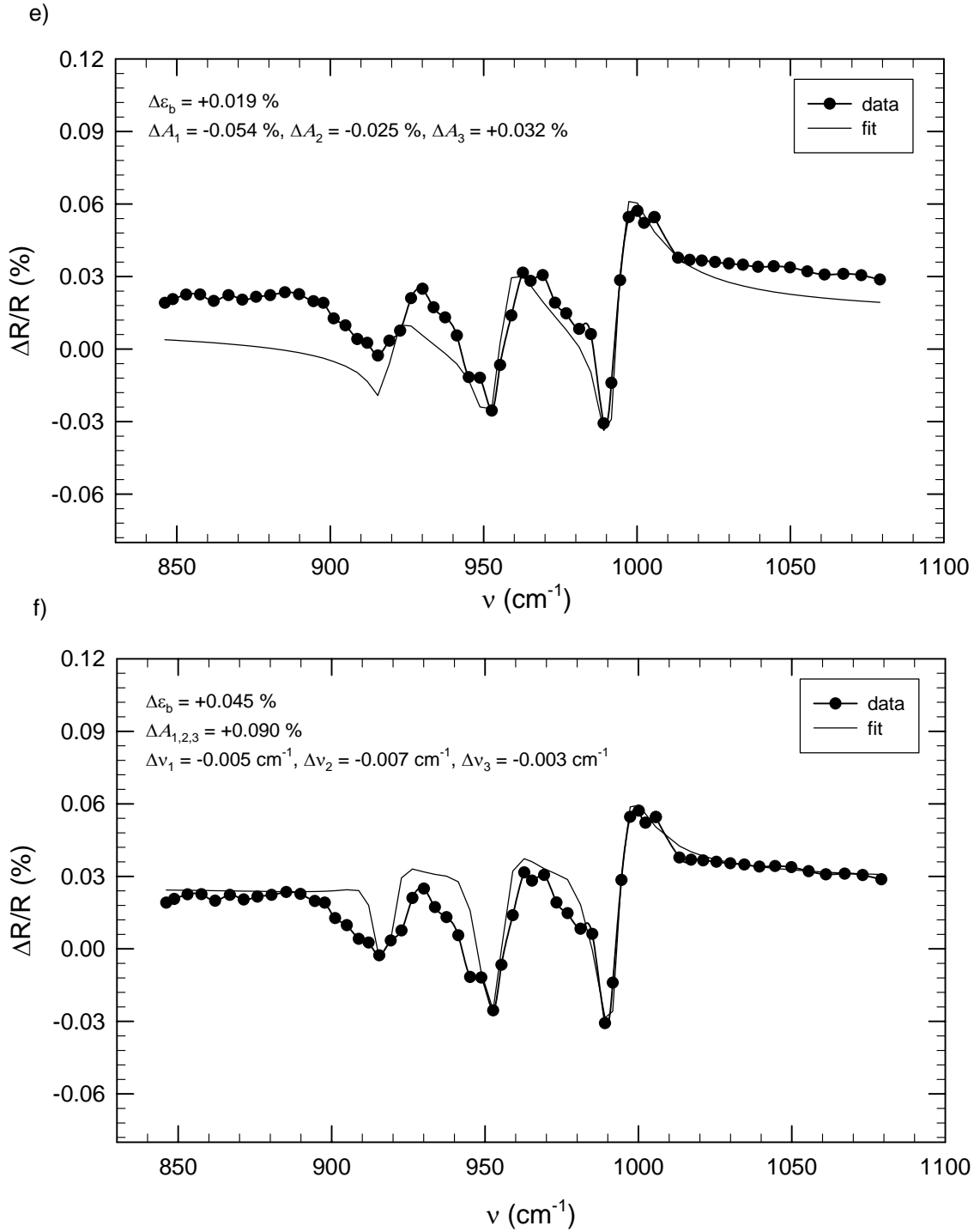


Figure 3.9 Fits of the electro-reflectance spectrum by varying different parameters as indicated in each graph: (e)  $\epsilon_b$ , and  $A$ 's are changed for all three phonons, and (f)  $\epsilon_b$ ,  $A$ 's, and  $\nu$ 's are changed for all three phonons.

reflectance data, but does not do as well in fitting the background. Figures 3.9c and 3.9d show the fits to  $\Delta R/R$  by varying the linewidths and the frequencies of all three phonons. Changes in the frequencies,  $\sim 0.005 \text{ cm}^{-1}$  (consistent with the electro-transmission results<sup>57</sup>) qualitatively match the data, except that, as for oscillator strength changes, they can not match the background. Changing the linewidths, however, does a much poorer job of fitting the phonon spectra.

Of course, the fits to the data get even better if more than one set of parameters are changed. By changing the  $A_j$ 's and the background dielectric constant independently, two phonons are fitted very well as shown in Figure 3.9e. Typical changes in the  $A_j$ 's and  $\epsilon_b$  are  $\sim 0.05 \%$  and  $\sim 0.02 \%$  respectively. Note that changing any one phonon parameter affects the fits of the other phonons. Finally, the fit to the data from varying  $\epsilon_b$ ,  $A_j$  and  $\nu_j$  simultaneously is shown in Figure 3.9f. This fit is good for the second and third phonons, whereas the fit to the first phonon is not as good.

These results show that, unlike from the electro-transmission which suggested frequency shifts of order  $\sim 0.01 \text{ cm}^{-1}$  for these three phonons, it is impossible to unambiguously associate the electro-reflectance spectra with changes in specific phonon properties. The changes in electro-reflectance spectra are complicated and difficult to analyze. The order of magnitude of possible phonon changes can be estimated however:  $\Delta A \sim 0.05\%$ ,  $\Delta \nu \sim 0.005 \text{ cm}^{-1}$ . The changes are consistent with the changes estimated from Equation 3.7. However, the best fits are obtained by including changes in the background dielectric constant. Note that the order of magnitude of the changes in  $\epsilon_b$  ( $\sim 0.045 \%$ ) is much less than that of in quasiparticle density and conductivity ( $\sim 1 \%$ ) deduced from the electro-transmittance.<sup>8</sup>

### 3.2.3 Parallel Electro-Reflectance Spectra

Figure 3.10 shows the spatial dependence of  $\Delta R/R$  for bipolar and unipolar square wave voltages for Sample #1. The vertical arrows show the locations on the sample

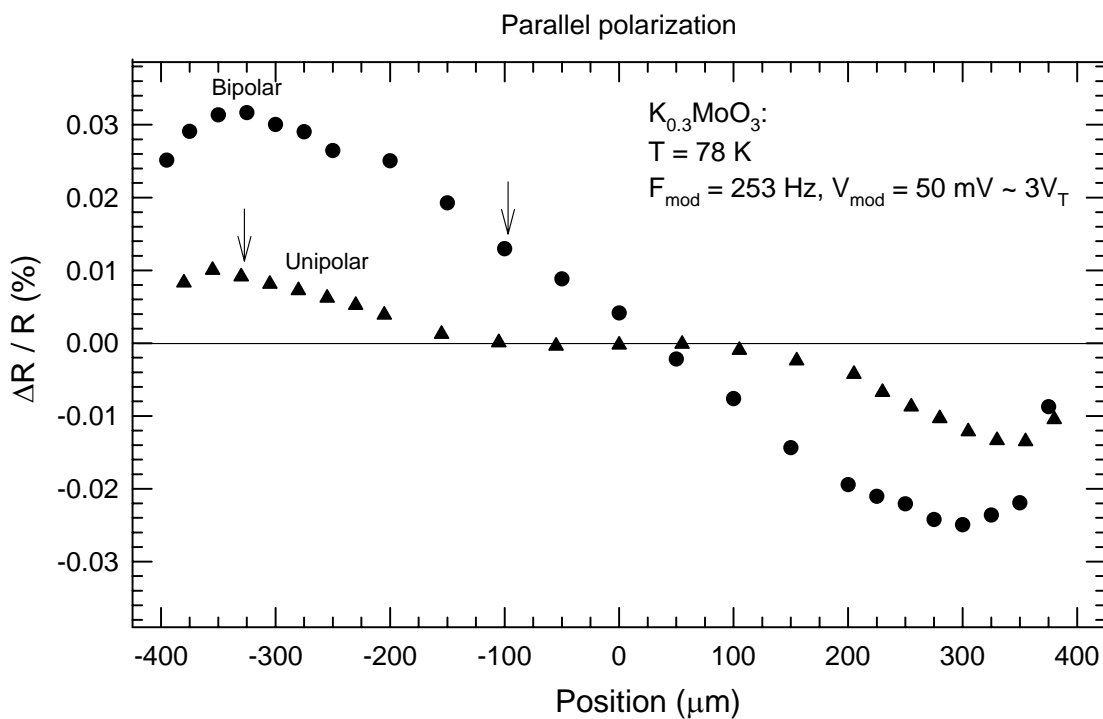


Figure 3.10 Spatial dependence of the relative change in reflectivity when applying 253 Hz square-wave voltages. ( $715\text{ cm}^{-1}$ , parallel polarized light) Closed circle: 50 mV, bipolar square-wave. Closed triangles: 50 mV, positive unipolar square-wave. The vertical arrows show the locations of the spectra shown in Figures 3.11.

where the bulk and contact spectra were taken. Figure 3.11a shows the parallel reflectance spectrum, similar to the published results<sup>35, 82</sup>; we denote 6 phonon modes with letters K-P. The bulk and contact electro-reflectance spectra, taken at the locations shown by the arrows in Figure 3.10, are shown in Figure 3.11b, with the contact spectrum multiplied by a normalization factor  $N = 1.9 \pm 0.3$  for direct comparison. (The value of  $N$  varied slightly for spectra taken with different lasers, possibly because the positions of the images of the microscope aperture varied slightly for different laser positions.) Similar reflectance and electro-reflectance spectra were obtained for a second sample as shown in Figure 3.12. The reflectivity spectra of two samples are similar except in the region from  $720 \text{ cm}^{-1}$  to  $800 \text{ cm}^{-1}$ , where the second sample has one (small) additional peak Q. In both spectra, the phonon ‘O’ was not clearly observed whereas in spectrum measured by others<sup>82</sup> the peak at phonon ‘O’ was more pronounced.

In the case of electro-reflectance spectra, both Samples #1 and #2 have qualitatively and quantitatively similar spectra. Even more than for the transverse polarization, the phonon features dominate the spectra. While, as for the transverse polarization, it is difficult to associate the features in the electro-reflectance spectrum unambiguously with particular phonon changes, the electro-reflectance features can generally be associated with frequency or linewidth changes varying from  $\sim 0.01 \text{ cm}^{-1}$  to  $0.2 \text{ cm}^{-1}$  or oscillator strength changes varying from  $< 0.1\%$  to  $> 1\%$  using Equation 3.7. The largest changes are associated with phonon O for Sample #1; however, they were calculated with the (questionable) assumption that the large peak in  $\Delta R/R$  at  $695 \text{ cm}^{-1}$  is associated with the tiny reflectance peak at  $705 \text{ cm}^{-1}$ <sup>82</sup> rather than the much larger Fano resonance at  $660 \text{ cm}^{-1}$ .

Away from the phonon lines, e.g. at frequencies above  $1000 \text{ cm}^{-1}$ , the electro-reflectance signal has opposite signs for the two polarizations (compare Figure 3.7b and Figure 3.11b or Figure 3.12b), and the magnitude for the transverse polarization is an order of magnitude larger than for the parallel. These differences can be understood in terms of the effects of changes in quasiparticle density on the reflectance. For example, in a Drude model of excited quasiparticles, a decrease in density (such as occurs near the

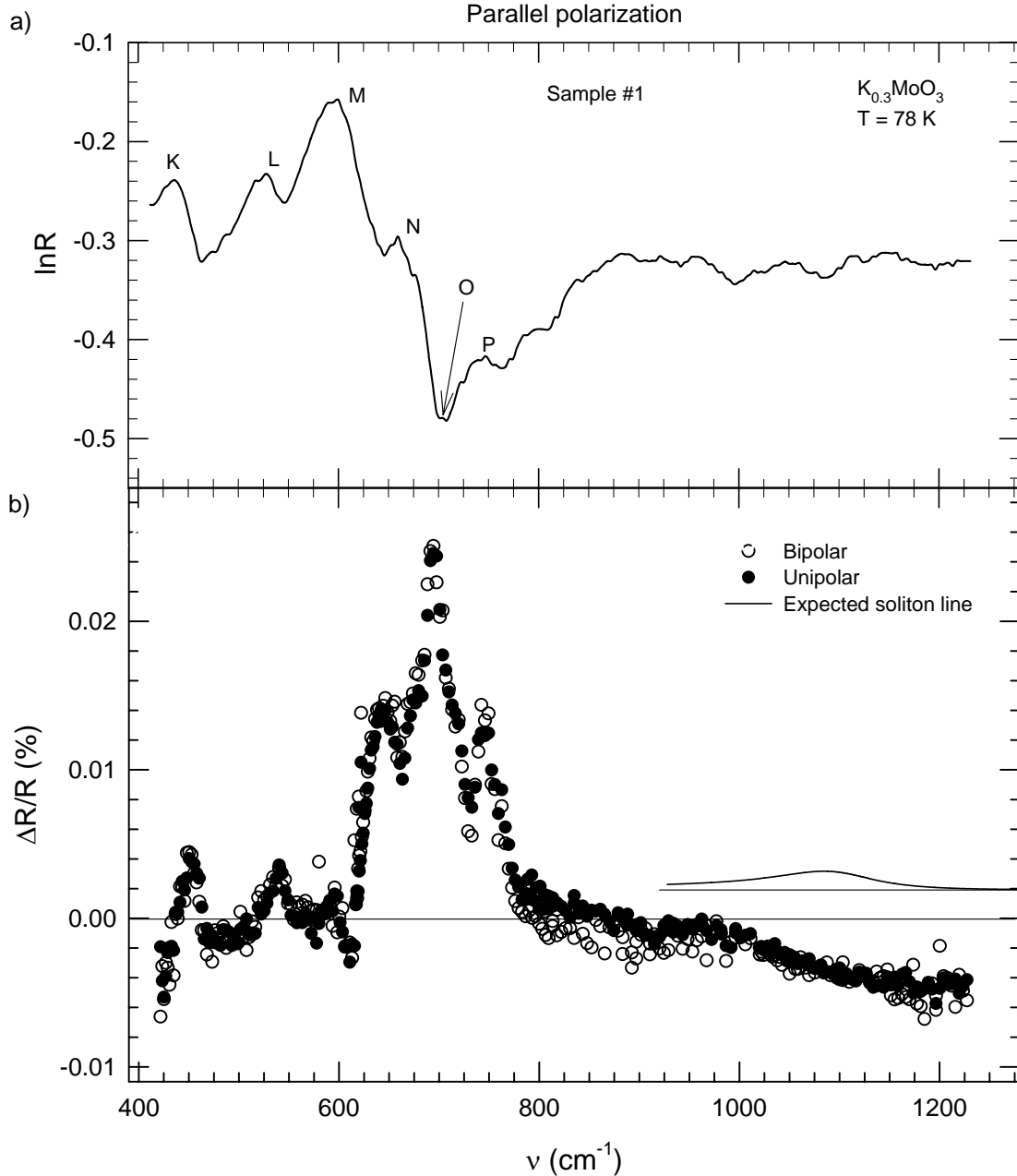


Figure 3.11 (a) Reflectivity spectrum for parallel polarization. Phonon resonances are labeled K – P. (b) Electro-reflectance spectrum for parallel polarization, measured with 253 Hz, 50 mV square-waves at the locations shown in Figure 3.10. Open symbols: bipolar square-wave. Closed symbols: unipolar square-wave (multiplied by  $N \sim 1.9$ ). The curve is the calculated difference in the spectra (vertically offset for clarity) due to the presence of field-induced soliton excitations, with  $n = 10^{16} / \text{cm}^3 \sim 1/\text{chain}$ ,  $\sigma = 400 \text{ \AA}^2$ ,  $\Gamma = 125 \text{ cm}^{-1}$ , and  $\nu = 1100 \text{ cm}^{-1}$ .

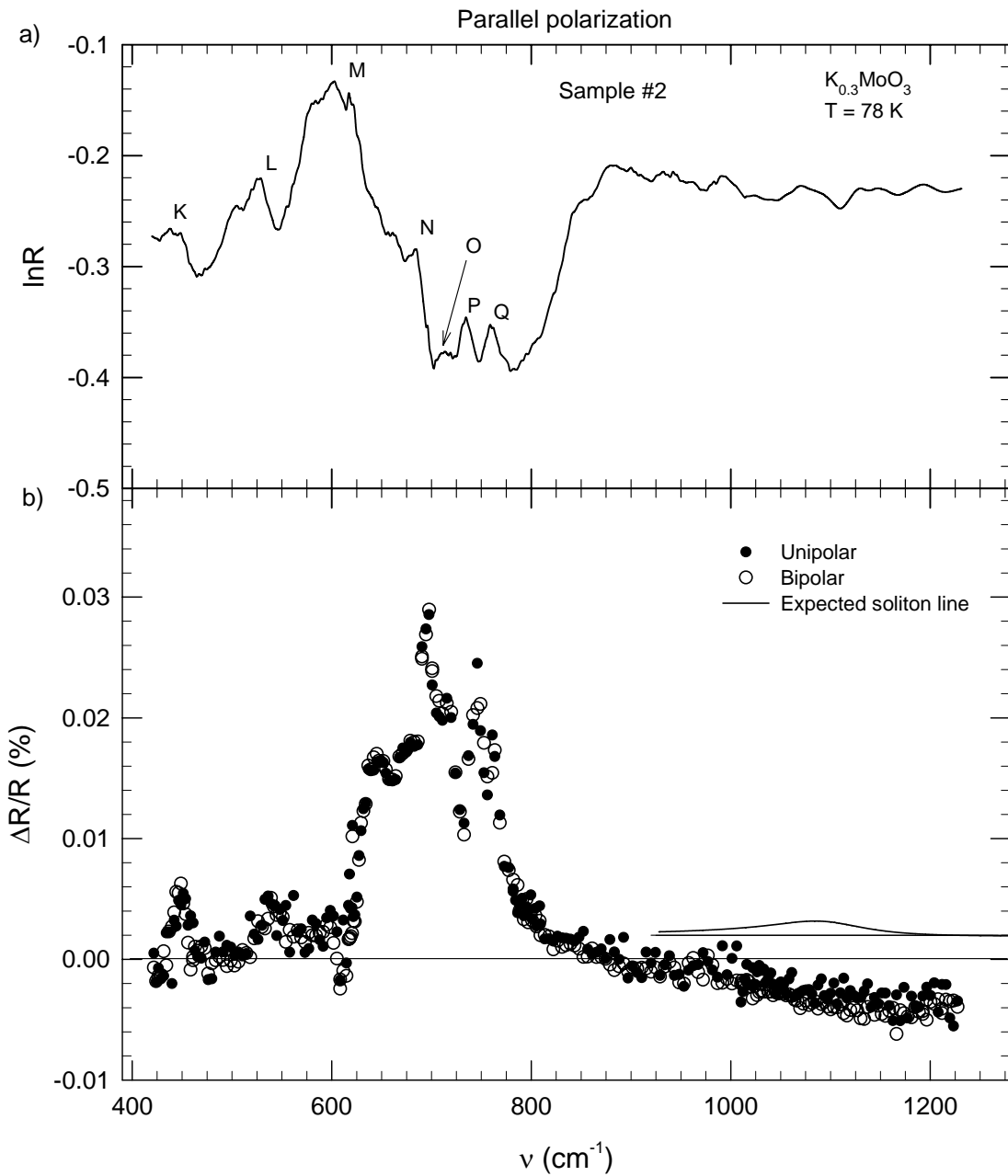


Figure 3.12 (a) Reflectivity spectrum for parallel polarization. Phonon resonances are labeled K – Q. (b) Electro-reflectance spectrum for parallel polarization, measured with 253 Hz, 50 mV square-waves for Sample #2. Open symbols: bipolar square-wave. Closed symbols: unipolar square-wave (multiplied by  $N \sim 2.1$ ). The curve is the calculated difference in the spectra (vertically offset for clarity) due to the presence of field-induced soliton excitations, with  $n = 10^{16}/\text{cm}^3 \sim 1/\text{chain}$ ,  $\sigma = 400 \text{ \AA}^2$ ,  $\Gamma = 125 \text{ cm}^{-1}$ , and  $\nu = 1100 \text{ cm}^{-1}$ .

positive contact) will decrease the imaginary part of the dielectric constant but increase the real part. For moderately anisotropic quasiparticle masses and moderate degrees of damping, this can result in an increase in the transverse reflectance and a much smaller decrease in the (higher) parallel reflectance, as observed. However, a more complete analysis of the reflectance spectra than has been attempted until now would be necessary to confirm this explanation.

As seen in the figure, the contact and bulk spectra are very similar, with no new absorption lines seen in the contact spectrum. The expected difference in the two spectra due to the presence of intragap solitons in the contact region is (see Equation 20 in Appendix B) <sup>84</sup>:

$$\delta |\Delta R/R| \sim (n\sigma/\Gamma) (e^2/\hbar c) a(\varepsilon) \quad (3.10)$$

where the geometric cross-section  $\sigma \sim \xi_{\parallel}^2 \approx 400 \text{ \AA}^2$  for parallel polarized light and the function  $a(\varepsilon) \sim 4 \times 10^{-4}$  for blue bronze.<sup>84</sup> Over most of the spectrum, the contact and bulk spectra agree to within their scatter:  $\delta(\Delta R/R) < 2.6 \times 10^{-6}$ , so that,  $[n\sigma/\Gamma] < 9 \times 10^{-9} /(\text{\AA cm}^{-1})$ . Obtaining a better limit would require having a more stable optical source.

The scatter in the data is somewhat larger near  $900 \text{ cm}^{-1}$ , and the apparent difference between the contact and bulk spectra shown in Figure 3.11b,  $\delta(\Delta R/R) \sim 7.5 \times 10^{-6}$  in this region is not reproducible so that,  $[n\sigma/\Gamma] < 2.6 \times 10^{-8} (\text{\AA cm}^{-1})$  for energies between  $800$  and  $1000 \text{ cm}^{-1}$ . The increased noise in this spectral region near the zero-crossing of  $\Delta R/R$  may reflect noise in the phase of the CDW response <sup>8</sup> because, as mentioned above, there was a small quadrature signal.

Taking the expected values of  $\Gamma \sim k_B T_C \sim 125 \text{ cm}^{-1}$ , ( $n = 10^{16}/\text{cm}^3 \sim 1/\text{chain}$ ), and  $\sigma \sim \xi_{\parallel}^2 \approx 400 \text{ \AA}^2$ , we find an upper limit for the soliton density of  $n < 3 \times 10^{15} \text{ cm}^{-3}$  for most of the spectrum, with the upper limit a few times greater than this near  $900 \text{ cm}^{-1}$ . While this limit is a few times greater than we obtained from the electro-transmission,

our estimate for the cross-section is probably more appropriate for the parallel polarization, as discussed above. These intragap states are expected to be distributed throughout the phase-slip regions of length  $\Lambda \sim 0.1$  mm near the contacts, i.e. where the unipolar electromodulated response is observed. Taking the area/conducting chain to be  $\Omega \sim 100 \text{ \AA}^2$ , our results imply that, for energies over most of the subgap spectrum, less than 30% of the conducting chains contain such an intragap state. (Given the many approximations made, these of course should just be considered order of magnitude estimates, but our results certainly imply that there is less than one intragap state per chain.) For comparison, the change in electro-reflectance that would result from one soliton per conducting chain, assuming a Lorentzian peak<sup>84</sup> in the dielectric constant (arbitrarily placed at  $1100 \text{ cm}^{-1}$ ), is shown in Figure 3.11b and Figure 3.12b.

In fact, the following simple model suggests that there should be roughly one soliton/chain. Two electrons, which form a  $2\pi$ -soliton, enter each conducting chain at the rate given by the narrow-band-noise frequency.<sup>84</sup> (This washboard, “narrow-band-noise”<sup>6</sup> period was  $\sim 5 \text{ \mu s}$  at  $V = 50 \text{ mV}$  in our samples.) The density of these  $2\pi$ -solitons in the phase-slip region ( $\Lambda$ ) is given by<sup>84</sup>

$$n = f_{NBN} T_0 / (\Lambda \Omega) \quad (3.11)$$

where  $\Omega$  is the area/chain and  $T_0$  is the “lifetime” for which the intragap state (i.e.  $2\pi$ -solitons) can be optically excited. Hence our result implies that lifetime is less than the narrow-band-noise period, whereas we expect  $T_0 \geq 1/f_{NBN}$ .

We assume<sup>84</sup> that the soliton moves off its original chain when a second soliton enters the chain. When this happens, one possibility is that the intragap states become optically inert as the soliton moved into a phase dislocation. In this case, the lifetime of the soliton would be  $T_0 = 1/f_{NBN}$ ; giving one soliton/chain. A second possibility is that the intragap states remain optically excitable within the dislocation as it moves



through the crystal of thickness  $d$ , then  $T_0 = d/(\Omega^{1/2} f_{NBN})$ , and the density of the intragap states is given by

$$n \approx (d/\Omega^{1/2})/(\Lambda\Omega) \quad (3.12)$$

In this case the density of the intragap states would be orders of magnitude larger than the first case. In either case, we would be able to observe the soliton line, although it would be only slightly greater than our noise for the first case.

In contrast, we note that in their early work on CDW phase slip, Ong and Maki<sup>75</sup> assumed that the each phase dislocation line swept through the entire sample cross-section in the narrow-band-noise period, so that the dislocation line speed would be much faster than our assumed value and dependent on the sample dimensions. In that case,  $T_0 = 1/f_{NBN}$  if the intragap states are excitable for the whole lifetime of the dislocation line, but  $T_0 = \Omega^{1/2}/(f_{NBN} d)$  if the intragap state becomes optically inert once the solitons on neighboring chains coalesce into CDW phase dislocations.<sup>84</sup> In the second case the soliton density would be negligible.

### 3.2.4 Conclusion

In conclusion, we present the first evidence that the infrared reflectance of blue bronze varies with position when a voltage above the CDW depinning threshold is applied, as expected from the previous transmission measurements. The spatial dependence of the electro-reflectance differs from that of the electro-transmission, suggesting that the dynamics of pinning on the surface is different than in the bulk. The electro-reflectance spectrum was fit assuming changes in background dielectric constant of  $\sim 0.05\%$  and/or oscillator strength and/or frequency shifts of the phonon of  $\sim 0.05\%$  and  $\sim 0.005\text{ cm}^{-1}$ . As for the transverse polarization, we find that parallel polarized phonons are affected by CDW strain, and these changes dominate the electro-reflectance spectrum. We compared the parallel polarized contact and bulk spectra to search for

intragap states associated with CDW current injection and find an upper limit for  $[n\sigma/\Gamma]$  a few times of magnitude lower than its expected value over most of the spectral range, suggesting that such states occur on less than 30 % of the conducting chains.

### 3.3 Dynamics of the Electro-Reflective Response of TaS<sub>3</sub>

When a voltage greater than its depinning threshold is applied, the CDW can slide through the sample, carrying current <sup>6</sup>, as discussed in Section 1.2. At the same time, the CDW becomes elastically strained; i.e. its phase varies throughout the sample so that the CDW is compressed near one current contact and rarefied at the other. <sup>25, 53, 55</sup> The strain ( $Q^{-1} \partial\phi/\partial x$ ) near a current contact is required to drive the phase-slip process needed for current conversion, while the smaller strain near the center of the sample reflects the shift in the chemical potential due to imperfect screening by the uncondensed quasiparticles. <sup>55</sup> The latter polarization can be frozen into sample for long times when the current is removed, as its relaxation requires the climb of CDW phase dislocations. <sup>55</sup> Studies of the dynamics of CDW polarization from an unpolarized state <sup>85</sup> have hence been hindered by this metastable behavior in the pinned state.

On the other hand, if the applied voltage is reversed above threshold, the CDW strain also (approximately) reverses <sup>53, 80</sup> and the CDW changes between two states of dynamic equilibrium. Hence, transport measurements with an ac amplitude larger than threshold could, in principle, be used to study the dynamics of CDW “repolarization”. In NbSe<sub>3</sub>, which stays metallic in its CDW state, <sup>6</sup> this repolarization time was found to be surprisingly long ( $\sim 10 \mu\text{s}$ ) <sup>53</sup>, giving rise to inductive behavior at frequencies  $\sim 1 \text{ MHz}$ . <sup>86</sup> Longer times are expected in semiconducting CDW materials, but we are not aware of any such measurements. However, in semiconducting blue bronze, K<sub>0.3</sub>MoO<sub>3</sub>, <sup>6</sup> the initial CDW polarization (i.e. from an unpolarized state) was found to obey a stretched exponential time dependence; the characteristic polarization time, presumably  $\sim 50\%$  of the repolarization time, was found to be an activated function of voltage,  $\tau \propto \exp(V_0/V)$ , with a typical time constant  $\sim 0.1 \text{ ms}$  for temperatures near 80 K and

voltages slightly above threshold.<sup>85</sup>

In measurements of the infrared transmittance of blue bronze, it was reported that, for photon energies below the CDW gap, the transmittance<sup>25</sup> varied spatially in a sample when a voltage above threshold is applied (as reviewed in Section 1.7). The spatial dependence suggested that the relative change in transmittance was proportional to the CDW strain. Hence if an alternating square wave voltage,  $\pm V(\Omega)$  was applied to the sample, the frequency ( $\Omega$ ), voltage, and position dependence of the CDW repolarization could be studied through measurement of changes in the optical properties. Indeed, the characteristic repolarization time reported in Reference,<sup>25</sup>  $\sim 0.1$  ms was similar to the pristine polarization time observed in Reference<sup>85</sup>, but detailed measurements of the frequency dependence of the electro-transmittance of blue bronze were not made.

In this section, we discuss the electro-reflectance of the related semiconducting CDW compound, orthorhombic TaS<sub>3</sub>,<sup>4</sup> this is the first report of a position/voltage dependent change in the optical properties of this material.<sup>87</sup> We have observed that, for polarizations both parallel and transverse to the conducting chains,  $|\Delta R/R| \sim 1\%$ , an order of magnitude larger than for blue bronze, with typical time constants also a few times larger than for blue bronze.<sup>58</sup> We have studied the voltage-frequency-position dependence of the electro-reflectance signal, and, *assuming that the response is proportional to the local CDW strain*, discuss its implications on the dynamics of CDW repolarization.

For these dynamics studies, the in-phase and quadrature components of the relative change in the reflectance were measured separately, requiring determination of the frequency dependence of the electronics including the detector electronics in the microscope, to which we had no direct access. In order to measure the gain and phase shift of the electronics, we needed a square wave light signal because the in-phase and quadrature components of  $\Delta R/R$  were measured with square wave voltages (to the sample) at different frequencies. We modulated the laser current with electronic circuitry

in the laser controller to produce a square wave laser signal, and its phase and magnitude were measured as functions of modulating frequency with the lock-in amplifier. However the laser controller could not vary the laser current below 100 Hz and the shape of the square wave signal became distorted above  $\sim 2000$  Hz due to modulation of the laser temperature as the period became comparable to the thermal time constant. Therefore, for frequencies below 100 Hz and above 2000 Hz, a mechanical chopper (which could go to 4000 Hz) was used. Note that the laser signal was only approximately square wave when chopped with mechanical chopper and there was a fixed phase error at all chopping frequencies that depended on the position of the chopper. This fixed phase error was determined by comparing the phases measured with two techniques between 100 Hz and  $\sim 1000$  Hz. From this comparison, we could only determine the phase shift of the electronics to a precision of  $\sim 2^\circ$ ; this precision was adequate at most frequencies, but led to relatively large uncertainties in the quadrature component of the electro-reflectance signal at low frequencies (e.g.  $< 100$  Hz) where the quadrature component is much smaller than the in-phase component (e.g. see Figure 3.14).

All the measurements were made with the sample holder at  $T \sim 77$  K; the sample, in vacuum, may have been a few degrees warmer than this in general, and an additional few degrees warmer for measurement at high voltage. In principle, since measurements were made with symmetric square wave voltages, there should not have been an oscillating signal due to Joule heating of the sample, but CDW materials often have slightly unequal responses to positive and negative currents, so there may have been a small thermal signal for frequencies below the thermal response rate ( $\sim 100$  Hz). However, since the electro-reflectance response for bipolar square waves was always much larger than we observed for unipolar square waves (e.g. see Section 3.2.1 for similar results in blue bronze), the thermal component to the signals is considered negligible.

Although samples were chosen for having visually flat surfaces, we typically found that the reflectance signal varied considerably as we scanned the light along the sample, suggesting that the reflectance was affected by unseen steps and/or facets

(perhaps causing diffraction as well as misdirecting the light). Similarly, we were not able to take meaningful spectra with our lasers. However, these effects should not affect the relative change in reflectance, as determined by Equation. 3.13. When studying a new sample, we first scanned the spectrum for wavelengths at which the electro-reflectance could be measured with a high signal/noise ratio. (As discussed in Section 2.5.2, there was considerable, variable noise due to mechanical vibrations of the helium refrigerator for cooling the lasers). Dynamics studies were done on six samples, but in this thesis, I will concentrate on two samples which were mounted over holes on the sapphire substrate, as discussed in Section 2.4. The light spot was focused to a spot  $\sim 50$   $\mu\text{m}$  long along the length of the sample and slightly wider than the sample; light that missed the sides of the crystal went into the hole in the substrate and therefore was not reflected back to the detector. Measurements were made for both parallel and transverse polarized light and are presented in the sections below; no significant differences were observed for the two polarizations.

### 3.3.1 Voltage and Spatial Dependences of the Electro-Reflectance

Figure 3.13a shows the square-wave voltage dependence at  $\Omega/2\pi = 253$  Hz of  $\Delta R/R$  for Sample #1, measured with (parallel polarized) light of energy  $\nu = 860$   $\text{cm}^{-1}$  focused adjacent to a current contact. (Note, as indicated by the minus sign on the ordinate that at this wavelength the reflectance decreases near the positive contact.) As discussed above, the onset voltage of the electro-optical signal,  $V_{\text{onset}} = 40$  mV, is presumably the threshold at which the CDW becomes depinned within the crystal<sup>8</sup>, while the threshold for non-linear current is higher (i.e.  $V_T = 70$  mV), and is the voltage at which the CDW is depinned at the contacts; the difference is the “phase-slip voltage”.<sup>53, 80</sup> The (dc) threshold voltages for ortho-TaS<sub>3</sub> samples from two different batches with typical length of 1 mm varied from  $\sim 27$  mV to  $\sim 100$  mV.

The spatial dependences at 253 Hz for a few voltages are shown in Figure 3.13b. Note that, unlike for blue bronze, the spatial profile is very asymmetric, with the response much larger on one side of the sample. Note that in Figure 3.13b the electro-reflectance

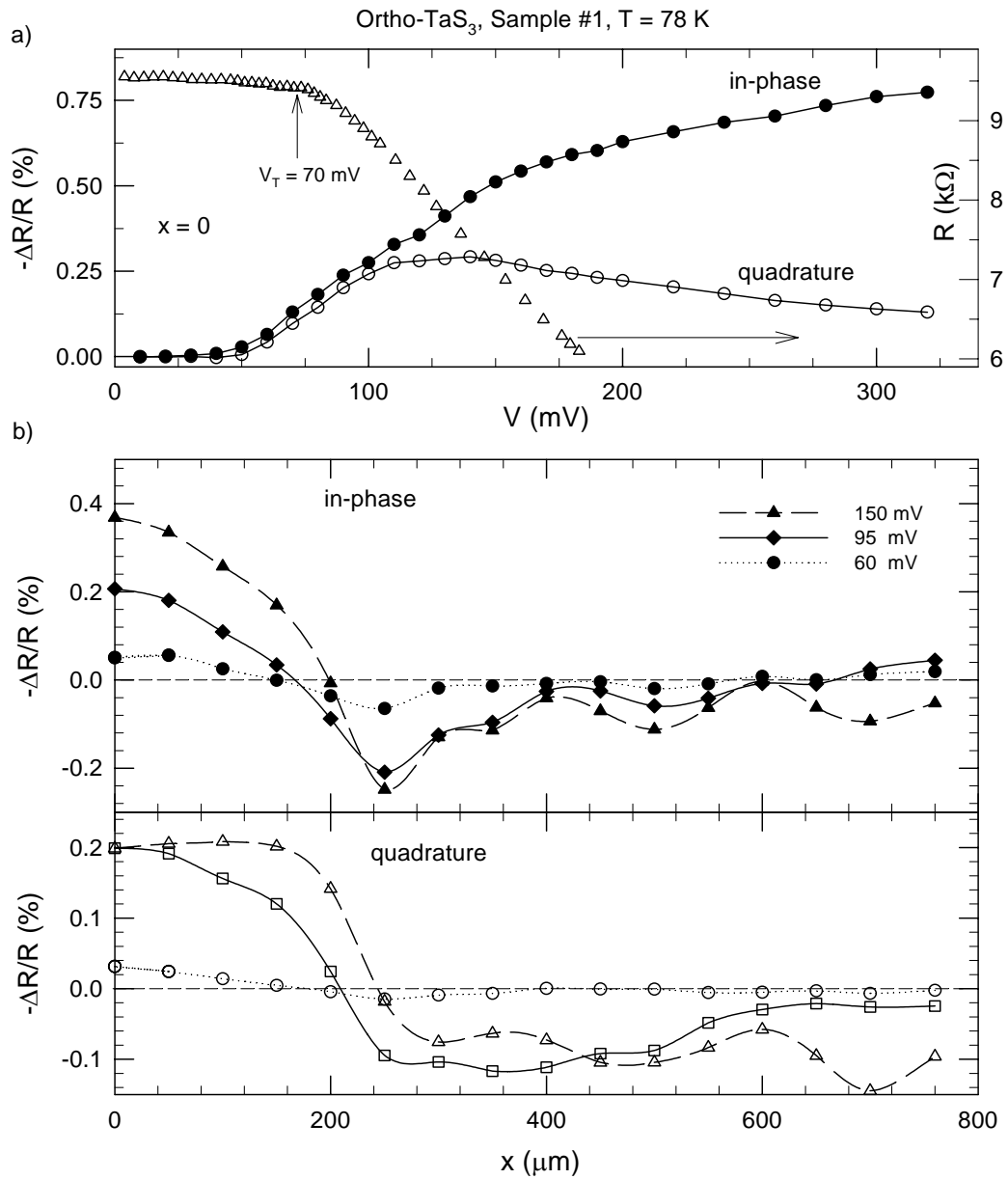


Figure 3.13 (a) Voltage dependence of the electro-reflectance at the left contact and the dc R-V curve. (b) Spatial dependence of the in-phase and quadrature response of the electro-reflectance ( $\Delta R/R$ ) to 253 Hz square waves of magnitudes 60, 95, and 150 mV for Sample #1 with light of energy  $\nu = 860$  cm<sup>-1</sup>. The right ( $x \sim 800$   $\mu\text{m}$ ) contact is grounded and the voltage applied to the left ( $x \sim 0$ ) contact, so that (noting the minus sign on the ordinate) the electro-reflectance decreases for large voltages on the side of the sample which is positive.

signal is a very irregular function of position on the side of the sample (i.e. for  $x > 250 \mu\text{m}$ ), and even again changes sign near the  $x \sim 800 \mu\text{m}$  contact for small voltages; this inversion is similar to what is observed for blue bronze,<sup>58</sup> as shown in Figure 3.6. Similar voltage and spatial profiles, with no qualitative differences, were observed with different wavelengths for both polarizations of light.

While similar asymmetry was observed for all six samples studied, for one sample (Sample #3) the response was quite symmetric on its initial cool down and only became asymmetric with subsequent coolings, as shown in Figure 3.14 for two different runs. The reason for this change may be due to deterioration of the contacts with subsequent coolings. While the spatial profile of  $\Delta R/R$  was different on two runs for this sample, the (asymmetric) spatial profiles (in most of the cases) were very reproducible for the other 5 samples. Asymmetric spatial profiles suggest that the CDW polarization, either because of differences in the electrical contacts or defects in the sample, tends to pile up on one side of the sample.

### 3.3.2 Frequency Dependence of the Electro-Reflective Response

Figure 3.15 and 3.16 show the frequency dependences at  $x = 0$  and  $100 \mu\text{m}$  for Sample #1 at a few voltages, for frequencies between 25 Hz and 4 kHz. (Actual measurements were made for several voltages but only 4 voltages are shown for clarity). As expected, the average relaxation time, estimated from the reciprocal of the frequency of the peak in the quadrature response (and shoulder in the in-phase response) decreases as the voltage increases.<sup>85</sup> An unexpected feature, however, is that the in-phase response becomes inverted for frequencies greater than  $\sim 1$  kHz, indicative of surprisingly large inertia to repolarization. In contrast, the inductive response in  $\text{NbSe}_3$ , corresponding to the inverted in-phase response, was only observed for frequencies near 1 MHz.<sup>86</sup> The curves show fits to the modified damped oscillator equation:

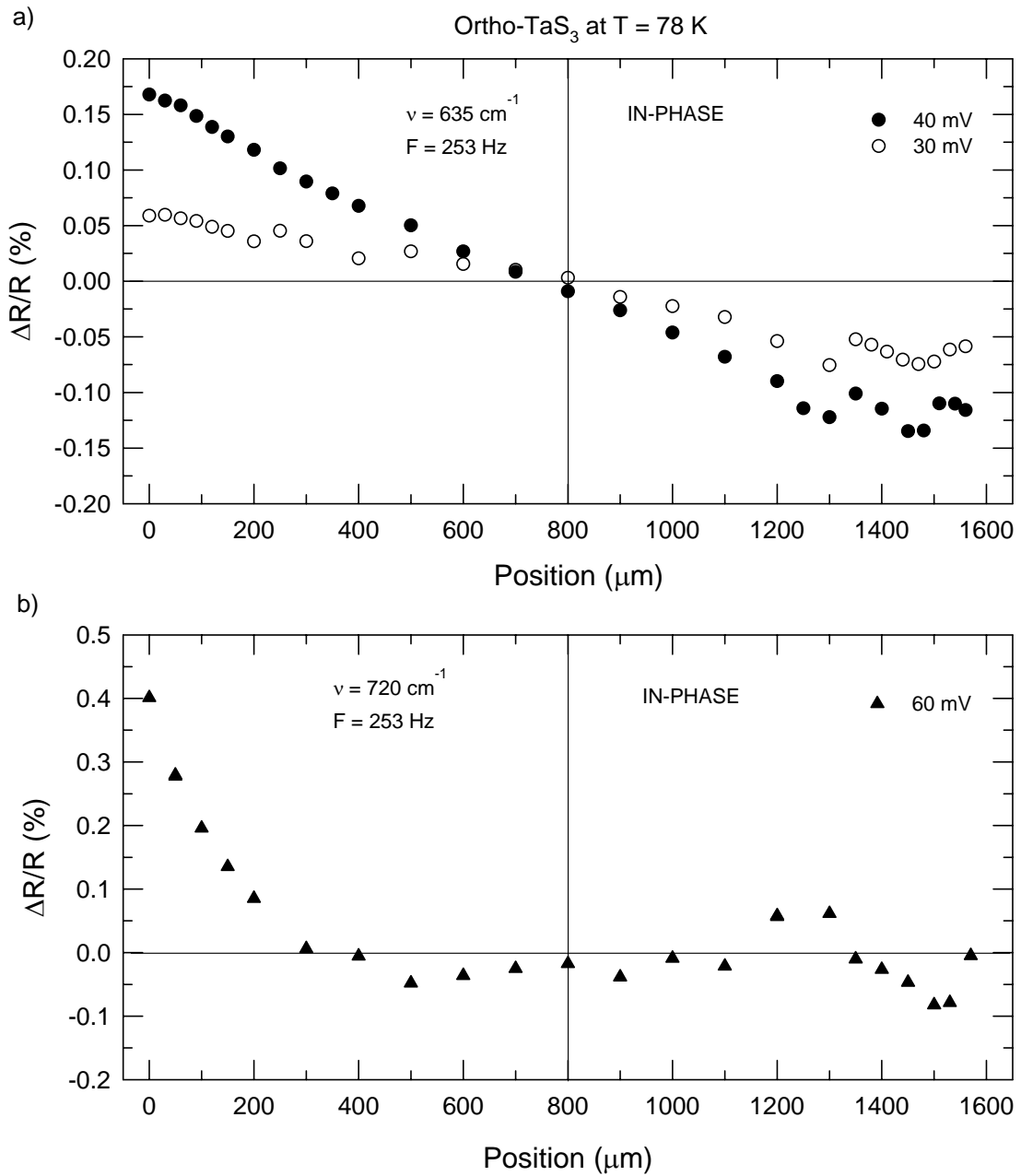


Figure 3.14 Spatial dependence of the in-phase response of  $\Delta R/R$  for Sample #3 in two different coolings: (a) Square waves of magnitude 30 mV and 40 mV at 253 Hz in the first cooling. (b) Square wave of magnitude 60 mV at 253 Hz in a later cooling.



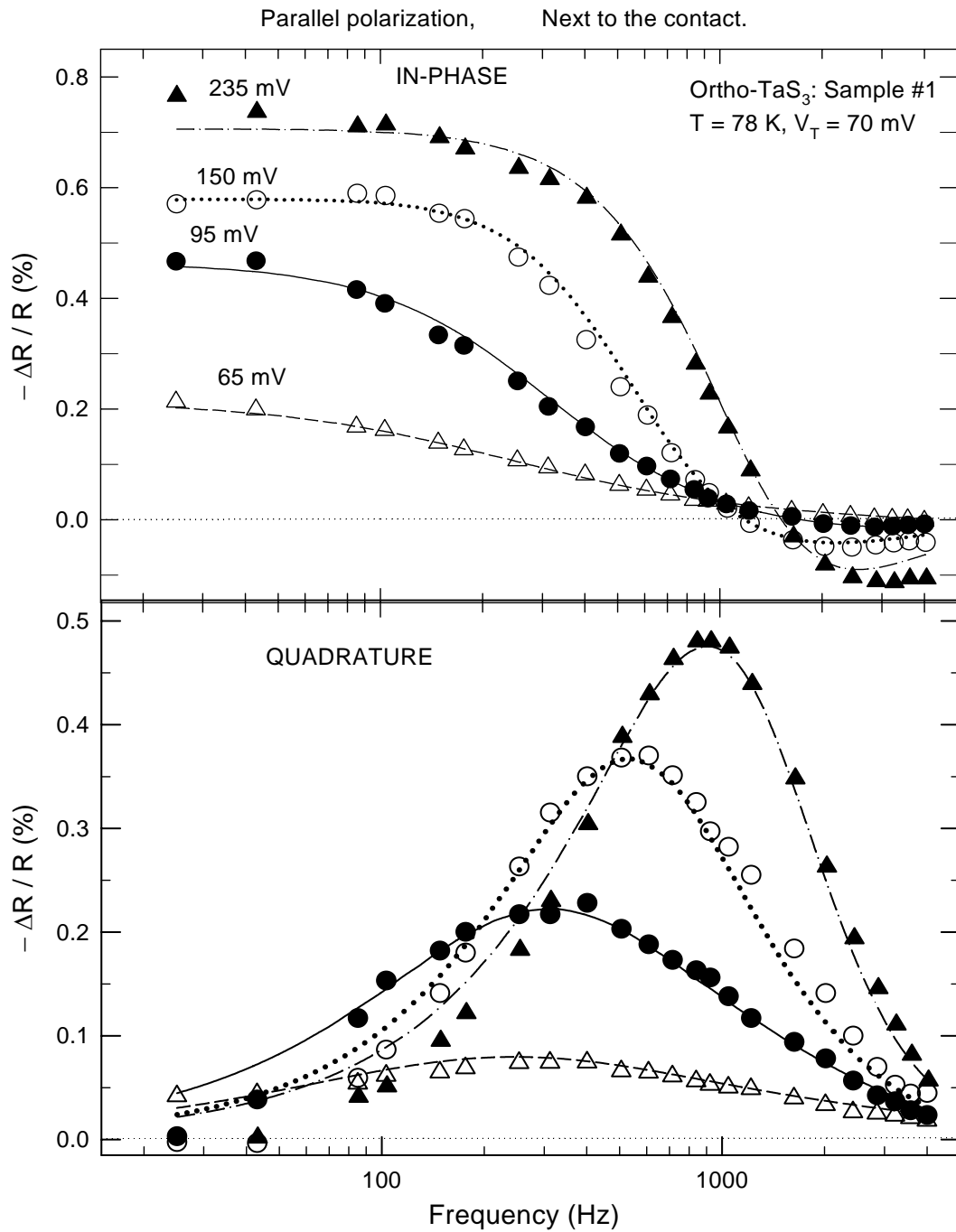


Figure 3.15 Frequency dependence of the in-phase (upper panel) and quadrature (lower panel) electro-reflectance for 65 mV, 95 mV, 150 mV, and 235 mV square waves for Sample #1, with light ( $\nu = 860 \text{ cm}^{-1}$ , parallel polarization) incident adjacent to the left contact (see Figure 3.13). The curves show fits to Equation. 3.13.

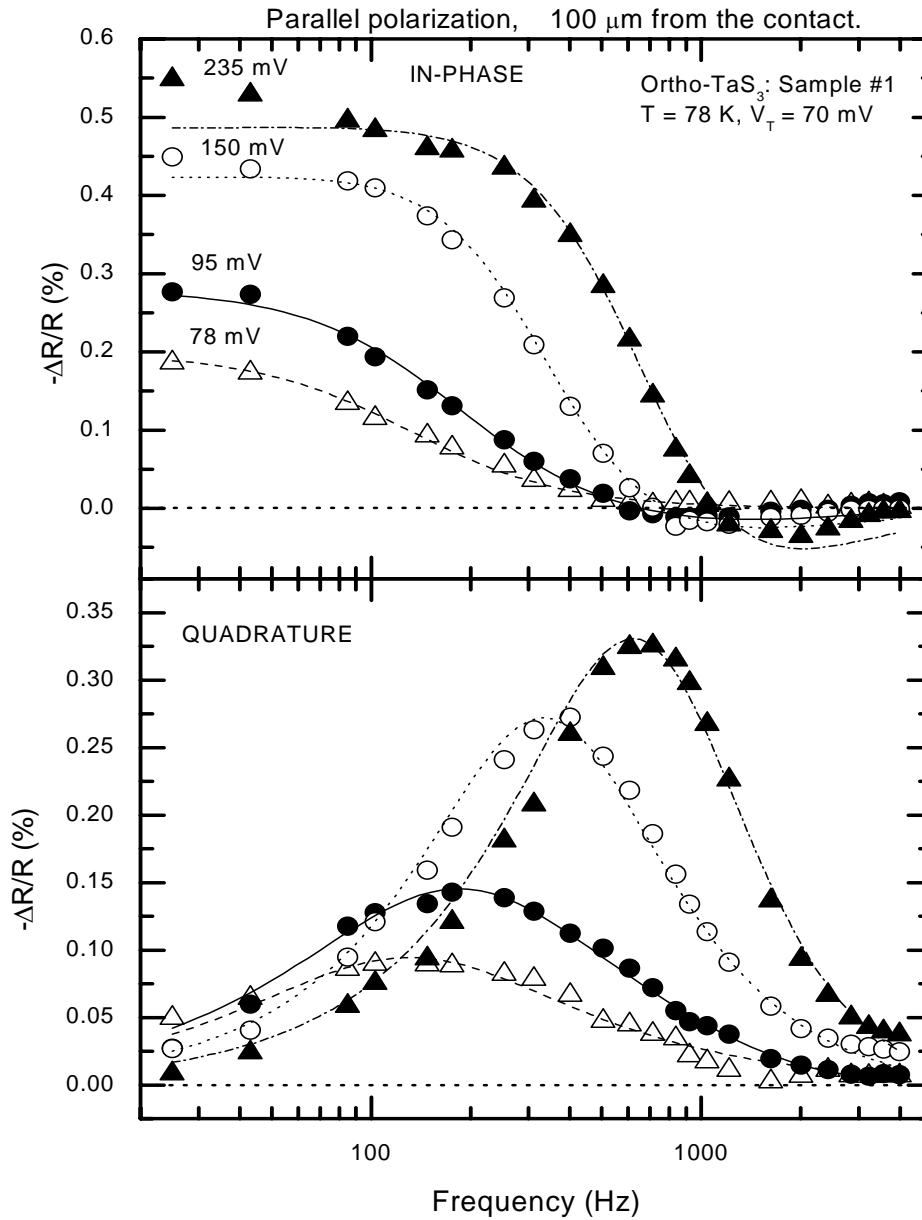


Figure 3.16 Frequency dependence of the in-phase (upper panel) and quadrature (lower panel) electro-reflectance for 78 mV, 95 mV, 150 mV, and 235 mV square waves for Sample #1, with light ( $\nu = 860 \text{ cm}^{-1}$ , parallel polarization) incident at  $100 \text{ }\mu\text{m}$  from the left contact (see Figure 3.13). The curves show fits to Equation. 3.13.

$$\frac{\Delta R}{R} = \frac{\left(\frac{\Delta R}{R}\right)_0}{\left[1 - \frac{\Omega^2}{\Omega_0^2} + (-i\Omega\tau_0)^\gamma\right]} \quad (3.13)$$

where  $\left(\frac{\Delta R}{R}\right)_0$  is the amplitude of the electro-reflectance signal,  $\Omega_0 / 2\pi$  is the resonance frequency,  $\tau_0$  is the relaxation time, and  $\gamma$  is the exponent for distribution of relaxation times. Real and imaginary parts of  $\Delta R/R$  are written as

$$\text{Re}\left(\frac{\Delta R}{R}\right) = \left(\frac{\Delta R}{R}\right)_0 \frac{1 - \frac{\Omega^2}{\Omega_0^2} + (\Omega\tau_0)^\gamma \cos(\gamma\pi/2)}{\left[\left(1 - \frac{\Omega^2}{\Omega_0^2}\right)^2 + 2(\Omega\tau_0)^\gamma \left(1 - \frac{\Omega^2}{\Omega_0^2}\right) \cos(\gamma\pi/2) + (i\Omega\tau_0)^{2\gamma}\right]} \quad (3.14)$$

$$\text{Im}\left(\frac{\Delta R}{R}\right) = \left(\frac{\Delta R}{R}\right)_0 \frac{(\Omega\tau_0)^\gamma \sin(\gamma\pi/2)}{\left[\left(1 - \frac{\Omega^2}{\Omega_0^2}\right)^2 + 2(\Omega\tau_0)^\gamma \left(1 - \frac{\Omega^2}{\Omega_0^2}\right) \cos(\gamma\pi/2) + (i\Omega\tau_0)^{2\gamma}\right]} \quad (3.15)$$

In analogy to the Cole-Cole generalization of simple relaxation,<sup>88</sup> we've introduced the exponent  $\gamma$ ; values of  $\gamma < 1$  imply a distribution of relaxation times.<sup>89</sup>

Several similar frequency dependences of the in-phase and quadrature electro-reflectance response for different square wave voltages for Samples #1 and #2, at different wavelength and polarization are shown in Figures 3.17-3.19. (Note that for some wavelengths/polarizations, as for the case shown in Figures 3.15-3.16 the (low frequency) reflectance decreases at the positive side of the sample, so  $\Delta R/R < 0$ , while at other wavelengths/polarizations it increases, so  $\Delta R/R > 0$ .) From all these figures, we found that the average relaxation times for both samples became faster as the

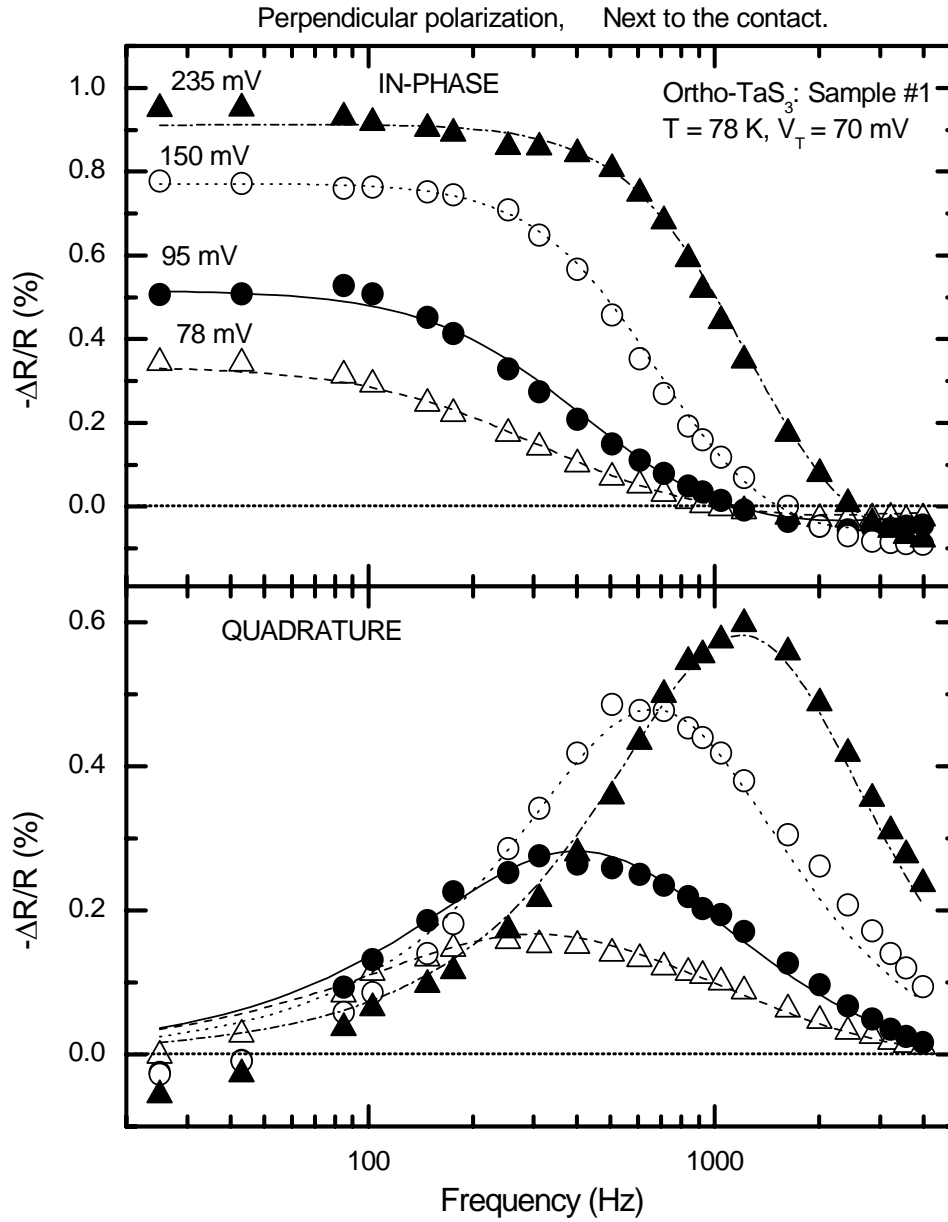


Figure 3.17 Frequency dependence of the in-phase (upper panel) and quadrature (lower panel) electro-reflectance for 78 mV, 95 mV, 150 mV, and 235 mV square waves for Sample #1, with light ( $\nu = 760 \text{ cm}^{-1}$ , perpendicular polarization) incident adjacent to the left contact (see Figure 3.13). The curves show fits to Equation 3.13.

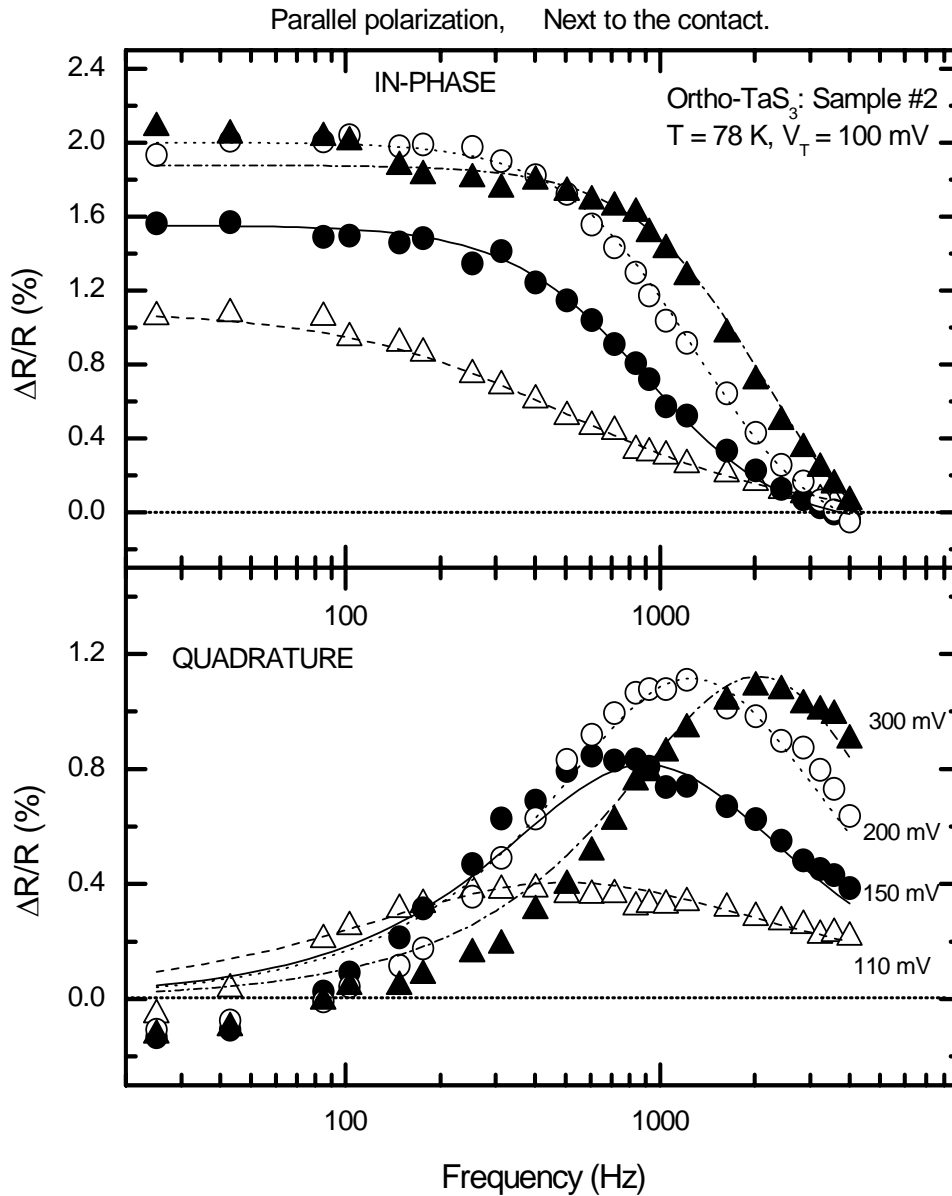


Figure 3.18 Frequency dependence of the in-phase (upper panel) and quadrature (lower panel) electro-reflectance for 110 mV, 150 mV, 200 mV, and 300 mV square waves for Sample #2, with light ( $\nu = 695 \text{ cm}^{-1}$ , parallel polarization) incident adjacent to the contact. The curves show fits to Equation 3.13.

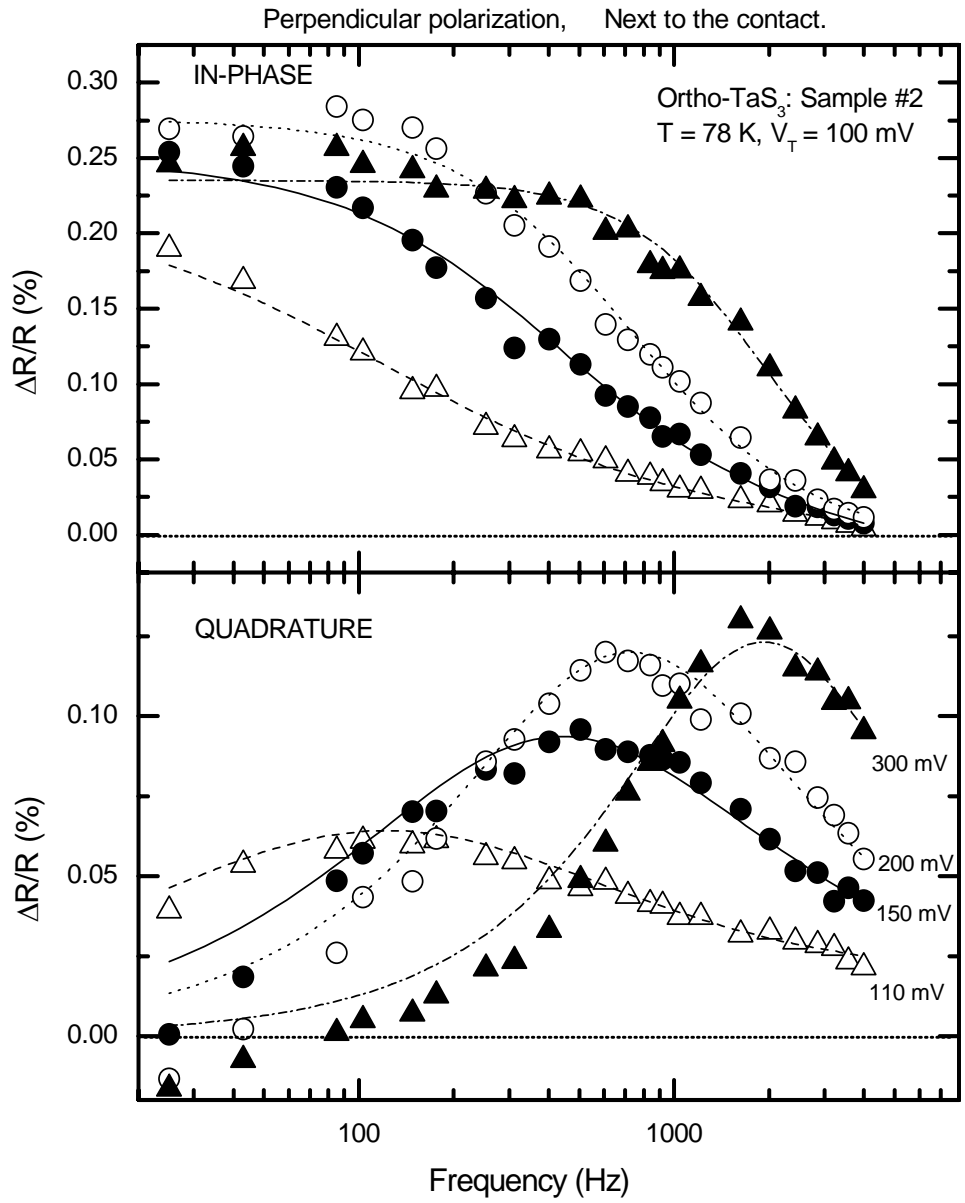


Figure 3.19 Frequency dependence of the in-phase (upper panel) and quadrature (lower panel) electro-reflectance for 110 mV, 150 mV, 200 mV, and 300 mV square waves for Sample #2, with light ( $\nu = 925 \text{ cm}^{-1}$ , perpendicular polarization) incident adjacent to the contact. The curves show fits to Equation 3.13.

voltage was increased. The inversion of the in-phase response for Sample #2 was observed at few times higher frequency than for Sample #1. These different inversion frequencies for the in-phase response for two samples imply that the inertia for repolarization is sample dependent.

The voltage dependences of the parameters of the fit, for (parallel polarized) light at two locations each for two samples, are shown in Figure 3.20. In each case,  $\tau_0 \propto V^{-p}$ , with  $1 \leq p \leq 3/2$ , much weaker than the exponential voltage dependence in blue bronze found from transport measurements mentioned above.<sup>85</sup> There is no indication of  $\tau_0$  diverging at the depinning threshold, as expected for a dynamic critical models of depinning,<sup>72</sup> but while data was taken down to the nonlinear threshold,  $V_T$ , we have not yet been able to approach the “bulk threshold”,  $V_{\text{onset}}$ . However, what is observed in most cases is that the exponent  $\gamma$  decreases at small voltages, indicating a broadening of the distribution of relaxation times. While there is no clear voltage dependence to the resonant frequency, its typical value of  $\Omega_0/2\pi \sim 1$  kHz suggests that there is  $\sim 100$   $\mu\text{s}$  delay between the applied voltage and the electro-reflective response.

For both samples, the relaxation time at  $100 \mu\text{m}$  from the contact is greater than at the contact. This is consistent with previous results<sup>25, 53</sup> and suggests that the relaxation is “local”, i.e. driven by the local CDW strain, which is greatest at the contact. In addition, except for low voltages at which the  $\tau_0$ -distribution broadens, the resonant frequency is smaller away from the contact (i.e. the inertia is greater) than at the contact.

The “repolarization” times (and inertia) are much greater than those associated with the dielectric constant, i.e. small amplitude oscillations of the CDW about its pinned position (at  $T \sim 80$  K, the dielectric time constant  $\sim 1 \mu\text{s}$ <sup>90, 91</sup>), because polarization and repolarization involve large, nonlocal changes in the CDW phase.<sup>85, 86</sup> On the other hand, the repolarization times shown in Figure 3.20 are much smaller than the time constants governing how the CDW responds to elastic strains of the crystal; the elastic time constants were measured to be  $\sim 10$  ms at  $2V_T$  and diverged at threshold.<sup>92</sup> This

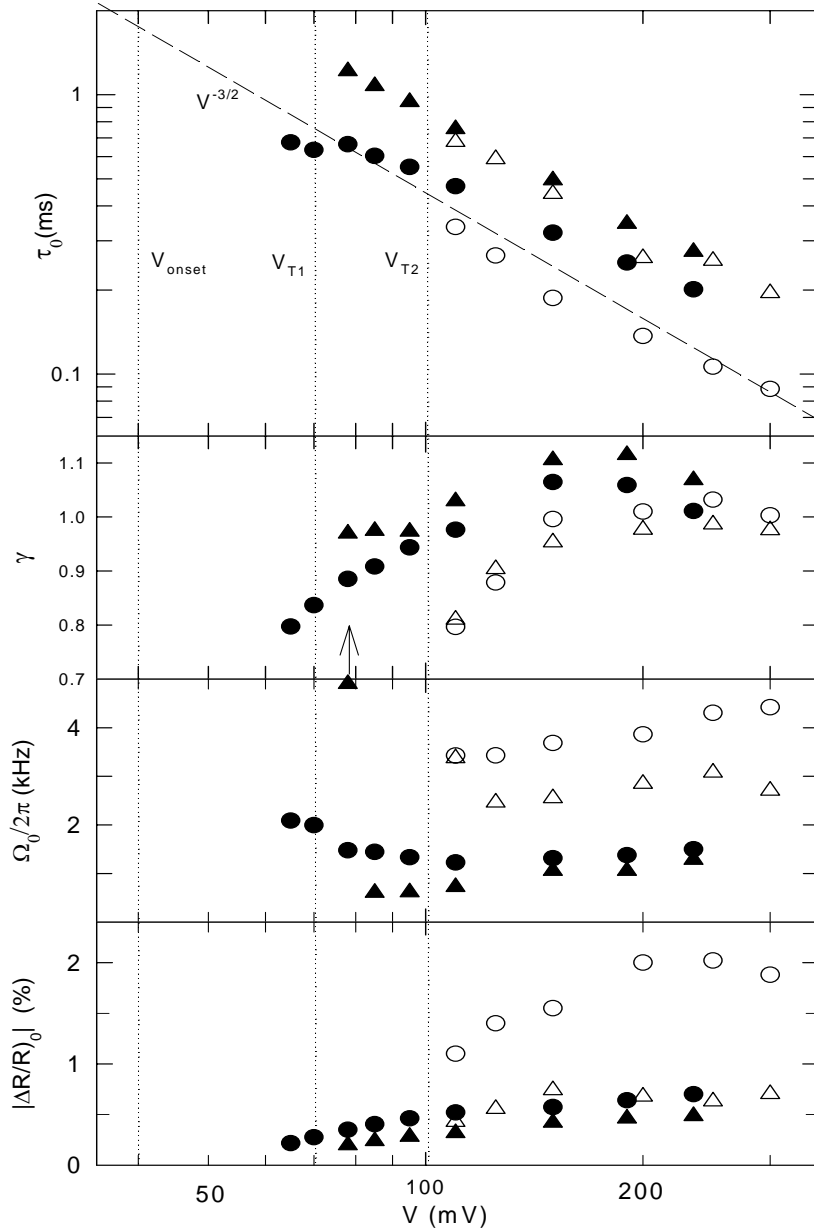


Figure 3.20 Voltage dependence of the parameters of Equations 3.15-16. Closed symbols: Sample #1 (measured at  $860 \text{ cm}^{-1}$ ); open symbols: Sample #2 (measured at  $695 \text{ cm}^{-1}$ ). Circles: light focused adjacent to current contact; triangles: light focused  $100 \mu\text{m}$  from this contact. The dotted lines show the onset voltages ( $V_{\text{onset}} \approx 40 \text{ mV}$  for both samples) and thresholds for non-linear current ( $V_T \approx 70 \text{ mV}$  for Sample #1 and  $100 \text{ mV}$  for Sample #2). The dashed line in the upper panel indicates  $\tau_0 \propto V^{-3/2}$  behavior for reference. (The symbol with the arrow indicates a fit for which the resonant frequency was effectively infinite, i.e.  $\gg 4 \text{ kHz}$ .)



difference might seem surprising, since both the repolarization and “elastic” time constants are related to long length scale deformations of the CDW. That the elastic time constant is greater therefore suggests that changes in the elastic constants caused by CDW depinning, believed to be due to the effect of the strain on the optimum local CDW phase<sup>92,93</sup>, require changes of the CDW on an even longer length scale than repolarization. Another possible reason for the difference is that the elastic measurements<sup>92</sup> averaged over the entire sample length, whereas we measured the reflectance changes near the contacts, where repolarization is fastest.

### 3.3.3 Real Time Measurement of the Electro-Reflective Response

Figure 3.21 shows direct time traces, measured with a digital oscilloscope, of the change in reflectance of Sample #1 in response to applied square wave voltages. As for Figure 3.20, measurements were made for light adjacent to the contact (center panels) and 100  $\mu\text{m}$  positions (bottom panels). Each trace in the figure represents the average of 500 time sweeps, with time normalized to the square wave period. Also shown (the top panels) is the resulting current; the current overshoot, due to CDW repolarization after reversing the voltage,<sup>6, 94</sup> is shown by arrows in the current traces. Figure 3.21a shows the responses to 253 Hz square-waves of different magnitudes. The decrease in the relaxation time with increasing voltage is clear in the  $\Delta R$  traces, but in all cases this time is much longer than the “current overshoot” time; in fact, as has been pointed out in References<sup>8, 53</sup>, the current estimated from the overshoot is only a small fraction of the repolarization current.

The center panel of Figure 3.21a shows that, when the current changes from negative to positive, the reflectance adjacent to the contact has a delay of  $\sim 100 \mu\text{s}$  before it starts changing abruptly. This is seen more clearly in Figure 3.21b, at which the responses to 200 mV square waves at different frequencies are shown. Note that away from the contact (lower panels), while there is still a comparable delay in  $\Delta R$ , the onset of the increase in reflectance is much broader (i.e. less abrupt). Also note that the delay is several times shorter when the current is changing from positive to negative. While the

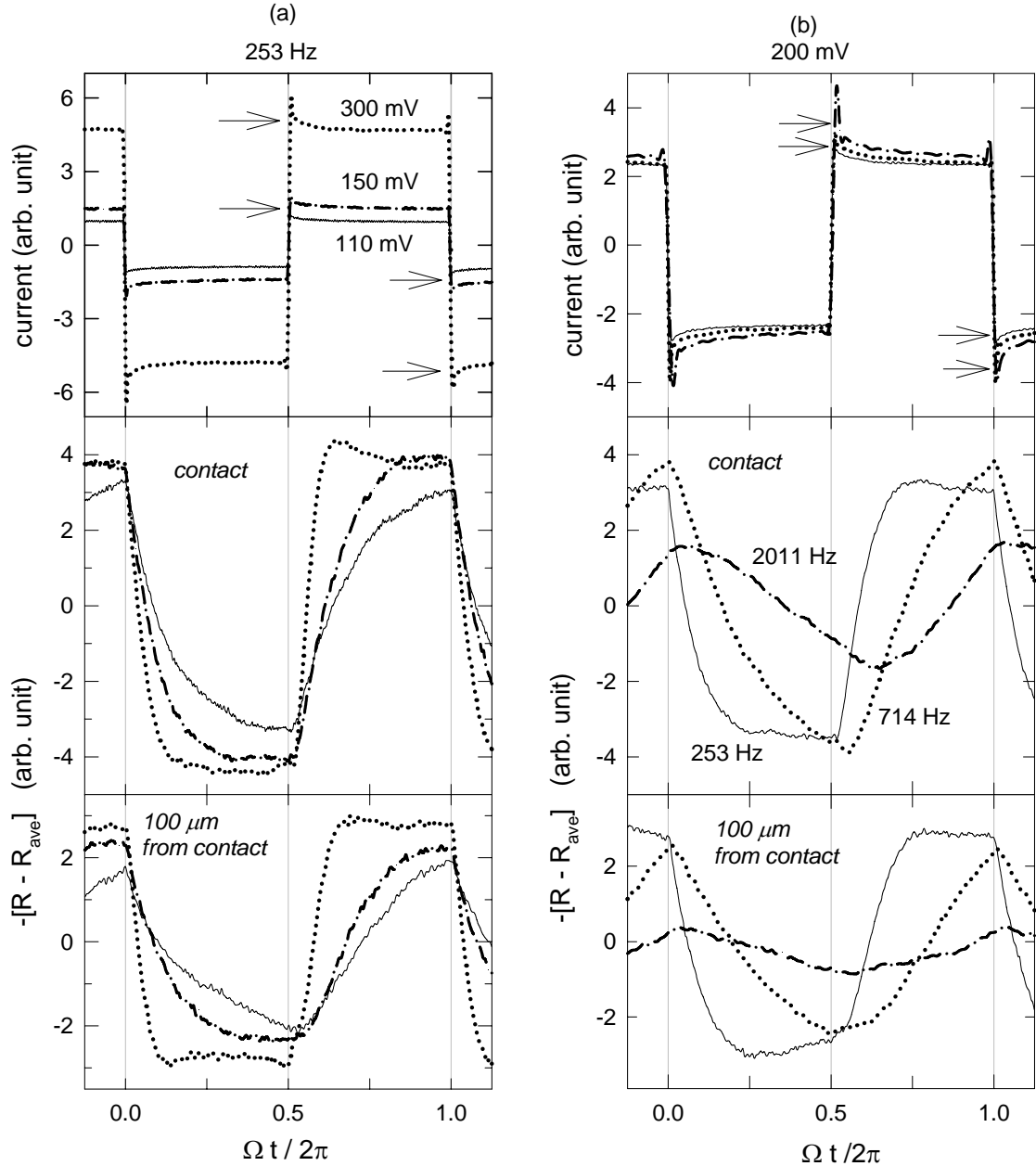


Figure 3.21 Time dependence of the CDW current (top panels), reflectance adjacent to current contacts (center panels), and reflectance 100  $\mu\text{m}$  from the contacts (bottom panels) for Sample #1 at  $\nu = 860 \text{ cm}^{-1}$ . The horizontal arrows in the top panels indicate current overshoot. (a) Responses to  $\Omega/2\pi = 253 \text{ Hz}$  square waves with magnitudes 110 mV, 150 mV, 300 mV. (b) Responses to 200 mV square waves of frequencies  $\Omega/2\pi = 253 \text{ Hz}$ , 714 Hz, and 2011 Hz.

magnitude of the CDW polarization has previously been found to be polarity dependent,<sup>54, 56</sup> for example the magnitude of the polarization has been observed to be larger on the negative side of the sample in TaS<sub>3</sub> at lower temperatures,<sup>95, 96</sup> this is the first report of different dynamic response for the two polarities. This dynamic polarity dependence suggests that Schottky barriers at the contacts may contribute to the surprisingly large inertia. If this is so, perhaps different barriers on the two contacts are responsible for the very asymmetric spatial dependence. However, since the penetration depth of light at these frequencies is  $\sim 1000 \text{ \AA}$ , such a strong contact dependence is surprising. As discussed in Section 2.4, the contacts on these samples were gold films. It would be interesting to see if different results are obtained with contacts of other materials.

In fact, the delayed response of the reflectance as compared to the current suggests that our underlying assumption, that  $\Delta R/R \propto \partial\phi/\partial x$ , may require qualification, since the current overshoot indicates that the CDW polarization is “undelayed”. The difference may reflect the fact that the reflectance and current are probing different fractions of the sample depth. (Similarly, as mentioned above, differences in the spatial dependence of the changes in transmittance and reflectance were previously noted in blue bronze.) It will therefore also be interesting to compare the time dependence of changes in transmittance with those in reflectance.

To some extent, the abrupt but delayed change in reflectance adjacent to the contact resembles the delays in CDW conduction, typically  $\sim 1 \text{ ms}$ , that have been observed in samples exhibiting “switching”, i.e. hysteretic discontinuous changes in current,<sup>97-99</sup> but the resemblance may be superficial. The switching delays were associated with the time needed for the CDW polarization to build up to the value needed for phase slip,<sup>99</sup> but in our case, with non-switching samples, no delay was observed in the current change (including the overshoot).

Our measurements suggest that the electro-optic response can be used to measure the temporal/spatial dependence of changes in CDW polarization without adding multiple

contacts, which tend to strongly perturb the local fields, especially in semiconducting CDW materials such as TaS<sub>3</sub> and blue bronze. Furthermore, once the spectrum is known, the variation of the polarization with depth in the sample can be measured by comparison of the response at different wavelengths and polarizations or, as mentioned above, by comparison of the electro-reflectance and electro-transmittance. However, we note two caveats: i) For Samples #1 and #2, the light spot filled the sample width, so that we averaged over this transverse dimension. For other samples, a narrower light spot was used and, we frequently observed large differences in  $\Delta R$  as the spot was scanned across the sample width, in some cases even changing sign. Similarly, large local changes in the chemical potential, implying local polarizations, varying across the sample width were measured with a scanning electron microscope,<sup>100</sup> presumably reflecting the sensitivity of the CDW to grain boundaries and surface features prevalent in even visually smooth samples of TaS<sub>3</sub>. ii) For some cases, the measured frequency dependence of  $\Delta R/R$  did not obey Equation. 3.13, which was introduced above simply to parameterize results for the two samples (#1 and #2) studied most extensively. In particular, in some cases high frequency inversion was not observed (i.e.  $\Omega_0/2\pi > 4$  kHz) and in others the peak in the quadrature component of  $\Delta R/R$  was much less symmetric, as shown in Figure 3.22, than given by this equation. For Sample #3, we even observed two peaks in the quadrature component of  $\Delta R/R$ , especially at low voltages, as shown in Figure 3.23. While the double peaks became less visible at higher voltages, our fitting equation can not work for low voltage data. The unusual double peaks indicate that there may be two relaxations processes taking place in a small length  $\sim 50$   $\mu\text{m}$  (light spot) of the sample.

### 3.3.4 Conclusion

In conclusion, we have presented results of measurements of the voltage, frequency, and spatial dependence of the electro-reflectance of orthorhombic TaS<sub>3</sub>. The response indicates that there is considerable inertia, which is observable as a polarity dependent delay in  $\Delta R$  in measurements of its time dependence. We have fit the frequency dependence of  $\Delta R/R$  to a modified damped harmonic oscillator response, and

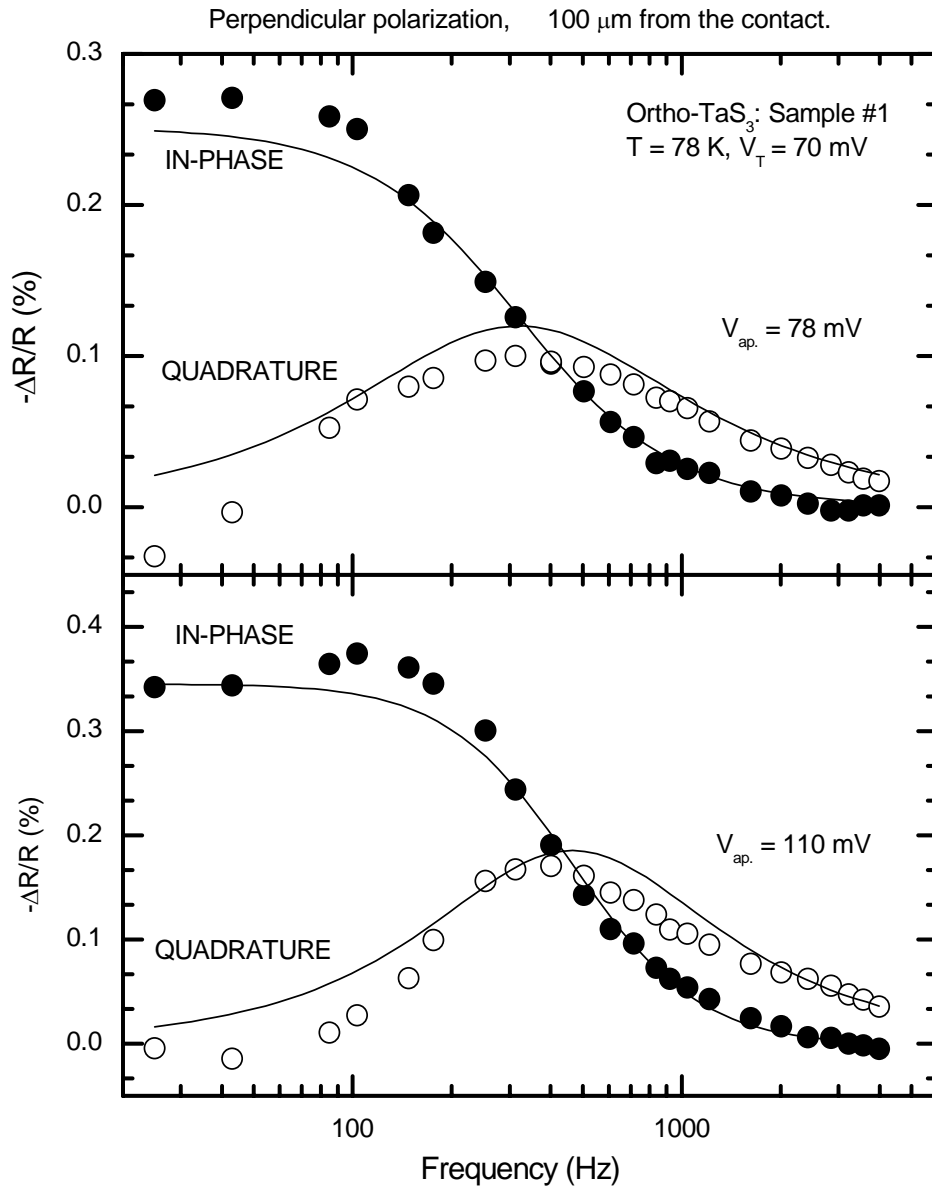


Figure 3.22 Frequency dependence of the in-phase and quadrature electro-reflectance for 78 mV (upper panel) and 110mV (lower panel) square waves for Sample #1, with light ( $\nu = 760 \text{ cm}^{-1}$ , perpendicular polarization) incident at 100  $\mu\text{m}$  from the left contact. Non-symmetric quadrature components make data poorly fit by Equation 3.13. (The best fits are shown)

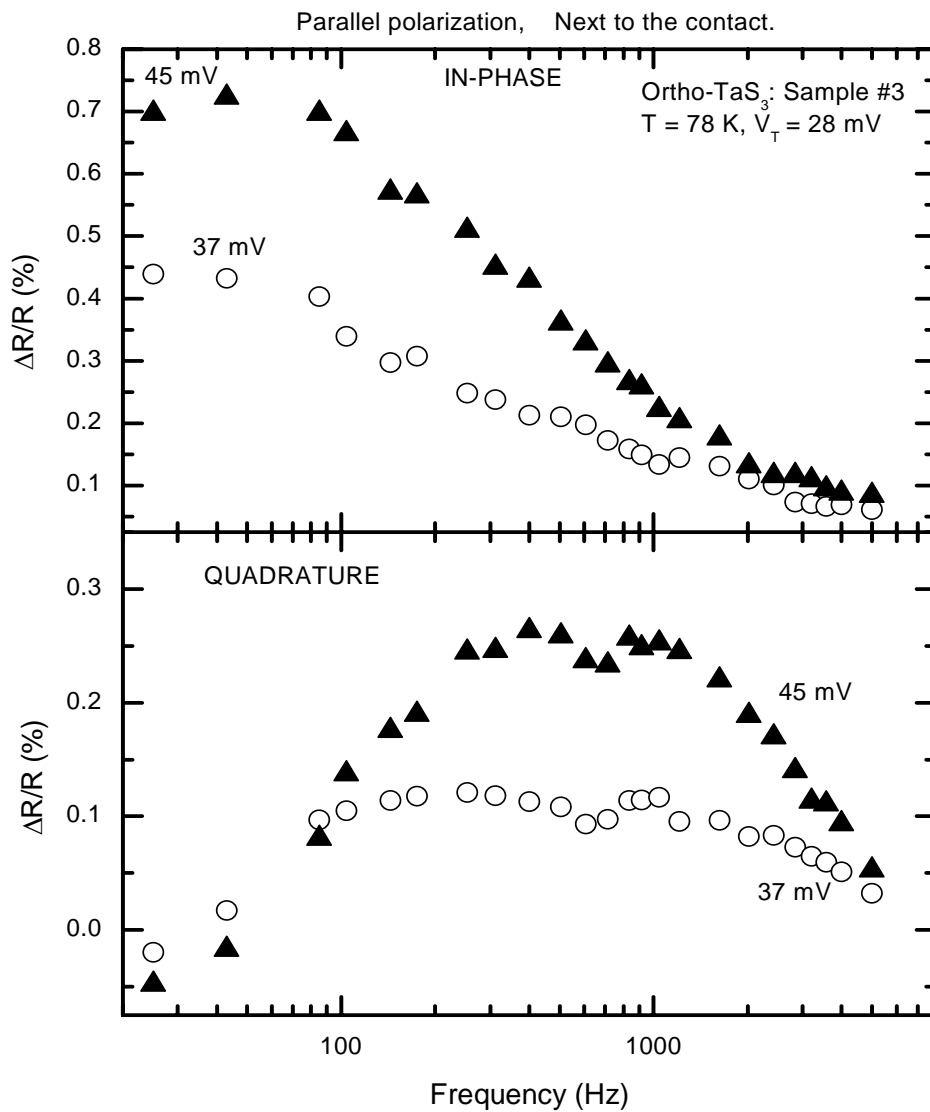


Figure 3.23 Frequency dependence of the in-phase (upper panel) and quadrature (lower panel) electro-reflectance for 37 mV and 45 mV square waves for Sample #3, with light ( $\nu = 720 \text{ cm}^{-1}$ , parallel polarization) incident adjacent to the contact. Double peaks in quadrature become more visible at the lower voltages due to the size of  $\Delta R/R$  signal.

find that the relaxation time varies as  $\tau_0 \sim V^{-p}$ , with p between 1 and 1.5, that the distribution of relaxation times increases at low voltages, and that the relaxation time increases away from the current contacts. The resonant frequency with its typical value of  $\Omega_0/2\pi \sim 1$  kHz suggests that there is  $\sim 100$   $\mu$ s delay between the applied voltage and the electro-reflective response.

# Chapter 4

## Conclusions

We searched for narrow-band-noise (NBN) modulations of the infrared transmission in blue bronze when the CDW was depinned: when the CDW slides due to application of a dc voltage above threshold, the CDW current oscillates at the NBN frequency  $f = v_{CDW} / \lambda$ , where  $v_{CDW}$  is the average CDW velocity and  $\lambda$  is the CDW wavelength length. We identified 3 possible causes for corresponding oscillation of the transmission: a) modulations of quasi-particle density due to spatial variations of the oscillating current; b) oscillations of the energy of soliton states<sup>27</sup>; and c) oscillations of phonon frequencies. No modulations in the infrared transmission were observed. The experimental limits to the above possibilities are; a) modulations of quasi-particle density gives the velocity coherence length  $\xi_{\parallel} > 1 \mu m$ , comparable to the phase coherence length; b) if oscillations of midgap states are coherent in the crystal, then the duty cycle of the oscillations  $\eta < 1/10$ ; c) phonon frequencies oscillate by  $\Delta v_{NBN} < 0.02 \text{ cm}^{-1}$ .

The first evidence that the reflectance of blue bronze varied with voltage, generally as expected from its electro-transmittance, was presented in this thesis. In particular, the electro-reflectance spectra were dominated by phonons, rather than quasiparticle, changes and consequently the changes were small, with relative changes in reflectance,  $|\Delta R/R| \sim 0.1\%$  for transversely polarized light and a few times smaller for parallel polarized. Consequently, the sign of the reflectance change (at a given position and voltage) varied as the wavelength was tuned through phonon lines. The dependence of  $\Delta R/R$  (for a given wavelength) on position was slightly different than for the electro-transmittance, in that the magnitude of the electro-reflectance signal decreased (and, for low voltages and frequencies, the signal became inverted) near the contacts; these differences suggested that the CDW strain was affected by the sample surface, perhaps



due to the placement of the contacts or the dynamics of pinning on the surface is different than in the bulk or both.

The electro-reflectance spectrum (from  $845 \text{ cm}^{-1}$  to  $1080 \text{ cm}^{-1}$  for transverse polarization) was fit by varying the background dielectric constant, frequency, linewidth, and oscillator strength of the phonons. We found that the resulting changes in background dielectric constant were  $\sim 0.05 \%$  and/or oscillator strength and/or frequency shifts of the phonons were  $\sim 0.05 \%$  and  $\sim 0.005 \text{ cm}^{-1}$ . We also found that parallel polarized phonons are affected by CDW strain, and these changes dominate the electro-reflectance spectrum. The phonon modulations due to the CDW polarization can be better understood if both the reflectance and transmittance spectra were studied and fit simultaneously on the same sample. However, the electro-transmission measurements require very thin samples,  $\sim 5 \text{ }\mu\text{m}$  for transverse polarization of light and  $< 1 \text{ }\mu\text{m}$  for parallel polarization, and measurements of both electro-transmission and electro-reflectance for the same samples have not yet been done.

We also compared the contact and bulk electro-reflectance spectra for parallel polarization of light to search for new absorption features that could be associated with CDW current injection: the contact spectra were taken near the current contact with a unipolar square-wave voltage and the bulk spectra were taken at  $\sim 300 \text{ }\mu\text{m}$  from the contact with a bipolar square-wave voltage. No absorption features associated with current conversion were observed, giving an upper limit for  $[n\sigma/\Gamma]$  (where  $n$  is the soliton density,  $\sigma$  is the geometric cross-section, and  $\Gamma$  the soliton linewidth) a few times lower than its expected value over most of the spectral range, suggesting that such states occur on less than 30 % of the conducting chains, while we expect roughly one soliton/chain. Similarly, our result implies that the lifetime ( $T_0$ ) for which solitons can be optically excited is less than the narrow-band-noise period ( $1/f_{NBN}$ ), whereas we expect  $T_0 \geq 1/f_{NBN}$ .

We also studied the electro-reflectance of orthorhombic TaS<sub>3</sub> and measured the

position/voltage dependent change in the optical properties of this material. Unlike for blue bronze, the spatial profile is very non-symmetric, with the electro-reflectance response much larger on one side of the sample, suggesting that the CDW polarization, either because of differences in the electrical contacts or defects in the sample, tends to pile up on one side of the sample. The inversion in electro-reflectance signal near the contact for small voltages was observed which is similar to what was observed for blue bronze.<sup>58</sup> For both parallel and transverse polarizations of light,  $|\Delta R/R| \sim 1\%$ , an order of magnitude larger than for blue bronze, with typical time constants also a few times larger than for blue bronze.<sup>58</sup> As the differences in the spatial dependence of  $\Delta\tau/\tau$  and  $\Delta R/R$  were previously noted in blue bronze, it will be interesting to compare the time dependence of  $\Delta\tau/\tau$  and  $\Delta R/R$  for TaS<sub>3</sub>.

Dynamics of the sliding CDW state of the orthorhombic TaS<sub>3</sub> were studied by measuring the frequency dependence of the electro-reflectance signal at different square wave voltages and at different positions on the sample. The in-phase response of  $\Delta R/R$  was observed to be inverted for frequencies greater than  $\sim 1$  kHz, indicative of surprisingly large inertia to the CDW repolarization. This large inertia was also observable as a polarity dependent delay in  $\Delta R$  in measurements of its time dependence. The frequency dependence of  $\Delta R/R$  was fit to a modified damped harmonic oscillator equation, and the relaxation time was measured to vary as  $\tau_0 \sim V^{-p}$ , with  $3/2 \geq p \geq 1$ . From the fit, it was found that the distribution of relaxation times broadened at low voltages and increased away from the current contacts, suggesting that the relaxation was driven by the local CDW strain. The resonant frequency of  $\Omega_0/2\pi \sim 1$  kHz suggested that the delay between the applied current and the electro-reflective response was  $\sim 100$   $\mu$ s.

As seen in the time dependence measurements, the observed delayed response of  $\Delta R$  as compared to the current suggests that the underlying assumption, that the response is proportional to the local CDW strain i.e.  $\Delta R/R \propto \partial\phi/\partial x$ , may require qualification, since the current overshoot indicates that the CDW polarization is undelayed. The time

difference between the electro-reflectance and current may reflect the fact that they are probing different fractions of the sample depth.

The electro-optic measurements proved to be a useful method to study the temporal and spatial dependence of changes in CDW polarization without adding multiple contacts, which strongly perturb the local fields.

# Appendix:

## A. Dielectric Constant and Reflectivity:

Reflectivity for normally incident light on an optically thick material, as found in any standard optics textbook<sup>101, 102</sup>, is given by

$$R = \left| \frac{\tilde{n} - 1}{\tilde{n} + 1} \right|^2 = \frac{(n - 1)^2 + k^2}{(n + 1)^2 + k^2} \quad (1)$$

where  $n$  and  $k$  are the real and imaginary parts of the complex index of refraction ( $\tilde{n}$ ). The dielectric function,  $\tilde{\epsilon}$ , is also a complex quantity and is related to the index of refraction given by the equation;<sup>101, 102</sup>

$$\tilde{n} = n + ik = \sqrt{\tilde{\epsilon}} = \sqrt{(\epsilon_1 + i\epsilon_2)} \quad (2)$$

Solving for  $n$  and  $k$  in terms of the real and imaginary parts of the dielectric function, we have,

$$\epsilon_1 = n^2 - k^2, \quad \epsilon_2 = 2nk \quad (3)$$

and

$$n = \sqrt{\frac{\epsilon_1 + (\epsilon_1^2 + \epsilon_2^2)^{1/2}}{2}}, \quad k = \sqrt{\frac{-\epsilon_1 + (\epsilon_1^2 + \epsilon_2^2)^{1/2}}{2}} \quad (4)$$

so that

$$R = \frac{1 + \sqrt{(\epsilon_1^2 + \epsilon_2^2)} - \sqrt{2(\epsilon_1 + \sqrt{\epsilon_1^2 + \epsilon_2^2})}}{1 + \sqrt{(\epsilon_1^2 + \epsilon_2^2)} + \sqrt{2(\epsilon_1 + \sqrt{\epsilon_1^2 + \epsilon_2^2})}} \quad (5)$$

For a semiconductor, the subgap dielectric function represents the sum of all (damped harmonic) oscillators (e.g. phonons) and can be expressed as <sup>103</sup>

$$\begin{aligned}\tilde{\varepsilon}(\nu) &= \varepsilon_b + \sum_j \frac{A_j}{\nu_j^2 - \nu^2 - i\nu\Gamma_j} \\ &= \varepsilon_1(\nu) + i\varepsilon_2(\nu)\end{aligned}\tag{6}$$

where  $\varepsilon_b$  is the background dielectric constant due to electrons,  $A_j$  is proportional to the oscillator strength,  $\Gamma_j$  is the linewidth, and,  $\nu_j$  is the frequency of the phonon. Separating the real and imaginary parts of the dielectric function, and assuming  $\varepsilon_b$  is real,

$$\varepsilon_1(\nu) = \varepsilon_b + \sum_j \frac{A_j(\nu_j^2 - \nu^2)}{(\nu_j^2 - \nu^2)^2 + \nu^2\Gamma_j^2},\tag{7}$$

$$\varepsilon_2(\nu) = \sum_j \frac{A_j\nu\Gamma_j}{(\nu_j^2 - \nu^2)^2 + \nu^2\Gamma_j^2}\tag{8}$$

Now, using Equations (5), (7), and (8), we can fit the reflectance spectrum to get the phonon parameters. The electro-reflectance spectrum is then fit by varying some of these phonon parameters.

## **B. Soliton Absorption Calculation for the CDW (blue bronze):**

The analysis of soliton absorption for an incommensurate CDW, especially in the context of blue bronze, is discussed by J. W. Brill in his recent paper. <sup>84</sup> In this paper, the author compares the possible soliton to band absorption in blue bronze with a continuum model of soliton absorption in polyacetylene. Our soliton analyses of electro-transmission and electro-reflectance measurements in blue bronze from References <sup>57, 58</sup> [55,56] were reanalyzed with this new approach.

The soliton absorption coefficient, for light polarized parallel to the chain, was expressed as <sup>104</sup>:

$$\Delta\alpha(\nu) = n(e^2 / \hbar c \varepsilon_1^{1/2}) \pi \xi_{\parallel}^2 x^{-1/2} \sec h^2(x), \quad x \equiv (\nu / \nu_0)^2 - 1 \quad (9)$$

where  $n$  is the soliton density,  $\nu_0$  is the soliton excitation energy, and  $\tilde{\varepsilon} = \varepsilon_1 + i\varepsilon_2$  is the dielectric constant. Since one of the powers of the coherence length  $\xi_{\parallel}$  came from the geometric size of the soliton <sup>105</sup> and the other from its induced dipole moment, Brill replaced  $\xi_{\parallel}^2$  with  $\xi_{\parallel} \xi_{\perp}$  (i.e.  $\sigma_0$ ) for transversely polarized light.<sup>84</sup> Replacing the divergence of Equation 9 with a peak of the same intensity,

$$\int \Delta\alpha(\nu) d\nu \sim 0.6n(e^2 / \hbar c \varepsilon_1^{1/2}) \pi \xi^2 \nu_0, \quad (10)$$

where  $\xi^2 = \xi_{\parallel}^2$  or  $\xi^2 = \xi_{\parallel} \xi_{\perp}$ . For concreteness, taking a Lorentzian peak in  $\tilde{\varepsilon}$  :

$$\tilde{\varepsilon} = \varepsilon_{\infty} + M\Gamma\nu_0 / [(\nu_0^2 - \nu^2) - i\Gamma\nu], \quad (11)$$

where  $M$  is the (dimensionless) oscillator strength,  $\Gamma$  is the FWHM, and  $\varepsilon_{\infty}$  is the background dielectric constant. If we assume that the soliton absorption is weak, we can take  $M$  to be small (unlike the phonon contributions) <sup>84</sup>:

$$\varepsilon_1 = \varepsilon_{10} + \delta_1, \quad \varepsilon_2 = \varepsilon_{20} + \delta_2 \quad (\delta_j < \varepsilon_{j0}). \quad (12)$$

At the peak ( $\nu_0$ ),  $\delta_1 = 0$ ,  $\delta_2 = M$ . The integral of the change in absorption coefficient,  $\Delta\alpha = (4\pi\nu) \Delta k$ , for  $\nu$  expressed in wavenumbers, due to the peak is then <sup>84</sup>

$$\int \Delta\alpha(\nu) d\nu \sim 2^{3/2} \pi \nu_0 \Gamma M / \{[(\varepsilon_{10}^2 + \varepsilon_{20}^2) - \varepsilon_{10}] [(\varepsilon_{10} / \varepsilon_{20})^2 + 1]\}^{1/2} \quad (13)$$

so that, comparing with Equation 10, the oscillator strength is

$$M \sim 0.212 (e^2 / \hbar c) (n \xi^2 / \Gamma) \{[(\varepsilon_{10}^2 + \varepsilon_{20}^2) - \varepsilon_{10}] [(\varepsilon_{10} / \varepsilon_{20})^2 + 1] / \varepsilon_{10}\}^{1/2} \quad (14)$$

Transmission for near normal incidence can approximately be written as,

$$\tau \sim (1 - R^2) \exp(-\alpha d) \rightarrow \Delta\tau / \tau \sim -d \Delta\alpha, \quad (15)$$

For transverse polarized light, the difference between the bulk and contact for  $\Delta\tau/\tau$ ,

$$\delta |\Delta\tau / \tau| \sim n d (e^2 / \hbar c \varepsilon_1^{1/2}) \xi^2 \nu_0 / \Gamma \quad (16)$$

where  $n$ ,  $\Gamma$ ,  $\xi$  are density, linewidth and coherence length of soliton states (for transverse polarized light,  $\xi^2 \sim \xi_{\parallel} \xi_{\perp}$ ).

Similarly for parallel polarized light, the expected electro-reflectance signal due to the soliton absorption is given by

$$\frac{\Delta R}{R} = \frac{1}{R} \frac{dR}{d\varepsilon_2} \Delta\varepsilon_2 = \frac{1}{R} \left[ \frac{dR}{dk} \frac{dk}{d\varepsilon_2} + \frac{dR}{dn} \frac{dn}{d\varepsilon_2} \right] \Delta\varepsilon_2 \quad (17)$$

where  $R$ ,  $n$ ,  $k$  are given by Equations 1 and 4. Since at the peak,  $\Delta\varepsilon_2 = M$ , and with  $\varepsilon_{\infty\parallel} = 70 + 65i$ , (taken to match the measured spectra of blue bronze near  $1000 \text{ cm}^{-1}$ )<sup>84</sup>, Equation 14 for  $M$  becomes,

$$M \sim 0.19 (e^2 / \hbar c) (n \xi^2 / \Gamma) \quad (18)$$

Then,

$$\frac{\Delta R}{R} = (0.19) \frac{1}{R} \left[ \frac{dR}{dk} \frac{dk}{d\varepsilon_2} + \frac{dR}{dn} \frac{dn}{d\varepsilon_2} \right] (e^2 / \hbar c) (n \xi_{\parallel}^2 / \Gamma) \quad (19)$$

and the difference between the bulk and contact values of  $\Delta R/R$  is

$$\delta |\Delta R / R| \sim (n \xi_{\parallel}^2 / \Gamma) (e^2 / \hbar c) a(\varepsilon) \quad (20)$$

where  $a(\varepsilon) \approx (0.19) \frac{1}{R} \left[ \frac{dR}{dk} \frac{dk}{d\varepsilon_2} + \frac{dR}{dn} \frac{dn}{d\varepsilon_2} \right]$ , (for blue bronze,  $a(\varepsilon) \approx 4 \times 10^{-4}$ ).



# References

- 1 R. E. Peierls, *Quantum Theory of Solids* (Oxford University Press, 1955).
- 2 J. Dumas, C. Schlenker, J. Marcus, et al., Phys. Rev. Lett. **50**, 757 (1983).
- 3 K. Tsutsumi, T. Tagagaki, M. Yamamoto, et al., Phys. Rev. Lett. **39**, 1675 (1977).
- 4 T. Sambongi, K. Tsutsumi, Y. Shiozaki, et al., Solid State Comm. **22**, 729 (1977).
- 5 R. E. Thorne, Physics Today, page 42 (May 1996).
- 6 G. Grüner, Rev. Mod. Phys. **60**, 1129 (1988).
- 7 C. Schlenker, J. Dumas, C. E. Filippini, et al., in *Low-Dimensional Electronic Properties of Molybdenum Bronzes and Oxides*, edited by C. Schlenker (Kluwer Academic Publishers, Boston, 1989), Vol. 11, p. 159.
- 8 M. E. Itkis and J. W. Brill, Phys. Rev. Lett. **72**, 2049 (1994).
- 9 G. Grüner, *Density Waves in Solids* (Addison-Wesley Publishing Co., U.S.A., 1994).
- 10 P. A. Lee, T. M. Rice, and P. W. Anderson, Phys. Rev. Lett. **31**, 462 (1973).
- 11 H. Fröhlich, Proc. R. Soc. A **223**, 296 (1954).
- 12 H. Fukuyama and P. A. Lee, Phys. Rev. B **17**, 535 (1978).
- 13 P. A. Lee, T. M. Rice, and P. W. Anderson, Solid State Comm. **14**, 703 (1974).
- 14 P. A. Lee and T. M. Rice, Phys. Rev. B **19**, 3970 (1979).
- 15 C. H. Chen and R. M. Fleming, Solid State Comm. **48**, 777 (1983).
- 16 R. M. Fleming, R. G. Dunn, and L. N. Schneemeyer, Phys. Rev. B **31**, 4099 (1985).
- 17 P. Monceau, in *Electronic Properties of Inorganic Quasi-One-Dimensional Compounds*, edited by P. Monceau (D. Reidel Publishing Co., Boston, 1985), Vol. II, p. 139.
- 18 D. S. Fisher, Phys. Rev. Lett. **50**, 1486 (1983).
- 19 R. M. Fleming and C. C. Grimes, Phys. Rev. Lett. **42**, 1423 (1979).
- 20 G. Grüner, A. Zettl, W. G. Clark, et al., Phys. Rev. B **23**, 6813 (1981).
- 21 G. Verma and N. P. Ong, Phys. Rev. B **30**, 2928 (1984).
- 22 N. P. Ong, G. Verma, and K. Maki, Phys. Rev. Lett. **52**, 663 (1984).

- 23 L. P. Gor'kov, JETP Lett. **38**, 87 (1983).
- 24 H. Requardt, F. Ya. Nad, P. Monceau, et al., Phys. Rev. Lett. **80**, 5631 (1998).
- 25 M. E. Itkis, B. M. Emerling, and J. W. Brill, Phys. Rev. B **52**, R11545 (1995).
- 26 S. Brazovskii and S. Matveenko, J. Phys. I France **1**, 269 & 1173 (1991).
- 27 S. N. Artemenko, A. F. Volkov, and A. N. Kruglov, Sov. Phys. JETP **64**, 906  
(1987).
- 28 F. Ya. Nad' and M. E. Itkis, JETP Lett. **63**, 262 (1996).
- 29 G. Minton and J. W. Brill, Solid State Comm. **65**, 1069 (1988).
- 30 N. Suzuki, M. Ozaki, S. Etemad, et al., Phys. Rev. B **45**, 1209 (1980).
- 31 K. Maki and M. Nakahara, Phys. Rev. B **23**, 5005 (1981).
- 32 B. M. Emerling, in *Ph.D.Thesis, Department of Physics and Astronomy*  
(University of Kentucky, Lexington, KY, 2001).
- 33 J. Rouxel, in *Physics and Chemistry of Low-Dimensional Inorganic Conductors*,  
edited by C. Schlenker, J. Dumas, M. Greenblatt and S. v. Smaalen (Plenum  
Press, New York and London, 1996), Vol. 354, p. 1.
- 34 B. P. Gorshunov, A. A. Volkov, G. V. Kozlov, et al., Phys. Rev. Lett. **73**, 308  
(1994).
- 35 G. Travaglini, P. Wachter, J. Marcus, et al., Solid State Comm. **37**, 599 (1981).
- 36 J. Rouxel and C. Schlenker, in *Charge Density Waves in Solids*, edited by L. P.  
Gor'kov and G. Gruner (Elsevier Science Publishers B. V., New York, 1989),  
Vol. 25, p. 17.
- 37 L. Forro and J. R. Cooper, Phys. Rev. B **34**, 9047 (1986).
- 38 D. C. Johnston, Phys. Rev. Lett. **52**, 2049 (1984).
- 39 K. Nomura and K. Ichimura, J. Vac. Sci. Technol. A **8**, 504 (1990).
- 40 G. Minton and J. W. Brill, Phys. Rev. B **45**, 8256 (1988).
- 41 L. Degiorgi, B. Alavi, G. Grüner, et al., Phys. Rev. B **52**, 5603 (1995).
- 42 A. Meerscaut, L. Guemas, and J. Rouxel, J. Solid State Chem. **36**, 118 (1981).
- 43 E. Bjerkelund and A. Kjekshus, Z. Anorg. and Allg. Chemie. **328**, 235 (1964).
- 44 S. Kagoshima, H. Nagasawa, and T. Sambongi, *One-Dimensional Conductors*  
(Springer-Verlag Berlin Heidelberg, New York, 1988).
- 45 S. L. Herr, G. Minton, and J. W. Brill, Phys. Rev. B **33**, R8851 (1986).

46 A. H. Thompson, A. Zettl, and G. Grüner, Phys. Rev. Lett. **47**, 64 (1981).  
47 A. Zettl and G. Grüner, Phys. Rev. B **25**, 2081 (1982).  
48 A. Zettl and G. Grüner, Phys. Rev. B **28**, 2091 (1983).  
49 M. E. Itkis and F. Y. Nad, JETP Lett. **39**, 448 (1984).  
50 K. Machida and M. Nakano, Phys. Rev. Lett. **55**, 1927 (1985).  
51 M. E. Itkis, B. M. Emerling, and J. W. Brill, Phys. Rev. B **56**, 6506 (1997).  
52 B. M. Emerling, M. E. Itkis, and J. W. Brill, Synthetic Metals **103**, 2598 (1999).  
53 T. L. Adelman, M. C. de Lind van Wijngaarden, S. V. Zaitsev-Zotov, et al., Phys.  
Rev. B **53**, 1833 (1996).  
54 S. G. Lemay, M. C. de Lind van Wijngaarden, T. L. Adelman, et al., Phys. Rev. B  
**57**, 12781 (1998).  
55 S. Brazovskii, N. Kirova, H. Requardt, et al., Phys. Rev. B **61**, 10640 (2000).  
56 M. E. Itkis, B. M. Emerling, and J. W. Brill, Synthetic Metals **86**, 1959 (1997).  
57 B. M. Emerling, M. E. Itkis, and J. W. Brill, Eur. Phys. J. B **16**, 295 (2000).  
58 R. C. Rai, V.A. Bondarenko, and J. W. Brill, Eur. Phys. J. B **35**, 233 (2003).  
59 J. W. Brill, B. M. Emerling, and X. Zhan, J. Solid State Chem. **155**, 105 (2000).  
60 J. W. Brill, NSF proposal (2001).  
61 J. F. Butler and T. C. Harman, J. Quantum Electronics, IEEE (1969).  
62 J. F. Butler and J. O. Sample, Cryogenics **17**, 661 (1977).  
63 K. W. Nill, Optical Engineering **13**, 516 (1974).  
64 E. D. Hinkley, K. W. Nill, and F. A. Blum, Laser Focus **12**, 47 (1976).  
65 J. F. Butler, in *Electro-optical systems design*, April, 1976), p. 35.  
66 Physical properties of single crystals, ([http://www.mkt-  
intl.com/crystals/single2.htm](http://www.mkt-intl.com/crystals/single2.htm)).  
67 A. V. Golovnya, V. Ya. Pokrovskii, and P. M. Shadrin, Phys. Rev. Lett. **88**,  
246401 (2002).  
68 Thermal Expansion coefficients for common IR material,  
(<http://www.janostech.com/techinfo/csi.html>).  
69 R. C. Rai, V. A. Bondarenko, and J. W. Brill, J. Phys. IV France **12**, 85 (2002).  
70 R. C. Rai and J. W. Brill, submitted to Phys. Rev. B.  
71 G. Grüner, A. Zawadowski, and P. M. Chaikin, Phys. Rev. Lett. **46**, 511 (1981).

72 D. S. Fisher, Phys. Rev. B **31**, 1396 (1985).  
73 G. Mozurkewich, M. Maki, and G. Gruner, Solid State Comm. **48**, 453 (1983).  
74 T. W. Jing and N. P. Ong, Phys. Rev. B **33**, 5841 (1986).  
75 N. P. Ong and K. Maki, Phys. Rev. B **32**, 6582 (1985).  
76 G. Mozurkewich and G. Gruner, Phys. Rev. Lett. **51**, 2206 (1983).  
77 D. S. Fisher, Phys. Rev. Lett. **68**, 6570 (1983).  
78 S. M. DeLing, G. Mozurkewich, and L. D. Chapman, Phys. Rev. Lett. **66**, 2026  
(1991).  
79 J. L. Mozos, P. Ordejon, and E. Canadell, Phys. Rev. B **65**, 233105 (2002).  
80 J. C. Gill, Solid State Comm. **44**, 1041 (1982).  
81 J. C. Gill, J. Phys. Cond. Matt. **1**, 6649 (1989).  
82 S. Jandl, M. Banville, and C. Pepin, Phys. Rev. B **40**, 12487 (1989).  
83 B. P. Gorshunov, S. Haffner, M. Dressel, et al., J. Phys. IV France **12**, 81 (2002).  
84 J. W. Brill, Solid State Comm. **130**, 437 (2004).  
85 Z. Z. Wang and N. P. Ong, Phys. Rev. B **35**, 5896 (1987).  
86 G. X. Tessema and N. P. Ong, Phys. Rev. B **31**, 1055 (1985).  
87 A. K. Sood and G. Gruner, Phys. Rev. B **32**, 2711 (1985).  
88 K. S. Cole and R. H. Cole, J. Phys. Chem. **9**, 341 (1941).  
89 S. Havriliak and S. Negami, Polymer **8**, 161 (1967).  
90 D. Staresinic, K. Biljakovic, W. Brutting, et al., Phys. Rev. B **65**, 165109 (2002).  
91 R. J. Cava, R. M. Fleming, R. G. Dunn, et al., Phys. Rev. B **31**, 8325 (1985).  
92 X. Zhan and J. W. Brill, Phys. Rev. B **56**, 1204 (1997).  
93 G. Mozurkewich, Phys. Rev. B **42**, 11183 (1990).  
94 J. C. Gill, Solid State Comm. **39**, 1203 (1981).  
95 M. E. Itkis, F. Ya. Nad, P. Monceau, et al., J. Phys. Condens. Matter **5**, 4631  
(1993).  
96 S. V. Zaitsev-Zotov, Synthetic Metals **29**, F433 (1989).  
97 A. Zettl and G. Grüner, Phys. Rev. B **26**, 2298 (1982).  
98 G. Kriza, A. Janossy, and G. Mihaly, Lecture Notes in Physcis **217**, 426 (1985).  
99 J. Levy and M. S. Sherwin, Phys. Rev. B **43**, 8391 (1991).  
100 G. Heinz, J. Parisi, V. Ya. Pokrovskii, et al., Physica B **315**, 273 (2002).

- 101 F. Wooten, *Optical Properties of Solids* (Academic Press, New York and London,  
1972).
- 102 M. Fox, *Optical Properties of Solids* (Oxford university press, Oxford, 2001).
- 103 C. F. Klingshirn, *Semiconductor Optics* (Spinger-Verlag, New York, 1995).
- 104 A. J. Heeger, S. Kivelson, J. R. Schrieffer, et al., Rev. Mod. Phys. **60** (1988).
- 105 N. Suzuki, M. Ozaki, S. Etemad, et al., Phys. Rev. Lett. **45**, 1209 (1980).

# VITA

Ram C. Rai

- Date and place of birth:

March 12, 1969      Dharan, NEPAL

- Educational institution attended and degrees awarded:

M. Sc. in Physics, Tribhuvan University, Nepal, 1993.

B. Sc., Tribhuvan University, Nepal, 1990.

- Professional positions held:

- Research Assistant, Department of Physics and Astronomy,  
University of Kentucky, 2000 – 2004

- Teaching Assistant, Department of Physics and Astronomy,  
University of Kentucky, 1998 – 2000

- Lecturer of Physics, Tribhuvan University, Nepal, 1997-1998

- Lecturer of Physics, Kathmandu University, Nepal, 1994-1997

- Memberships and Affiliations:

- Member of American Physical Society

- Member of Nepal Physical Society

- Member of Nepal University Teacher's Association

- Professional publications:

1) E. Postolache, D. K. Powell, G. Popov, R. C. Rai, M. Greenblatt, J. W. Brill,  
“Comparison of Young’s modulus and specific heat anomalies at the magnetic  
transition in  $\alpha'$ - $\text{NaV}_2\text{O}_5$ ”, Solid State Sciences, 2, 759 (2000).

- 2) R. C. Rai, V. A. Bondarenko and J. W. Brill, "Search for narrow-band-noise modulations of the infrared transmission of blue bronze", J of Phys. IV France 12, 85 (2002).
- 3) R. C. Rai, V. A. Bondarenko and J. W. Brill, "Electro-reflectance spectra of Blue Bronze", Eur. Phys J. B 35, 233 (2003).
- 4) G. Cao, L. Balicas, X. N. Lin, S. Chikara, V. Durairaj, E. Elhami, J. W. Brill and R. C. Rai, "Field-tuned Collapse of an Orbital Ordered and Spin-polarized State: Colossal Magnetoresistance in Bilayered Ruthenate", Phys. Rev. B 69, 014404 (2004).
- 5) R. C. Rai and J. W. Brill, "Dynamics of the Electro-Reflective Response of TaS<sub>3</sub>" (submitted to Phys. Rev. B, 2004).

Ram C. Rai